Analysis of gamma decay asymmetries of ^{129m,131m}Xe in the gamma-MRI experiment

Laura Dupont

Supervisor: Dr. Magdalena Kowalska

November 30, 2020

UNIVERSITÉ DE GENÈVE

FACULTÉ DES SCIENCES
Section de physique

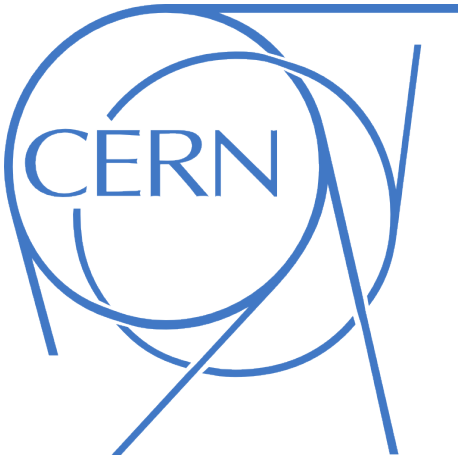

Acknowledgements

I would like to give a big thank you to Dr. Magdalena Kowalska, my CERN supervisor, who gave me the opportunity to take part in this project, for her guidance throughout this year.

I am also very grateful to everyone who helped and advice me during this thesis work: doctoral student Karolina Kulesz, doctoral student Victor Sanchez-Tembleque Verbo, Dr. Stuart Warren, professor Jose Manuel Udias Moinelo, Dr Lina Pallada, and master student Emma Linnea Wiström. Many thanks for your help, your advice, and all the helpful discussions during this project.

Finally, I would like to thank my family and friends, who supported me during all my time as a student at University of Geneva.

Contents

List of Figures

List of Tables

1 Introduction

Several powerful medical imaging techniques exist, which allow better diagnostics. The most frequently used devices are X-ray scanners which make images of the human body based on the intensity of X-ray that have crossed the patient. MRI (Magnetic Resonance Imaging) is based on Nuclear Magnetic Resonance of nuclei inside the human body in a magnetic field combined with a pulsed magnetic field gradient and radiofrequency excitations. PET (Positron Emission Tomography) uses yet another process, which consists of injecting a radioactive pharmaceutical into the patient's body which is emitting positrons, so the detectors can record two anti-parallel 511keV photons coming from the annihilation of a positron and an electron.

Often, these medical imaging methods are combined for more complete imaging. Each of these techniques is designed to image a specific thing, and it may therefore be wise to use them together for a more precise diagnosis. For example, while X-rays are stopped by dense tissues like bones, PET mostly gives information about the body physiology, and MRI rather provides anatomical information. Using several imaging methods to make a diagnosis therefore allows to combine the good aspects of these techniques, but unfortunately also the bad ones.

This thesis is part of a project combining the complementary techniques MRI and SPECT. As in MRI, we use a magnetic field and radiofrequency excitations to act on the nuclear spins, but we detect the response of the nuclei in changes of their asymmetric gamma-emission which improves the sensitivity. The isotopes used in the project are ^{129m}Xe and ^{131m}Xe.

This project was motivated by the work of a team at University of Virginia presented in a thesis [1] in 2014, and in a Nature paper [2] in 2016. Figure 1 shows the only published image using gamma-MRI imaging. The purpose of the project that this thesis is part of is to develop this experimental technique further into a medical technology.

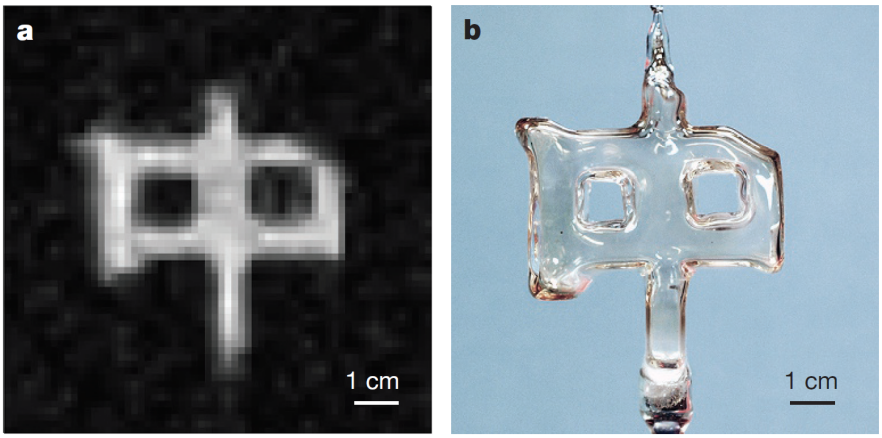

Figure 1: ^{131m}Xe MRI image [2]. Left: Image created with gamma-MRI imaging. Right: Photograph of the glass cell imaged.

The objective of the experiment performed from June to September 2019 at CERN in the ISOLDE facilities was to hyperpolarize the selected isotopes using the Spin-Exchange Optical-Pumping (SEOP) method, and then record asymmetries in gamma detection.

The task of this thesis was to use the gamma spectra recorded during the experimental period in several detectors located along and perpendicular to the magnetic field, and to try to find the best method to analyse the data, and to fit the most interesting runs to determine the degree of gamma-decay asymmetry that was achieved. This work should also allow further improvements to the experimental procedure.

2 Theory

2.1 Imaging methods

2.1.1 MRI

2.1.1.1 Setup and operation

Magnetic Resonance Imaging (MRI) is a noninvasive medical imaging radiology technique conceived to create images of the body and its processes. The imaging is based on the principle of Nuclear Magnetic Resonance (NMR), which benefits from the properties of atomic nuclei (mostly ^{1}H in the water molecules inside the body) in a magnetic field. MRI scanners have excellent contrast resolution and great versatility, which give them a wide range of medical diagnostic applications. MRI is for instance excellent for apprehending soft tissues. To process, MRI needs a stable and strong magnetic field in order to produce tissue magnetization by aligning magnetic spin moments. Then, weaker oscillating magnetic fields are applied so as to induce a change in precession which gives rise to a measurable electromagnetic signal. The particularity of MRI is that it succeeds to localize with precision the source of the NMR signal thanks to non-uniform magnetic fields called gradients, generating slightly different precession frequencies depending on the position of the atomic nuclei in these gradients. With this method, it is possible to construct and produce two or three dimensional pictures of the tissues by probing ^{1}H atoms, and therefore to understand the mechanisms.

The central element in the operation of an MRI scanner is the main magnet. It is here to polarize the sample, by producing the leading magnetic field which is permanent and stable. In addition, there are shim coils in order to maintain the homogeneity of the magnetic field over the imaged volumes. Then, the gradient coils enable to localize the region to image, and the radiofrequency system excites the nuclei in the body and catches the emitted NMR signal.

MRI is based on a property of nuclei with a spin angular momentum I which allows them to interact with a magnetic field. This interaction is the basis for Nuclear Magnetic Resonance (NMR), and is defined by the following relation:

$$\omega_0 = \gamma B_0 \tag{1}$$

With B_0 the static magnetic flux density perceived by the nucleus, ω_0 the angular frequency emerging from the rotation of the nuclear spin, γ the gyromagnetic ratio, which is constant and unique for each nuclear isotope with a spin I. It is connected to the magnetic moment of the nucleus via the relation:

$$\gamma = \frac{\mu}{Ih} \tag{2}$$

For nuclei with a spin quantum number I, and therefore 2I + 1 energy states in B_0 field, the distribution of the spins in each state is, in thermal equilibrium, determined by the following relation, called the Boltzmann law:

$$N_m = N_0 \cdot \frac{\exp\left(\frac{-E_m}{k_B T}\right)}{\sum_{n=-I}^{I} \exp\left(\frac{-E_n}{k_B T}\right)} \tag{3}$$

Where N_m is the number of spins in the state m, N_0 is the total number of spins, E_m is the energy of state m, E_n are the energies of states from $-I$ to I, T is the absolute temperature, and k_B is the Boltzmann constant.

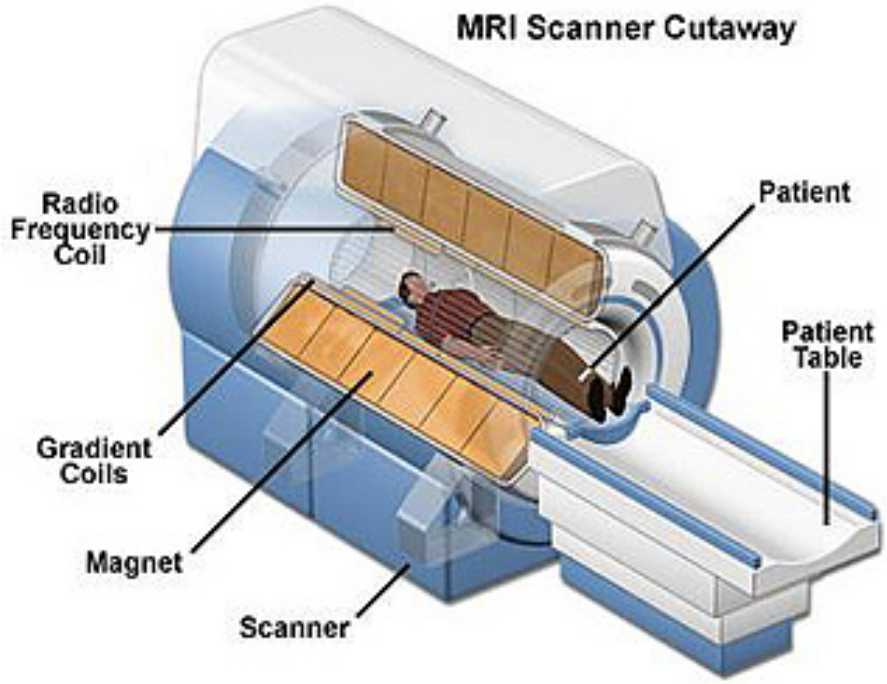

Figure 2: Scheme of a MRI scanner. [3]

The sum of the magnetic moments μ of all the nuclei with nuclear spin gives the Magnetization $M = \sum \mu$. The orientation of the Magnetization is the same as the main magnetic field. For example, if B_0 is aligned with the z axis, we have:

$$M_z = \frac{N_0 \gamma^2 \hbar^2 I(I+1)}{3k_B T} B_0 \tag{4}$$

which is called the Curie law. It shows that the magnetization is proportional to the magnetic field strength B_0. Accordingly, the higher magnetic field, the higher magnetization, and so is the signal.

The operation of MRI is based on the detection of the magnetisation vector M, which is displaced from its equilibrium position, parallel to the magnetic field B_0. For this, a second magnetic field, time varying, called B_1 is applied transversely to the main magnetic field B_0, in order to make the magnetisation vector M oscillate in time, so that M can induce a current in the coil. The resulting movement of M is given by:

$$\frac{d\vec{M}}{dt} = \gamma \vec{M} \times (\vec{B_0} + \vec{B_1}) \tag{5}$$

2.1.1.2 Technical aspects

MRI is frequently used is medical diagnosis because of its very good tissue contrast and very good resolution (of about a millimeter), especially the soft tissues. In addition, unlike many other imaging techniques, MRI doesn't require to expose the patient to radiations, because

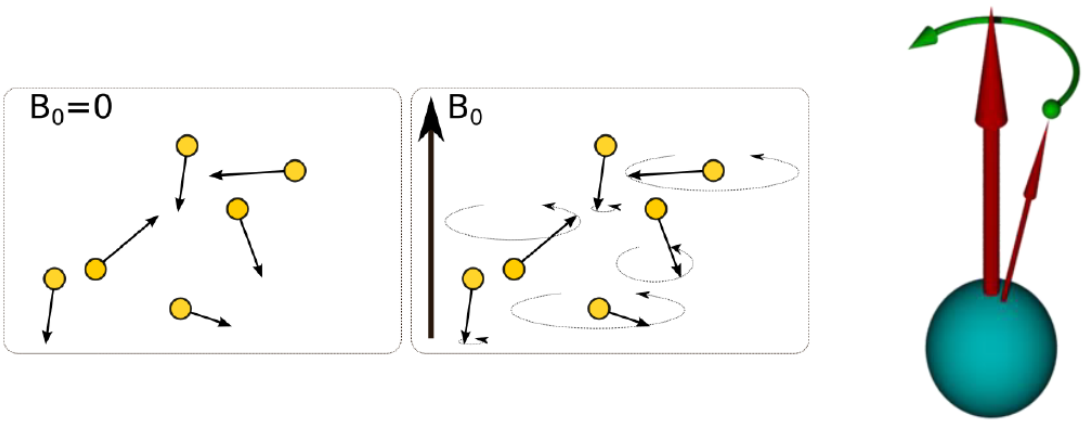

Figure 3: Illustration of the Larmor precession, showing the behavior of the nuclei with and without a magnetic field. The arrows represent the spin. [3]

it doesn't employ X-rays or radioactive materials, which makes it a non-invasive imaging method. In comparison to a CT scanner, MRI can be used with contrast agents to modulate signal strength. However MRI also have some disadvantages.

The installation of an MRI machine is more expensive, so it is less widespread, and a MRI scan also necessitate a longer acquisition time. Furthermore, as MRI scanners employ strong magnetic fields and magnetic field gradients, which have some contraindications such as, for example, if the patient has a metal implant, or a cardiac device, or in the case of allergy to the contrast medium. The discomfort linked to the reduced space for the patient in the scanner is also not negligible, or the loud noise during operation.

2.1.2 Single-photon Emission Tomography imaging

2.1.2.1 SPECT: setup and operation

Medical imaging techniques based on nuclear medicine exploit the properties of the radioisotopes that are injected into the patient to provide information about different areas of the body by detecting the intensity of gamma radiation emitted at these positions.

The Single-Photon Emission Tomography (SPECT) is a nuclear-medicine imaging method, which uses gamma detectors coupled to gamma collimators to register individual gamma photons emitted by a radioactive tracer injected into the patient. It is similar to PET, which also uses radioactive tracers and detects gamma rays in coincidence.

The first step for this method is to inject a gamma-emitting radioisotope to the patient. The radiopharmaceutical, selected for its chemical properties to be able to be selectively bound

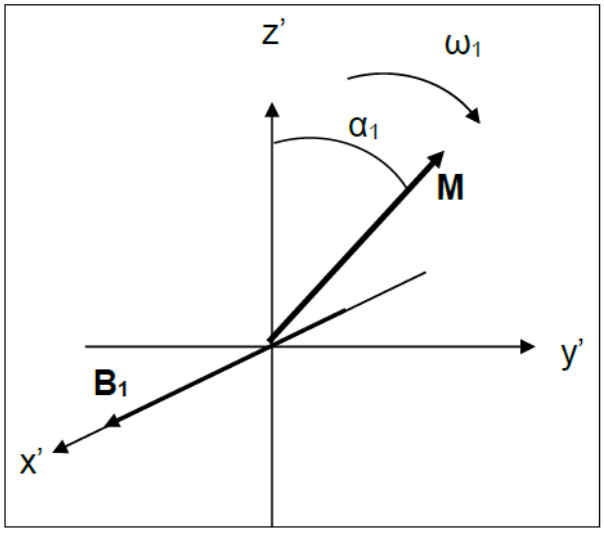

Figure 4: Illustration of the Magnetization vector after adding a second magnetic field B_1. [4]

in the body, will concentrate near certain types of tissues that one wants to image, in order to highlight certain biological processes. The radionucleus is selected according to its decay properties to be efficientlly detected. Gamma photons are then emitted from different areas and depths of the patient body. Thus, many interactions can occur in the matter, and some photons will not reach the detector, or will be deviated from their initial trajectory. Others will travel to the detector without being absorbed or deflected.

A gamma-camera is needed, rotating around the patient in order to catch the gamma-emissions from various angles. It is composed of a collimator which allows an angular selection of photons, and gamma ray detectors. Then, using an algorithm, a three-dimensional map of radioactive activity in the patient is created, and one can thus determine the distribution of the radioisotope in the body. The remaining photons that reach the detector are those coming with a parallel direction to the collimator holes. The photons approaching the collimator from other directions will likely be absorbed by the collimating material, which has a high probability of interaction with the photons. Figure 5 shows a schematic of SPECT operation and of the trajectory of a photon during the process.

2.1.2.2 Technical aspects

SPECT requires the administration of a radioactive tracer to the patient either by intravenous injection, inhalation, or by ingestion of a capsule. It is therefore more invasive than MRI. The radiation emission caught by the gamma camera allows to localize precisely the tracers in the body. To produce radionuclides, the presence of a cyclotron is necessary. It is important to use a radionuclide whose lifetime is long enough to allow imaging after administration, but

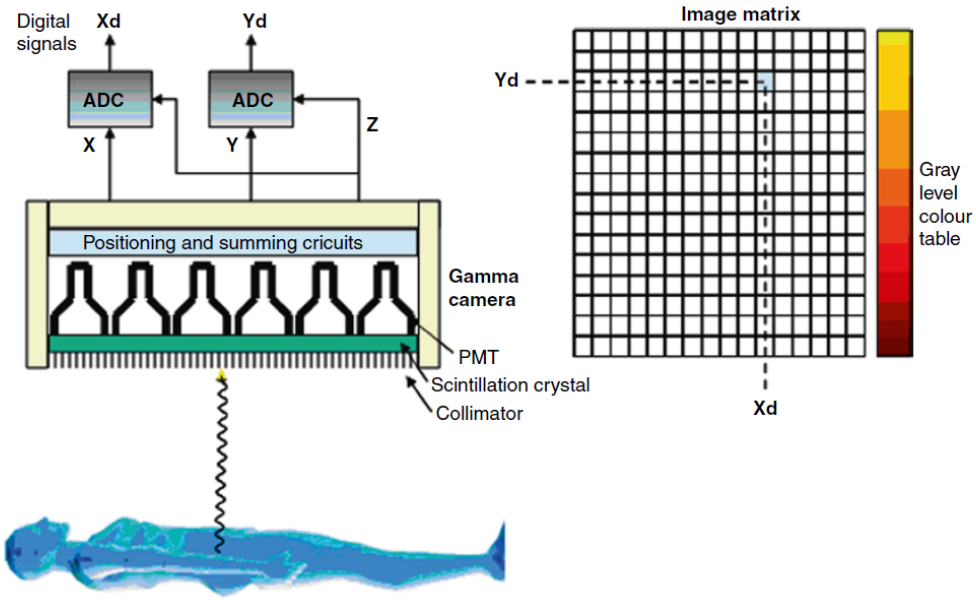

Figure 5: Scheme of the operation of SPECT and of the trajectory of a photon during the process. [5]

also short enough for the patient to be able to eliminate it fairly quickly afterwards. SPECT benefits from excellent sensitivity and good energy resolution. On the other hand, the spatial resolution is lower than MRI and reachs several millimeters.

2.2 Gamma MRI

2.2.1 Motivation

The idea of the Gamma-MRI project is to use the best facets of both MRI and SPECT, bringing together these two techniques in one.

We can see MRI and SPECT as two complementary methods. On one hand, we have MRI, which benefits from a good spatial resolution, but suffers from a bad sensitivity for signal detection. MRI sensitivity follows the Boltzman distribution equation (3) that we saw before and only around 10^{-5} nuclei react to the radiofrequency signal. On the other hand, we have SPECT, which has a good sensitivity, but provides a poor (inferior) spatial resolution. Gamma MRI aims to couple respectively the good signal generation in SPECT and the good signal acquisition in MRI.

The approach consists of recording spacial asymmetry in the emission of gamma-rays from radiotracers nuclei whose spins are highly aligned with B_0 (hyperpolarization) with $M_Z >>$ Boltzman distibution, and are manipulated by radiofrequency pulses in a gradient magnetic field.

2.2.2 Xenon Isotopes

Similar to MRI, we use an isotope with a non-zero nuclear spin which is immersed in a magnetic field, with in addition magnetic gradients. The difference is that the chosen isotopes, in our case isomers of Xenon, emit gamma radiation in a anisotropic way, which can improve the localization.

In order to perform gamma-MRI studies, we need to use isotopes compatible with the operation. Several stable isotopes of Xenon are abundant and easy to obtain, but the most suitable for this study are ^{129m,131m}Xe and ^{133m}Xe thanks to their non-zero spins (respectively $-11/2$ and $3/2$). These long-lived metastable isomers of isotopes are convenient thanks to their half-lifetime of several days, they can easily be produced, and they decay by gamma emission practical to detect for a medical use. When hyperpolarized, they decay by a anisotropic emission of gammas, which means that if the radiofrequency is in resonance with nuclei in a given volume, the asymmetry of emission will decrease. Knowing this, it is possible to quantify the amount of nuclei in a given volume.

2.2.3 SEOP

Nuclei in Gamma-MRI are introduced from outside and their spins are polarized to a high degree before administration into the sample or patient using a technique such as Spin-Exchange Optical Pumping [6], [7], [8], [9], [10].

The first step in SEOP is the Optical-Pumping of alkali metal atoms with laser light to achieve atomic spin polarization. In our case the alkali metal is Rubidium, one of the most used in optical pumping. The Rubidium is a good choice for this process for many reasons. First, it has a low melting point (39.5°C), so it is easy to obtain a high pressure vapour needed for SEOP. Furthermore, the Rubidium single electron can be excited and polarized with a laser with a wavelength of 795nm, which is easy to obtain commercially.

Once optical pumping is done, the next step is spin exchange. We want the alkali metal to transfer its polarization to the nuclei of the noble gas via spin-exchange interactions. To foster the interaction between the Rubidium and the Xenon, we heat the air around the cell containing the sample to allow the liquid alkali metal to vaporize, so our two components are in the same state. The spin-exchange can arise in two different ways. The first way is through binary collisions, which take place when Rubidium and Xenon and close enough to each other in order to transfer the spin by a hyperfine interaction between the Xenon's nuclei and the Rubidium's outermost electron. The other way of achieve spin-exchange is by the formation of Van der Waals molecules. This interaction involve a third component which is a buffer gas, like N_2 in our case. These two ways of achieving spin-exchange are illustrated in Figure 6. Rubidum and Xenon polarization can be destroyed by collisions with other molecules.

2.2.4 Asymmetric Gamma emissions

The difference between classical MRI and Gamma-MRI lies in the latter's possibility to record asymmetries of gamma radiations emitted by the source. This asymmetry is present thanks to the spin-polarization of the nuclei with spin $I > \frac{1}{2}$. The angular distribution of these emissions can be expressed by [1]:

$$W(\theta) = a_0 + a_2 \cos(2\theta) + a_4 \cos(4\theta) + a_6 \cos(6\theta) + a_8 \cos(8\theta) \tag{6}$$

Where θ is the angle of emission with respect to the polarization axis, and the a_k are coefficients depending on the polarization of the nucleus and the multipolarity of gamma

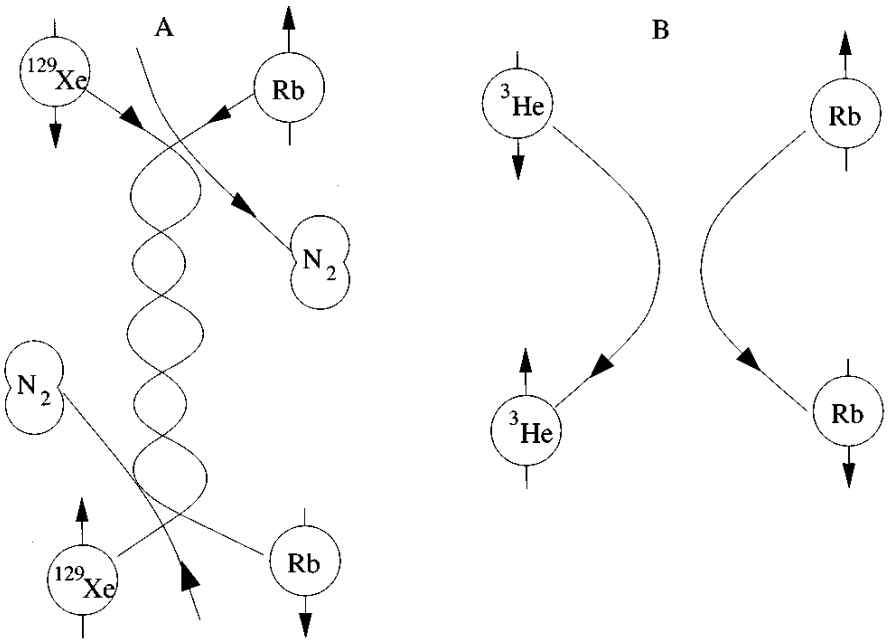

Figure 6: Illustration of the two different Spin-Exchanges. Left: the creation of Van der Waals molecules. Right: the binary collisions [10].

radiation.

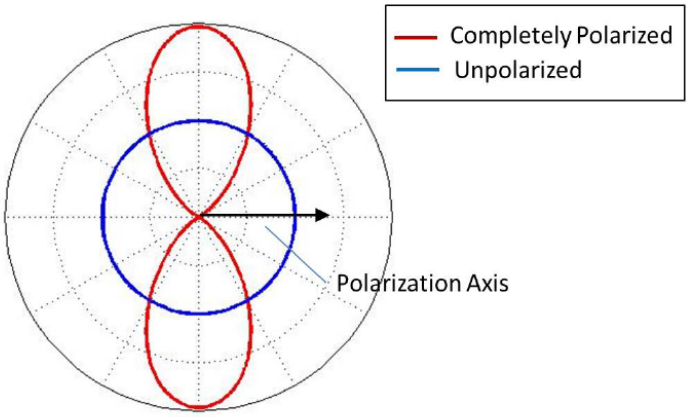

Figure 7: Angular distribution gamma rays emitted from ^{129m,131m}Xe with 0% and 100% polarization [1].

When the magnetic field is present, asymmetries can be observed with gamma detectors,

placed in the direction of the magnetic field axis, and in the orthogonal direction. Figure 7 shows the angular distribution of gamma emissions from fully unpolarised and polarised ^{129m,131m,133m}Xe nuclear levels with spin I=11/2, using the a2, a4, a6 coefficients from thesis [2].

2.3 Gamma Spectra and Compton effect

The gamma rays emitted by the decaying nuclear states are monochromatic, but the (Compton) scattering of gamma rays in the detector lead to a typical gamma spectrum, as the one shown in Figure 9. The Compton Scattering is the scattering of a photon by a charged particle (generally an electron). The photon is deprived of a fraction of its energy in the collision, and the portion of energy it lost is transferred to the charged particle. This process is shown in Figure 8. As the energy of the photon decreases, its wavelength increases according to $\lambda = \frac{c}{\nu}$, where λ is the wavelength, c is the speed of light, and ν is the frequency of radiation.

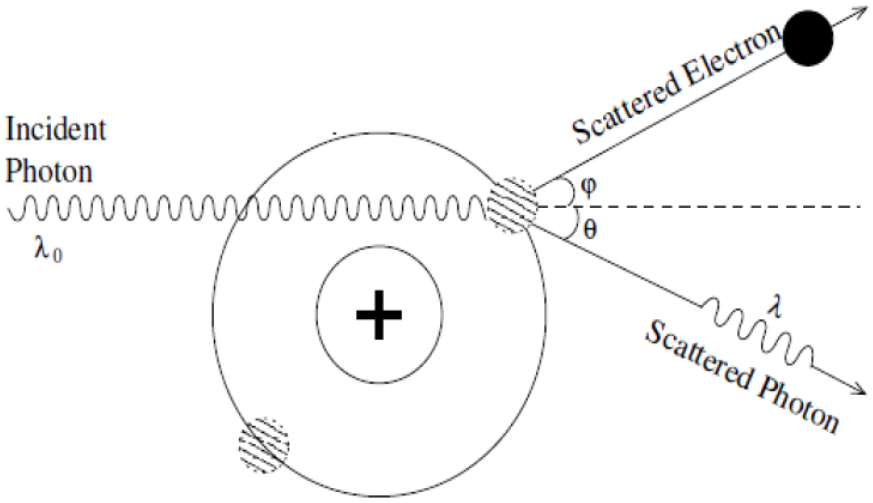

Figure 8: Illustration of the Compton Scattering [11]

The shift in the wavelength due to the Compton scattering is given by the Compton formula:

$$\Delta\lambda = \lambda_f - \lambda_i = \frac{h}{m_e c}(1 - \cos\theta) \tag{7}$$

where h is the Planck's constant, m_e is the electron's mass, and θ is the angle of deflection for the photon.

The Compton Edge is a feature coming from Compton Scattering of gamma rays interacting inside the scintillator detector. Some gammas can scatter in the scintillator, but without being absorbed, and then, only a portion of the total energy of the photon will be recorded by the detector. The gamma energy measured will vary depending on the scattering angle of the incident photon, with the biggest energy loss corresponding to a full back-scatter called the Compton edge. As a result, we obtain a spectrum of energies of all photons scattered at various angles caught by the scintillator, as illustrated in the Figure 9. The part of the

spectrum between zero and the Compton edge is called the Compton continuum.

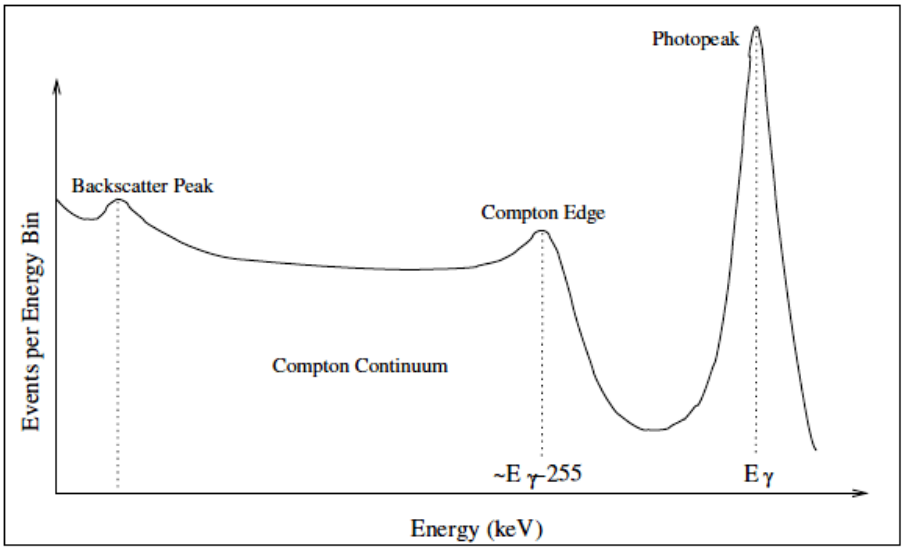

Figure 9: Gamma spectrum showing the Compton continuum and the Compton edge [11].

The energy exchanged during the process of Compton scattering is given by the formula:

$$\frac{1}{E'} - \frac{1}{E} = \frac{1}{m_e c^2}(1 - \cos\theta) \Leftrightarrow E' = \frac{E}{1 + \frac{E}{m_e c^2}(1 - \cos\theta)} \tag{8}$$

where: E is the energy of the incident photon and E' is the energy of the reflected photon.

The energy transferred by the photon to the material for different angles of deflection θ is given by $E_T = E - E'$. The maximum energy is transferred for $\theta = 180°$, and is given by the formula:

$$E_{Compton} = E_{Tmax} = E \cdot \left(1 - \frac{1}{1 + \frac{2E}{m_e c^2}}\right) \tag{9}$$

3 Experiment

This section focuses on the experimental part which took place from June to September 2019 at CERN. More precisely, this part is about the installation of the experiment, all the elements that make it up, and the course of measurements.

3.1 Principle and General setup

The goal of the experimental period was to obtain and optimise the hyperpolarization via SEOP of the two Xenon isomers, ^{129m}Xe and ^{131m}Xe, and then record gamma decay asymmetries.

The laser light polarizes the Rubidium vapour obtained by heating the oven. Then, the Xenon isomers are hyperpolarized by collisions with the polarized Rubidium vapor inside a glass cell. Once it is done, the scintillator detectors and the readout electronics are used to detect the emitted gamma rays, and observe spatial asymmetries in the emission. During this phase of the project, there were no radiofrequency pulses, and a static magnetic field was used to induce gamma anisotropies.

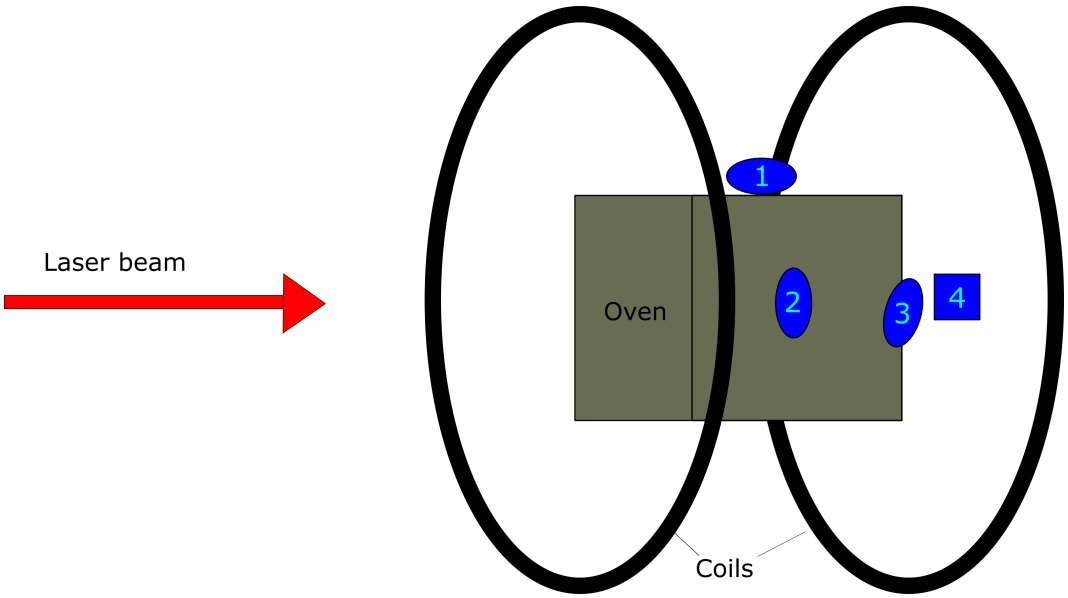

Figure 10: Scheme of the experiment.

The general setup consists of the following elements necessary to allow the experiment to run properly. A glass cell contains the sample, constituted of our Xenon isotope gas, liquid Rubidium, which become vaporous when heated, and buffer gas N_2. In order to be heated, this sample is inserted into an oven with heating tubes. An optical fiber for laser light monitoring is attached to the oven, and temperature sensors are placed close to the glass cell. Coils surrounding the oven produce the magnetic field. The laser is placed in front of the oven (with a transparent window) so that the laser beam can penetrate it and polarize the Rubidium vapour. Four scintillator detectors are installed around the oven containing

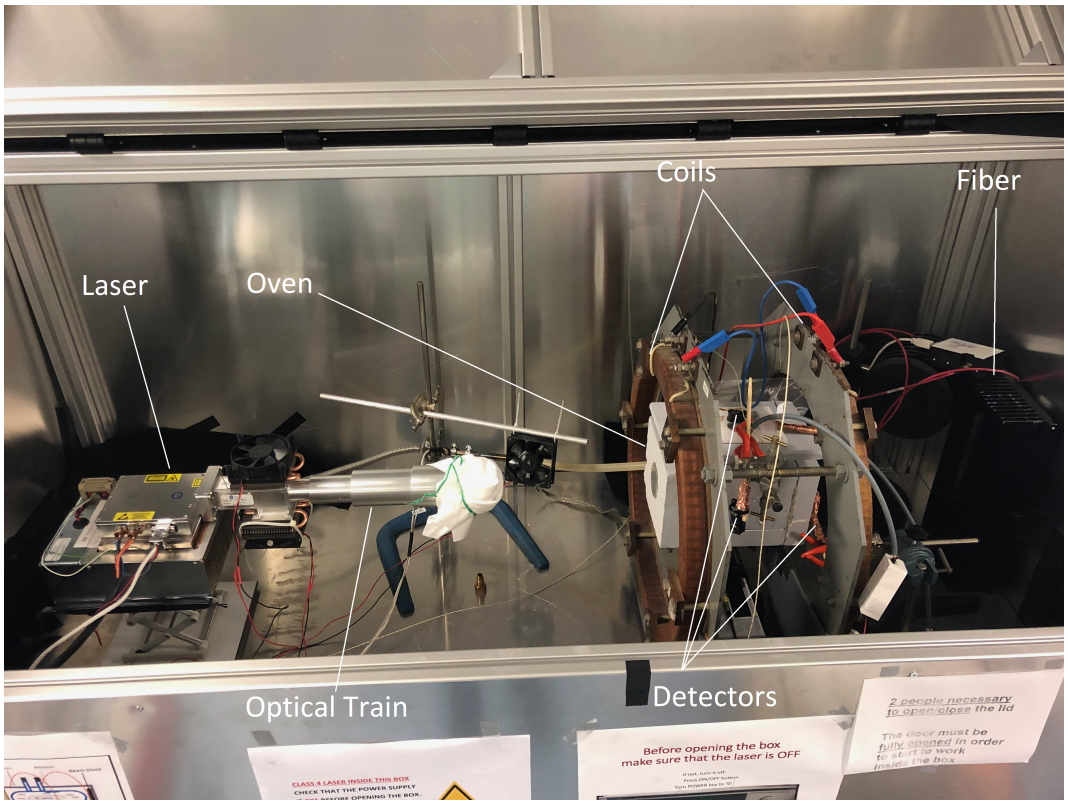

Figure 11: Setup of the experiment inside the laser box [12].

the sample in order to count the gamma emissions in longitudinal and transverse directions, and observe gamma asymmetries. The first detector changed place several times during the experimental period, it was on the top of the oven for a moment, then it was moved once the opposite to detector 2, on one side of the oven, both transverse to the laser beam, and occasionally under the oven. The third detector was all the time behind the oven longitudinally to the beam, and the last detector, the fourth one, was in times behind the oven and in times under the oven. The whole setup is shown in Figure 11.

3.2 Laser

The laser system used is composed of a Laser Module and an Optical Train. The laser is a BrightLock 50W, 800μm $\times$ 51mm Fiber-coupled Diode, with a narrow bandwidth 795nm (IR). An optical fiber is placed in the setup which guides part of the transmitted light to a wavemeter that measures the wavelength. The Optical Train includes an imaging Telescope, and a beam dump for retro-reflected light. The outgoing beam diameter is 1".

It is essential to protect users from the laser light. To achieve this, the setup is enclosed in a metal box, shown in Figure 12, to prevent all light from coming out when the laser is on, which can be opened only when the laser is off. In addition, users must wear protective glasses while the laser is operating.

The laser must be kept at a temperature below 30°C, otherwise the wavelength would shift outside 795nm, which would be a problem for the experiment because it would be out of Rubidium resonance.

Figure 12: Outside of the laser box [12].

Unfortunately, during long runs with the heater needed to melt Rubidium, the temperature was rising significantly in the whole box. Therefore, a ventilation system was added to the setup to maintain the temperature as low as possible for the laser. The installation consists of a plastic tube connected to the top of the box, and a strong fan to evacuate the hot air, with another tube at the bottom of the box to bring fresh air. This installation allows for long runs with better temperature control. The entire installation of the laser is visible in Figure 11 showing the setup in the metal box.

3.3 Magnetic field

The magnetic field is produced using Helmholtz coils. In this setup, the coils surround the oven containing the sample, located in the coils center. The sample is on the isocenter of the magnetic field, where it is the most homogenous. We use a magnetic field of 45Gauss.

3.4 Detectors

In this system, four gamma-ray detectors are used, more precisely scintillators combined with silicon photomultipliers (SiPM) to convert gamma rays into a signal without being disturbed by the magnetic field. The choice of these detectors is motivated by the fact that in this experiment we want to detect asymetries in counts between detectors, so efficiency and time resolution is more important than the resolution in energy. Three of them are CeGAGG scintillator crystals (called detectors 1, 2 and 3 in this thesis), and the last one is a LaBr3(Ce) scintillator (detector 4 in this thesis). They are coupled to silicon photomultipliers (SiPM). All detectors are shown in the Figure 13.

To convert the light signal into an electrical signal, Silicon Photomultiplier (SiPM) is used in this setup. Compared to classical PMTs, SiPMs are also more compact, and better in extreme conditions, like in a magnetic field, which makes them more suitable for our experiment.

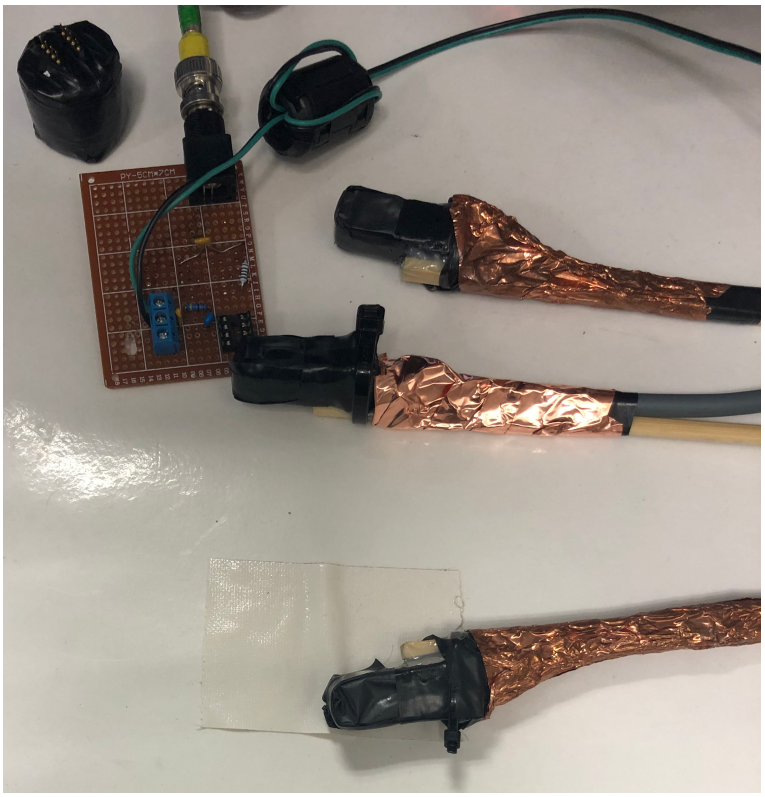

Figure 13: Detectors used during the experiment, one LaBr3Ce in the top left corner (cylinder) and three CeGAGG scintillators [12].

Most of the time, the detectors were positioned as shown in Figure 14. However, the detectors did not always remain in this configuration. The positions and/or distances were sometimes changed to record asymmetries at different positions. Therefore, in the part of this thesis concerning the experiment, the positions of the detectors will be specified.

The three CeGAGG detectors are crystal scintillators detectors. The crystal is a Gadolinium Aluminium Gallium Garnet crystal doped with Cerium. The size of the crystals is $10 \times 10 \times 30\text{mm}^3$. This type of detector has a high photon yield, and its emission peak is situated around 520nm. It is therefore well adapted to work with SiPM. They are coupled to silicon photomultipliers (SiPM) S13360-6075CS from Hamamatsu.
The scintillators are covered with a layer of tedlar film to block external light, and this layer is itself covered with Teflon tape.

The LaBr3 detector is also a crystal scintillator detector. The crystal is a Lanthanum

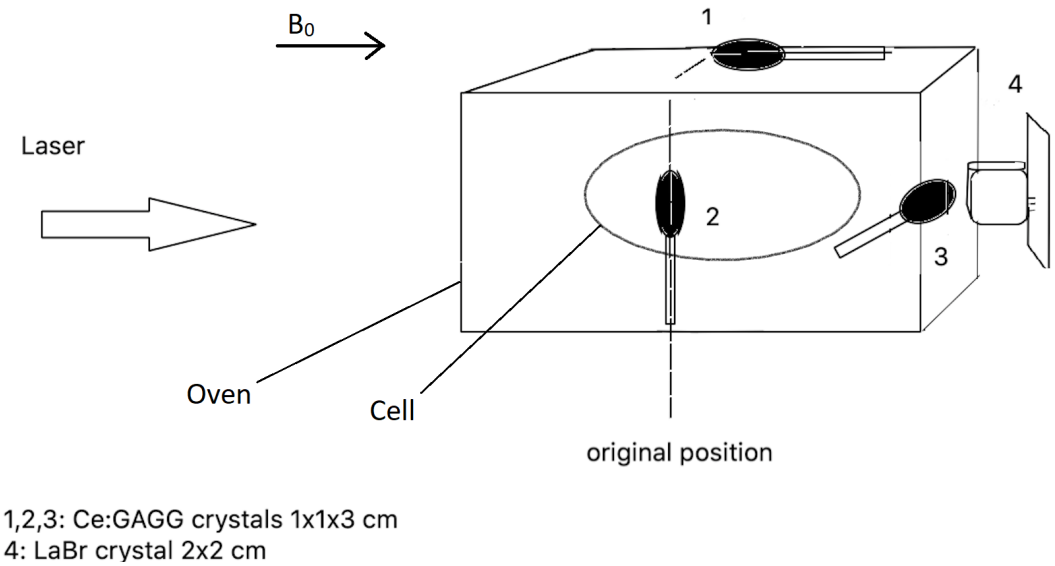

Figure 14: Typical detector positions during the experimental stage.

Bromide crystal, also dopped with Cerium. The crystal has cylindrical shape with a 20mm diameter and a 25.4mm height. This type of detector has a high photon yield too, and a good energy resolution. It is coupled with a 2×2 SiPMs matrix, with pixels of $6 \times 6\text{mm}^2$ from SensL.

3.5 Data acquisition

During the experimental phase, multiple runs were taken. The data we acquired was the number of gammas emitted by the sample recorded by each detector, their energies, and the timestamp. Most of the runs were taken to test the setup and the influence of different parameters, and then some of the runs were interesting for a deeper study.

The experimental parameters which were changed are mainly the temperature, detector positions and distances, the cell (and so potentially the xenon isotope, the pressure in it), the oven.

Once everything is in place, the laser box is closed and the preparations can begin.
The detectors and heating equipment power supply is turned on, and one can start heating the system. The ventilation equipment is also turned on, so the laser keeps a stable temperature around $25 - 28°$.
Next, one can switch on the detectors to initiate the measurements, and the laser and the magnetic fields can be turned on.

4 Data Analysis

4.1 Goal and expectations

In this section, part of the data collected during the experimental period is presented, as well as the results of the data analysis. The data recorded for each detector is number of gammas, the corresponding timestamps, and their energy.

We expect the radiation emitted to be anisotropic, as it was described in Section 2.2.4. During the data analysis, we want to compare the behaviour of the radiation when the magnetic field is on (polarization) and off (no polarization), by looking at the differences in count rates of longitudinal and transverse detectors. If a important difference between the longitudinal and the transverse detectors is recorded when the magnetic field is on, it would mean that spin polarization was achieved compared to field off.

If ^{129m,131m}Xe hyperpolarization is successfully accomplished, when the magnetic field is turned on and the nuclear spins are aligned in the axis of the magnetic field, the gamma radiation emissions should show asymmetries. This means that we should see differences for longitudinal and transverse detectors between magnetic field on and off.

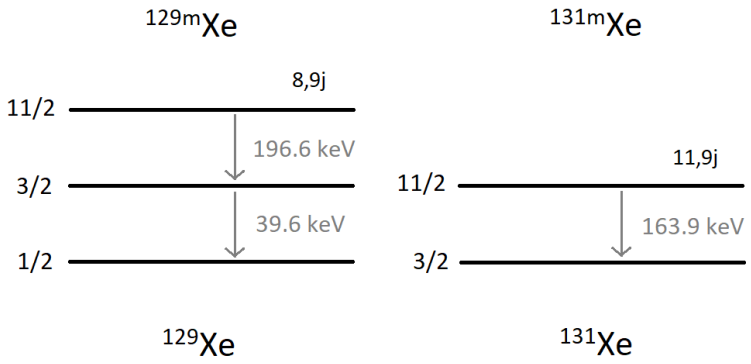

Figure 15: Decay scheme of ^{129m}Xe and ^{131m}Xe with gamma radiation energies [13].

In this work, we will be interested in the peak corresponding to the gamma radiation's emission energy, which is around 197keV for ^{129m}Xe, and around 164keV for ^{131m}Xe, whose decay schemes are shown in Figure 15.

Based on the results shown by the Virginia group [1], [2], we would expect significant differences between gamma countsin the presence and absence of the magnetic field if the Xe hyperpolarization is successfully completed, as Figure 16 shows a comparison of spectra with and without polarization registered by the Virginia group [1].

4.2 Energy calibration and separation of data

The first goal of the data analysis is to deduce the number of gammas emitted by ^{129m,131m}Xe, as detected by the scintillator detectors. Gammas in a large range of energies have been

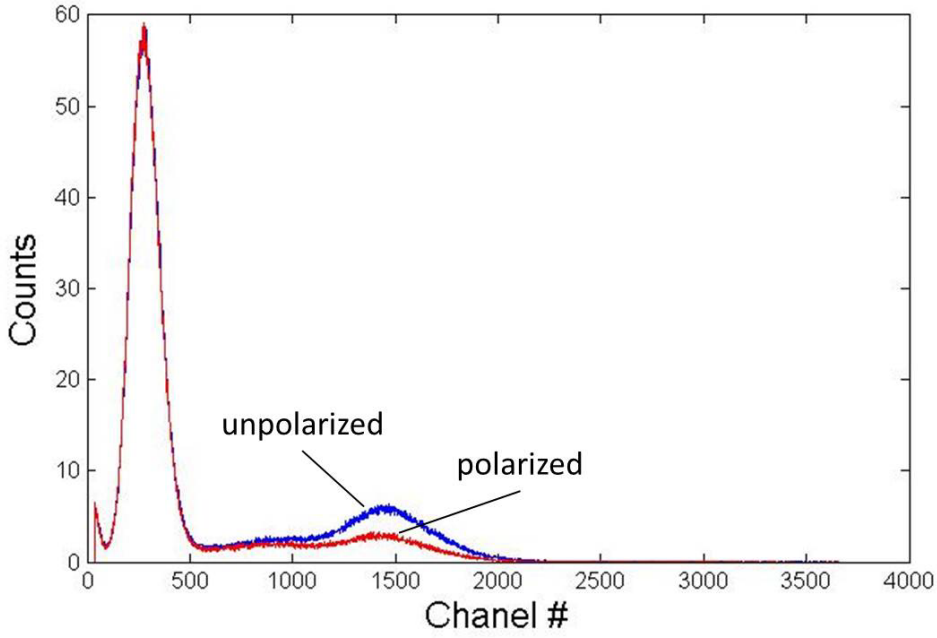

Figure 16: Polarized and unpolarized ^{131m}Xe decay spectra measured by a longitudinal detector in the Virginia experiment [1].

detected, but only a part of this range is interesting for us, namely 197keV or 164keV from the hyperpolarized ^{129m,131m}Xe, respectively. So we must separate the relevant counts from the other detected photons.

The part of the spectrum containing the data we are interested in is the rightmost peak. The objective is to determine the number of gammas per time units in this peak recorded by each detector. Then, we compare this number for the longitudinal and the transverse detectors, with and without a magnetic field, and we should see a change if we achieve polarization of ^{m}Xe. When the polarization is achieved (in presence of magnetic field), we should see a decrease in counts in the longitudinal detectors, and an increase for the transverse ones, meaning that there is polarization (see Figure 7).

There are some manipulations to be done on the spectrum before we can get number of interesting gamma counts.

The first thing is energy calibration, because we can see in Figure 17a that the scale on the x axis is just a channel number, which is proportional to the energy.

Knowing the energy of the gammas we are detecting, it is easy to make an approximate calibration with this simple formula (assuming a linear response of the detectors):

$$E_0 = E \cdot \frac{p_0}{p} \tag{10}$$

Here E is the current energy before calibration, E_0 is the calibrated energy, p is the current position of the center of the peak on the spectrum, p_0 is the energy of the photon emitted by the isotope (for example, for the ^{129m}Xe it is 195keV, and it is 163keV for the ^{131m}Xe).

To apply this correction on the spectrum, we have to do a first fit to know the middle

of the peak, and then we perform the calibration on each point. Figure 17 shows the same spectrum before and after the calibration.

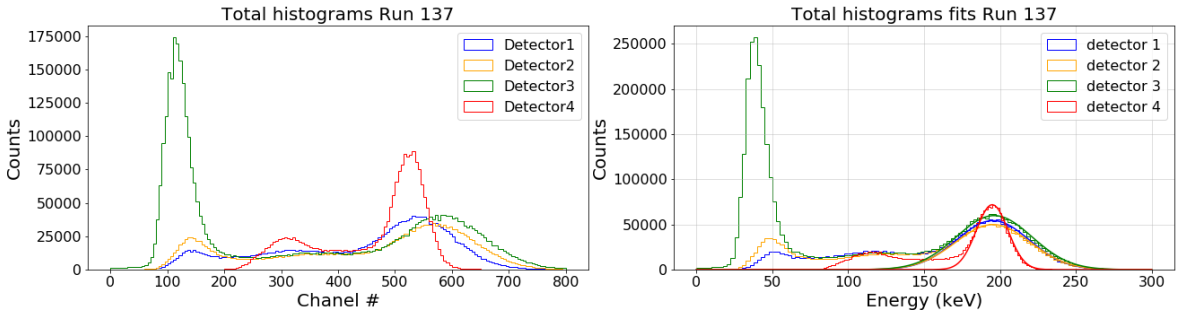

(a) Run 137, spectra before the calibration.

(b) Run 137, spectra after the calibration.

Figure 17: Histogram spectra for all detectors, Run 137. 17a) the spectra before the calibration, 17b) after calibration.

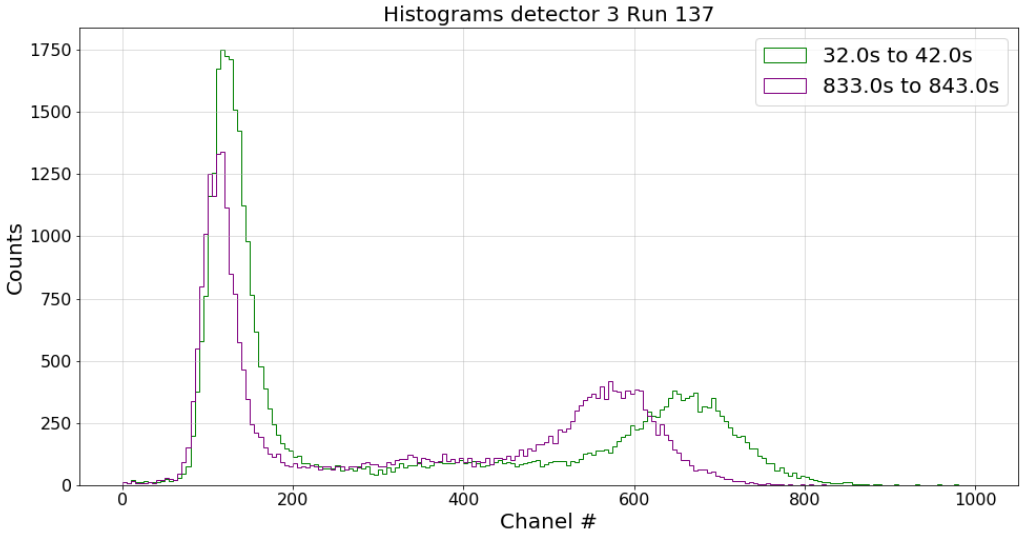

Figure 18: Two spectra containing data for 10 second intervals for detector 3 after data separation, Run 137. The **Green** spectrum shows data for 10 seconds from 32 seconds after the beginning of the measurement, and the **Magenta** spectrum shows data for 10 seconds from 1041 seconds after the beginning of the measurement. Between this two spectra, the temperature inside the oven increased by about 150°.

Furthermore, in our experiment, we have to heat the sample, which also increases the temperature of the detectors. The consequence is that the energy detected is shifted because the detector gain changes. The more the temperature rises, the more the peak is shifted. To take this into account in our analysis, the solution is to separate the data in multiple

time intervals, so that for each interval, the temperature is approximately stable. Figure 18 shows two spectra after data separation for Run 137 while the temperature was increasing, at different times to illustrate the shift induced by temperature increase.

4.3 Fit with two Gaussians

Since we don't know the exact shape of the part overlapping with the peak, we can also approximate it as a Gaussian. In this case, we try to fit only two peaks, so the formula will be an addition of two Gaussian equations:

$$g(E) = A \cdot \exp\left(-\frac{(E-\mu)^2}{2\sigma^2}\right) \tag{11}$$

Where E is the energy, A is the amplitude, σ is the variance and μ the expected value.

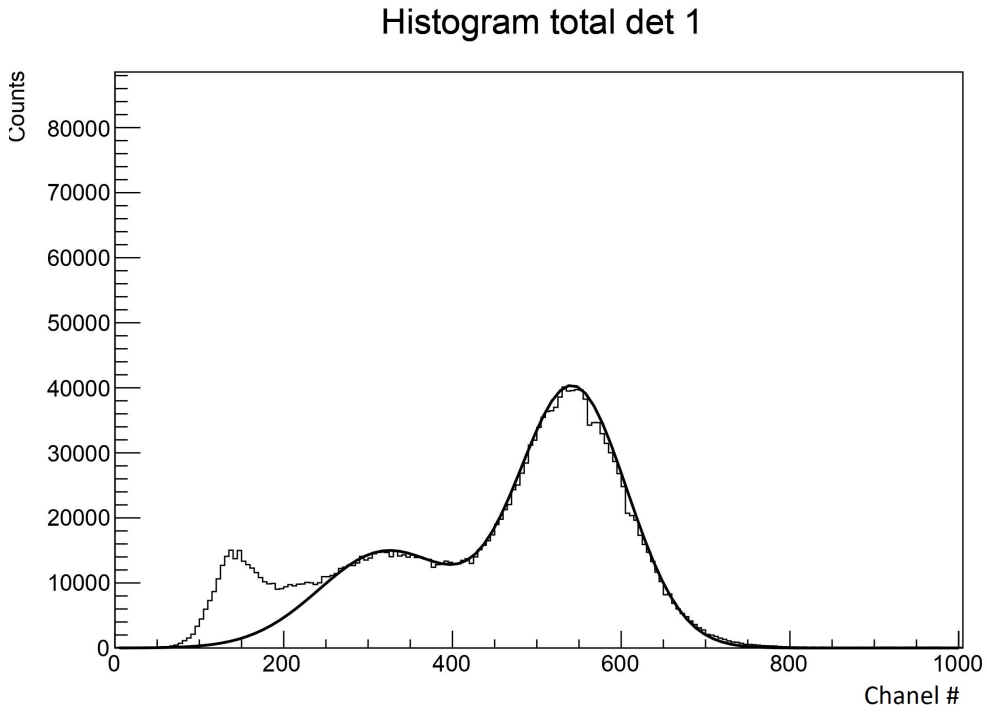

Figure 19: Histogram spectrum for detector 1 (for $x > 270$), Run 137. The **Black** line is the fit for two Gaussians. The data is not calibrated on this spectrum.

We can see what it looks like on Figure 19 that shows the fits with two Gaussians for all the data for Run 137, which seems to be a good approximation. However, when we try this on the histograms for 10 second intervals, it is way more difficult to fit the curve on the spectra. As these histograms contain less data, the shape is less smooth, and we can't predict with precision the values of the parameters, as shown in Figure 20.

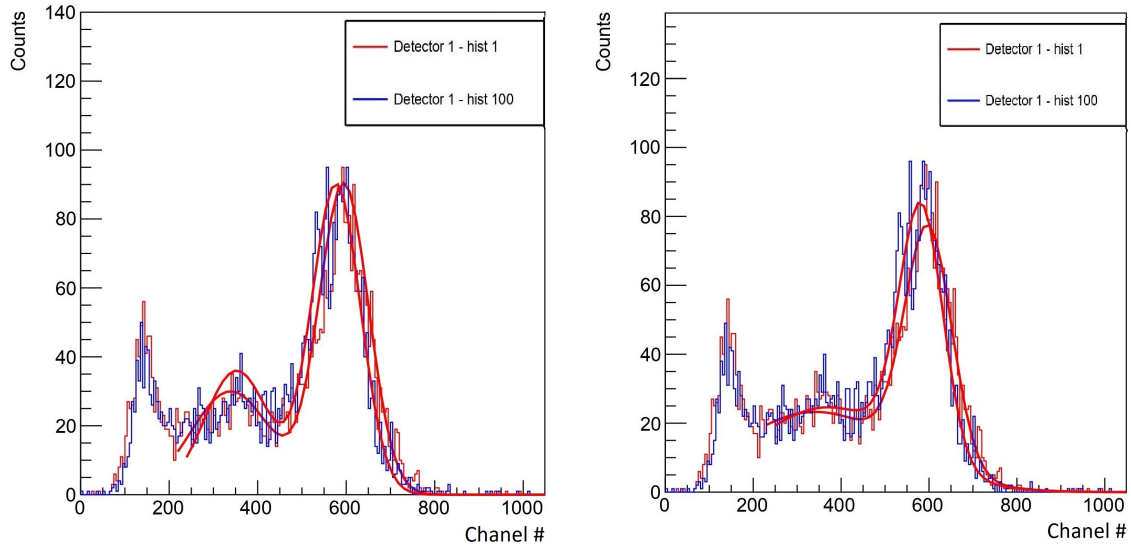

(a) 1a (b) 1b

Figure 20: Two spectra containing data for 10 second intervals for detector 1 after data separation, Run 137. This spectra have been fitted with an equation containing two Gaussians. The **Red** spectrum shows data for 10 seconds from 1 seconds after the beginning of the measurement and the **Blue** spectrum shows data for 10 seconds from 100 seconds after the beginning of the measurement. The **Red** curves are the fits for the two spectra. The data is not calibrated on these spectra.

4.4 Fit with three Gaussians using a derivative

Another thing we can try is to fit the whole spectrum. But because some of our spectra have three peaks, and others have two (due to different detector thresholds), we have to add one more step. We calculate the derivative of the spectrum, so the program can figure out how many peaks the spectrum has by looking for the points where the curve is positive and then becomes negative. Then, the program can chose the good formula to make the fit with two or three peaks according to the number of maxima it counted.

As we can see on Figure 21, using several Gaussian equations to fit our spectrum could be a good approximation with the good parameters. However, as for the fit with two Gaussians, when we try this on the histograms for 10 second intervals, it is complicated to fit the curve on the spectra, because these histograms contain less data, so the good values of the parameters are difficult to find. Furthermore, we apply this method to the separated data spectra, it is more complicated for the program to count the maxima, since the spectra are less smooth and more irregular. So, for this method, we will only use the numbers obtained by integrating the total spectrum containing all the data.

4.5 Analysis Methods

During some runs, the magnetic field was switched off (no polarization) and on (polarization should take place) several times. This is an opportunity to see if this change had the desired effect on gamma emission asymmetry. For example, Figure 21 shows the number of counts

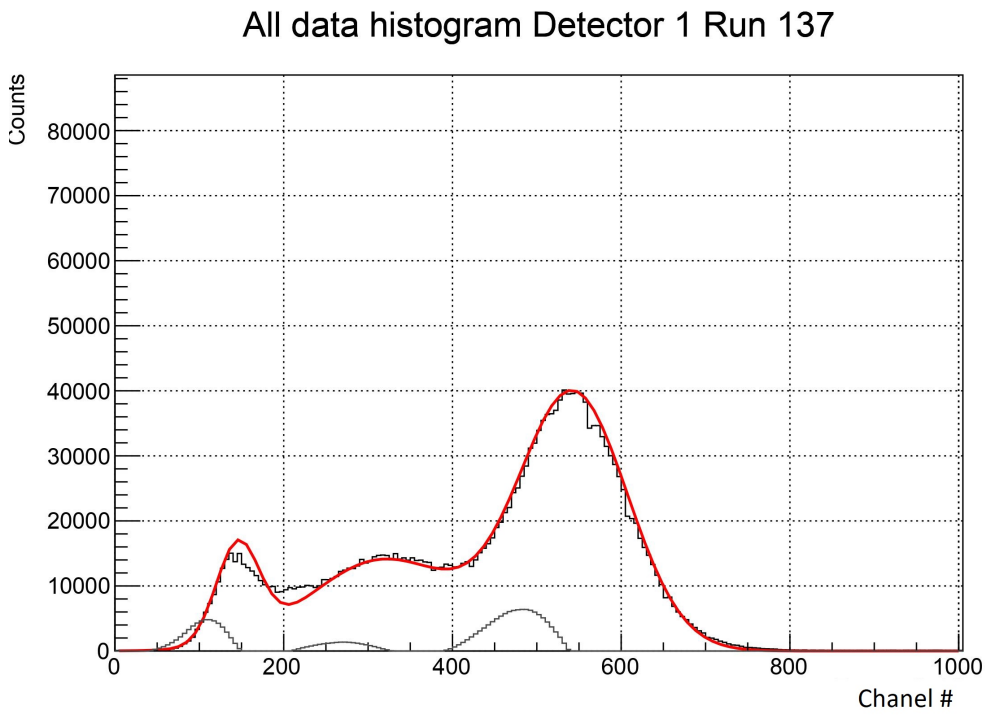

Figure 21: Histogram spectrum for detector 1, Run 137. The **Black** line is the derivative curve of the spectrum (positive part), and the **Red** line is the fit curve based on the derivative. The x axis is not calibrated on this spectrum.

for each detectors as a function of time for Run 64.

To check the effect of the magnetic field on the number of counts, we can choose a run during which the magnetic field has been switched on and off and look at the number the counts per second as a function of time.

On Figure 22, we can see many variations that may correspond to when the magnetic field is turned off or on. In particular, we can see for detectors 3 and 4 increases when the magnetic field is switched off. Unfortunately, we can also see significant variations of the same amplitude when the magnetic field remains on for a long time. It is thus difficult to be certain that these variations are induced by the magnetic field. We could probably have a better view on these possible changes if we look at data accumulated for a longer time with magnetic field on and off.

So another way to study the changes induced by the presence of the magnetic field is to look at several runs whose temperature and detection conditions are identical, but the only difference is that for some the magnetic field is on and for others it is off.

Comparing several runs, the first thing we can do is taking a look at the number of counts per second for each detector. We obtain these numbers based on the area under the curve of the Gaussian fit on the rightmost peak. We can even do this for each histogram containing the data separated in intervals of 10 seconds, and then add up the numbers obtained. By doing this, we take into account as much as possible the variations that may take place over time, such as temperature changes, which can induce the energy shift, and calibrate each spectrum.

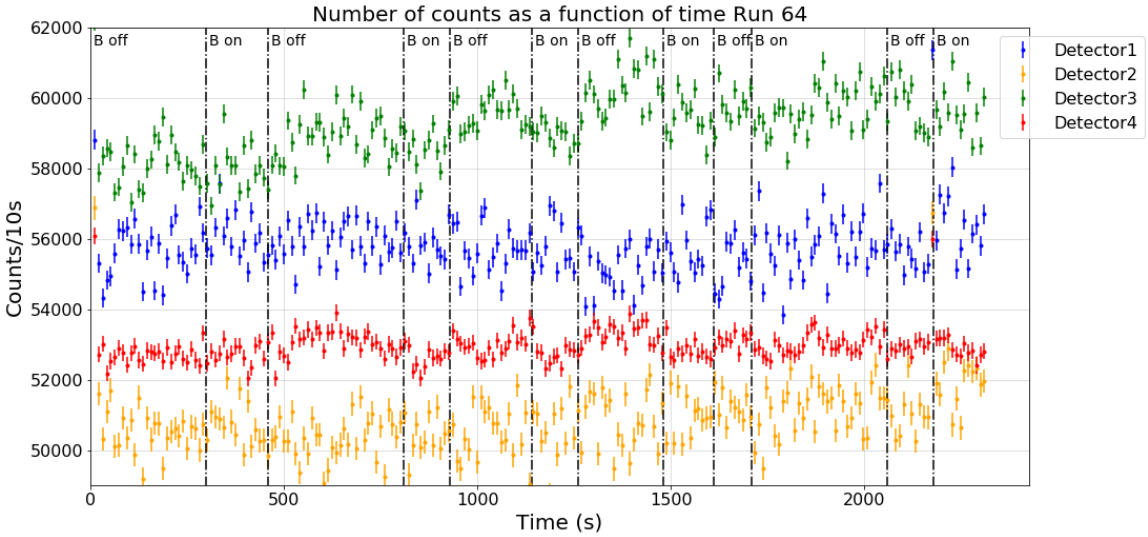

Figure 22: Fitted number of 197keV gamma rays in ^{129m}Xe as a function of time for all detectors, Run 64. The **Black** lines show the moment in time when the magnetic field changed. We subtracted arbitrary offsets for each detector for easier visualisation. Detectors 1 and 2: transverse. Detectors 3 and 4: longitudinal.

Because the detectors did not register identical number of counts in absence of polarization, to see the effect of polarization, we have calculated the percentage difference in counts per second for each detector, between the magnetic field on (Run 1) and off (Run 2):

$$P_{1/2}(det_1) = \frac{N_1(det_1) - N_2(det_1)}{N_1(det_1)} \cdot 100 \tag{12}$$

$P_{1/2}(det_1)$ is the percentage difference between Run 1 and Run 2 for detector 1, $N_1(det_1)$ is the number of counts per second of detector 1 for Run 1 and $N_2(det_1)$ is the number of counts per second of detector 1 for Run 2. If a statistically significant difference is observed, this can be interpreted as a sign of a spin polarization.

Another method could highlight small asymmetries that are difficult to perceive by looking only at the previous formula. It consists of calculating the differences in counts registered in two detectors in the same run, with magnetic field on (Run 1) and comparing this difference to the one with a magnetic field off (Run 2). The calculations are made using the following formula:

$$D_1(det_1, det_2) = \frac{N_1(det_2) - N_1(det_1)}{N_1(det_2)} \cdot 100 \tag{13}$$

$D_1(det_1, det_2)$ is the percentage difference between gamma counts per second registered by detector 1 and detector 2 for run 1, $N_1(det_1)$ and $N_2(det_1)$ respectively.

4.6 Fit optimal settings and systematical checks

To have the best possible fits, we want to determine what the optimal fit parameters are. The parameters we want to determine are the duration of the time intervals to separate the data, the optimal bin width for our histograms, and since the peak we want to fit overlaps another, the point where we want to start fits.

4.6.1 Bin widths

We can try different bin widths for our histograms, and compare the fit results. The bin width values we are going to try are 1keV, 1.5keV, 2.5keV and 5keV.

We first tried two extreme values of bin widths to see if the differences were significant: 1keV and 5keV. Figure 23 shows spectra of the peak we want to integrate and the fits for these two bin width values.

The larger the bin width, the fewer bins there are in the peak, and the fewer points available for fitting the peak. For this reason we see that 5keV seems to be too much for the bin width, while 1keV seems not to be enough, judging by the aspect of the peaks which are very irregular for the four detectors.

The left part of the peak overlaps the rest of the spectrum, the right part of the peak does not. We therefore expect that the left part of the peak is distorted by the contribution of the rest of the spectrum, while we can estimate that the right part is only slightly influenced. We will therefore look more the consistency of the fit on the right side of the peak.

We see on Figure 23a for 5keV that the fit does not precisely match the spectrum shape on the end of the right part of the peak, probably due to the few points for the fit, because this is not the case on Figure 23b for 1keV.

We then try intermediate values: 1.5keV and 2.5keV, the resulting spectra are shown in Figure 24.

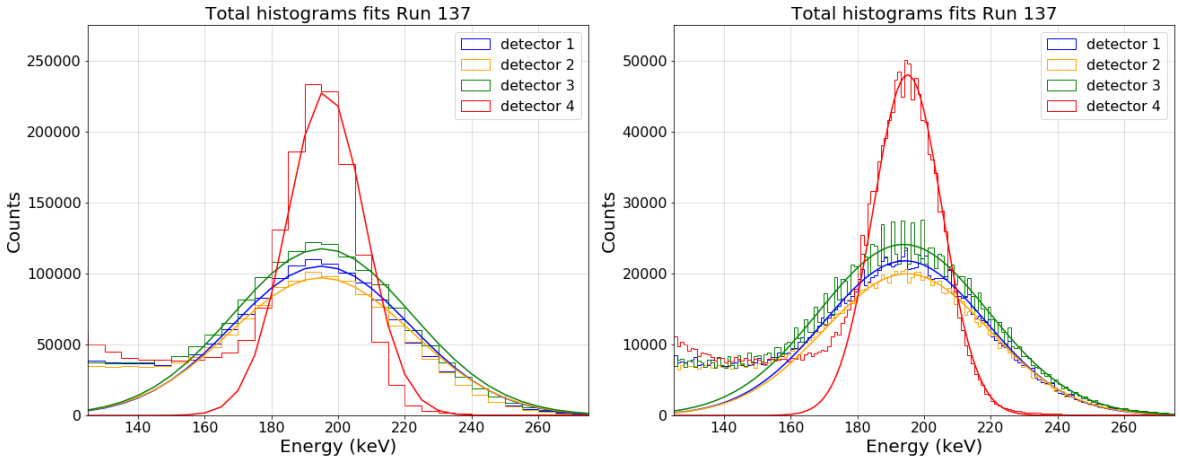

(a) Bin width = 5keV.

(b) Bin width = 1keV.

Figure 23: Histogram spectra for all detectors, Run 137, centered on the rightmost peak, with different bin widths. 23a) bin width = 5keV, 23b) bin width = 1keV.

Figure 24a shows the spectra for 1.5keV. We see that, as for 1keV, the spectra appear irregular for detectors 1, 2 and 3, and so this does not appear to be a suitable bin width. On the other hand, for the spectrum of detector 4, this width seems to be suitable.

Figure 24a shows the spectra for 2.5keV. The spectra shows that this bin width seems suitable for all detectors. For these two widths of bins, the fits seem good for all the detectors, except for the fourth detector for which 1.5keV seems more suitable, since with 2.5keV the top of the peak is not included in the fit.

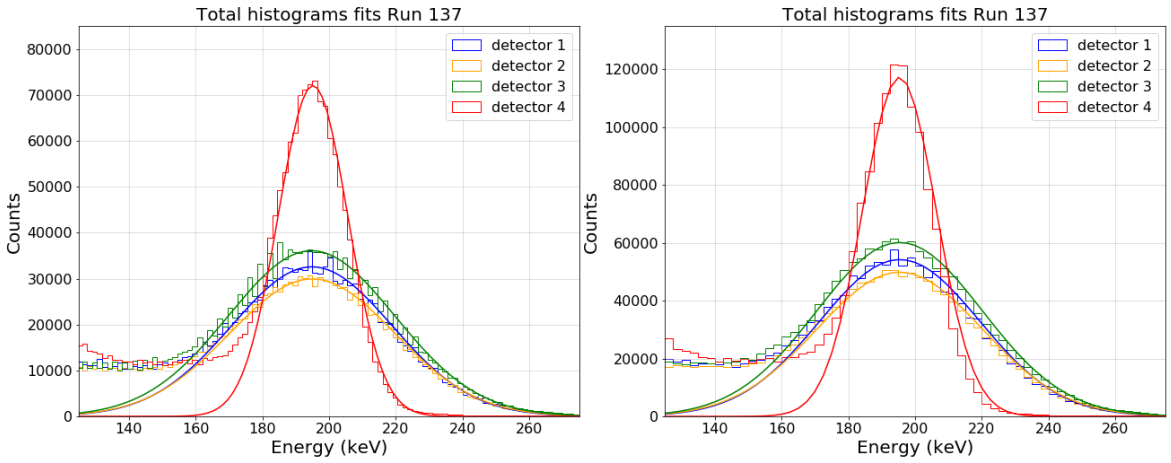

(a) Bin width = 1.5keV.

(b) Bin width = 2.5keV.

Figure 24: Histogram spectra for all detectors, Run 137, centered on the rightmost peak, with different bin widths. 24a) bin width = 1.5keV, 24b) bin width = 2.5keV.

The resulting number of counts for each detector for different bin widths for Run 137 are shown on Figure 25, and in Table 10 in Appendix A.

On Figure 25, we see that for detectors 1, 2 and 3, the curve is a little convex, so the numbers of counts decrease until reaching a minimum at 2.5keV, then start to increase again (the overestimation might be due to overestimating the right shoulder of the peak). For detector 4, the curve only increases, which is consistent with what we were seeing on the spectra, that the top of the fit curve got closer and closer to the top of the spectrum, thus taking more counts.

Figure 26 shows the percentage differences between the numbers obtained with a bin width of 1keV which is the smallest value and the numbers obtained with the other bin widths. It shows that for detectors 1,2 and 3, the curve behavior is the same. The differences are almost the same for 1.5keV and 2.5keV, and then there is a big decrease for 5keV width. As we are interested in the differences between the detectors to observe the asymmetries, it is important to look at how the relative differences between the detectors evolve on this graph. Between detectors 1, 2 and 3, the gap between the points remains almost the same for all the chosen values. For detector 4, the curve moves away between from the others between 1.5keV and 2.5keV, and then gets very close for 5keV.

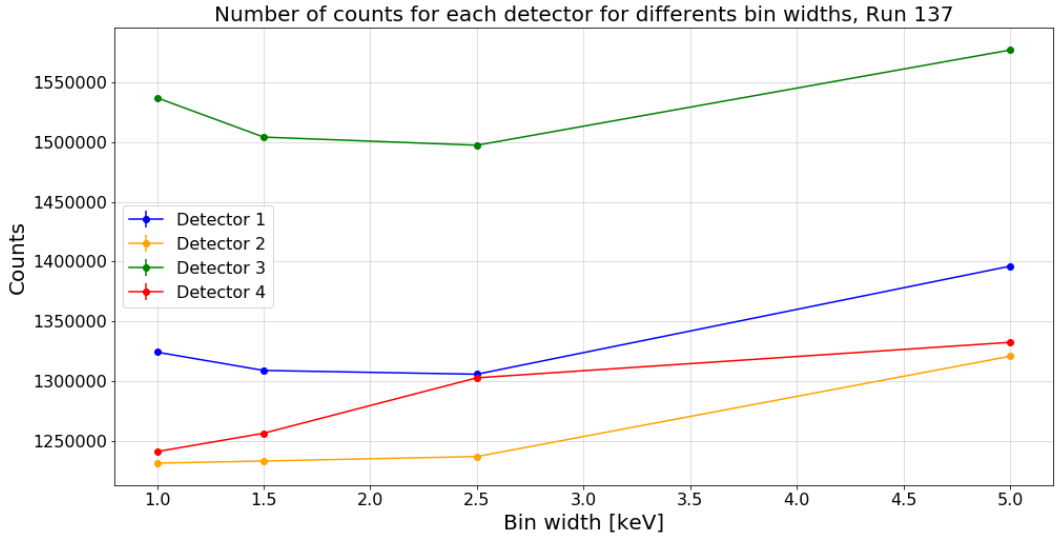

Figure 25: Number of counts for several bin widths.

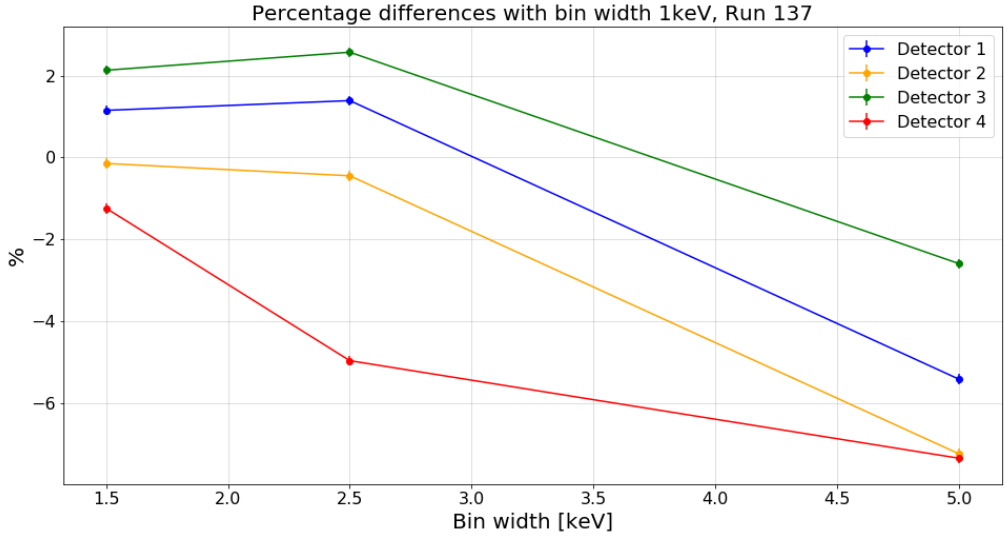

Figure 26: Percentage differences of counts for several bin widths with respect to counts for 1keV.

For detectors 1, 2 and 3, the best bin width seems to be 2.5keV, because the spectra look regular and smooth, and the fits seem to be well done. For detector 4, 2.5keV and 1.5keV both give a smooth spectrum, but the fits looks better with 1.5keV. Moreover, we can see that the spectrum for detector 4 is a bit different of the other ones. This detector has a better energy resolution, so the peaks look higher and narrower. It therefore seems logical to choose

a smaller bin width so that the four detectors have a comparable number of bins in the peak, and therefore a comparable number of points for the fit.

In addition, 2.5keV corresponds to the minimum of the convex curve on Figure 25 for detectors 1, 2 and 3, and 1.5keV seems to be a good intermediate value for the detector 4 because its curve for the number of counts is only increasing, and seems to be also a good intermediate value on Figure 25.

In conclusion, we set 2.5keV bins for detectors 1, 2 and 3, and 1.5keV bins for detector 4.

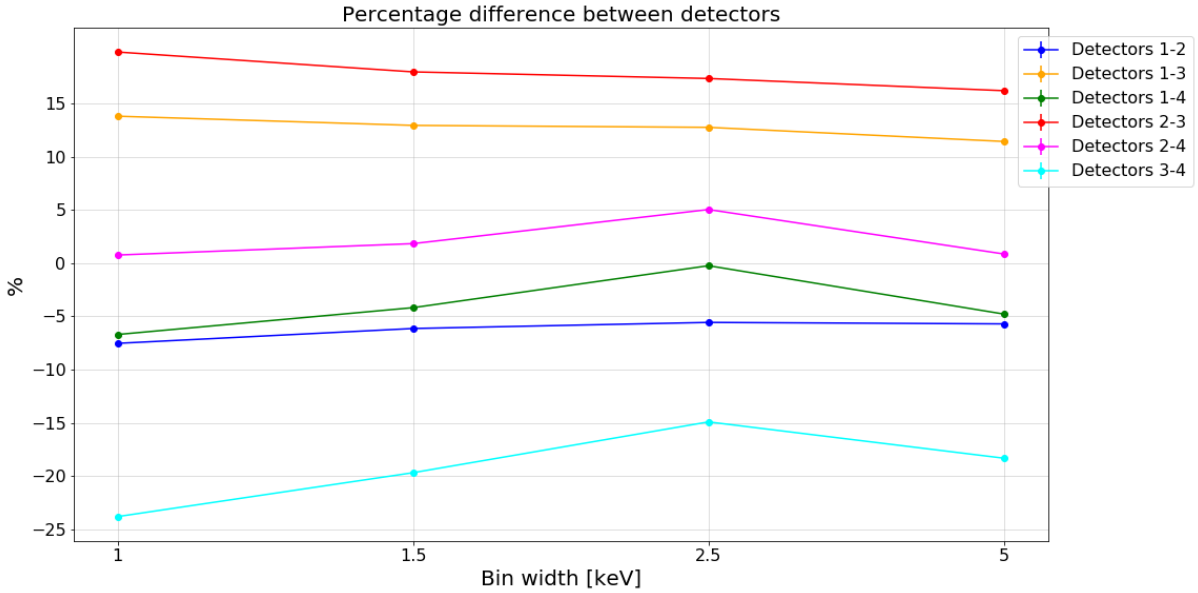

Figure 27: Percentage differences of counts between detectors for several bin widths.

Figure 27 shows the percentage differences between the detectors for each bin width tried. We can see that for all detectors the percentages vary depending on the bin width. The percentages including detector 4 are those which vary the most, since all other detectors were following the same trend except this one.

4.6.2 Starting point

We can try different energies to start the fitting of our histograms, and compare the fit results. We use the bin widths chosen previously which are 2.5keV bins for detectors 1, 2 and 3, and 1.5keV bins for detector 4.

As for the width of bins, we have tried extreme values for the starting fit energy: 150keV and 190keV. Figure 28 shows spectra of the peak we want to integrate and the fits for these values.

The more we start the fit on the left of the peak, the more we potentially take into account the contribution of the rest of the spectrum on the peak. However, we have seen that it was preferable to adjust the fit more on the right part of the peak. So 150keV seems to be a much too low value to start the fit. In addition, we see on Figure 28a that the top of the peak is not well included in the fit because the curve fits too much to the left of the peak. 190keV seems to be a better value, as almost only the left part of the peak is taken into account for the fit, and the curve seems to fit well on the top and on the right of the spectra. But maybe

this value is too close to the maxima, and to be sure, we are going to test some intermediate values again which are: 160keV, 170keV and 180keV.

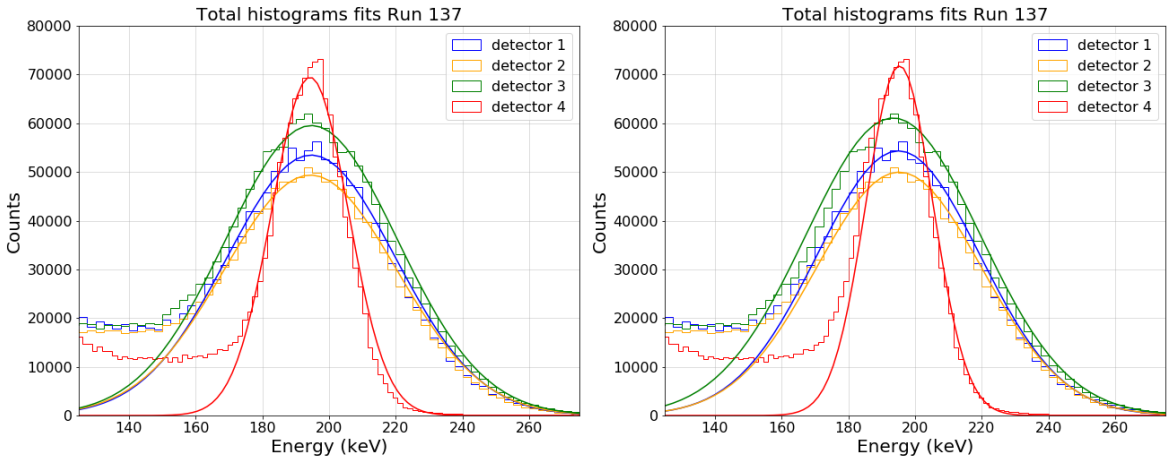

(a) Starting fit point = 150keV.

(b) Starting fit point = 190keV.

Figure 28: Histogram spectra for all detectors, Run 137, centered on the rightmost peak, with different starting points for the fit. 28a) starting fit point = 150keV, 28b) starting fit point = 190keV.

Figure 29 shows the spectra of all detectors for Run 137 with different values for the starting fit energy: 160keV, 170keV and 180keV.

On Figures 29a, 29b and 29c, we can't see important differences about the fit for detectors 1, 2 and 3. It seems that any of these values work fine. For detector 4, on the other hand, we can see that the closer we start the fit to the top of the peak, the more the fit surrounds the entire peak, and the more it matches the shape of the tail of the peak on the right. From these observations, it would seem that the best is to choose a value neither too close nor too far from the top of the peak.

The resulting number of counts for each detector for different starting fit energies for Run 137 are shown on Figure 30, and in Table 11 in Appendix A.

Again on Figure 30, the trend is similar for detectors 1, 2 and 3, for which counts decrease for a moment and then increase, while for detector 4, the counts only decrease as the energy increases. The gap between the curves of detectors 1, 2 and 3 stay almost stable, therefore the difference lies only in the behavior of detector 4. The curve of detector 4 is always between those of detectors 1 and 2 with a greater or smaller gap depending on the energies, except for the last point corresponding to 190keV. We can therefore exclude this value which seems too extreme.

Figure 31 shows the percentage differences between the numbers obtained starting the fit at 150keV which is the smallest value and the numbers obtained starting for the other values. For detectors 1, 2 and 3, the curves do not intersect, but the differences between them increase with the starting energy. The curve of detector 4, on the other hand, increases a lot, crossing

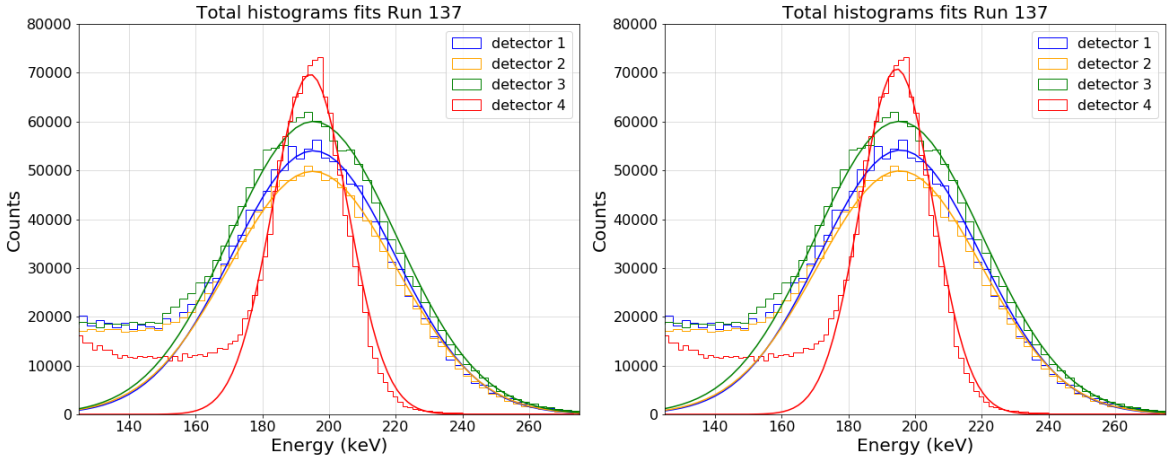

(a) Starting fit point = 160keV.

(b) Starting fit point = 170keV.

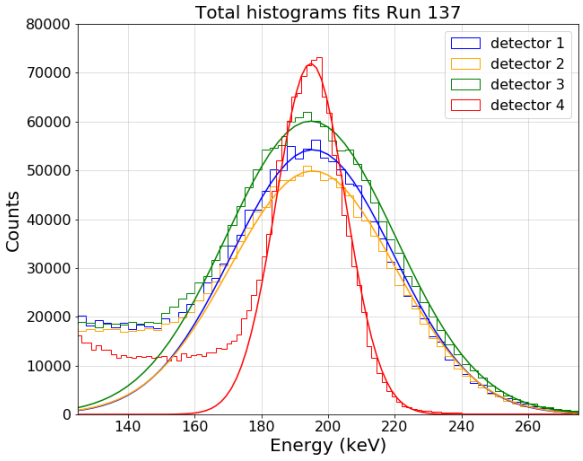

(c) Starting fit point = 180keV.

Figure 29: Histogram spectra for all detectors, Run 137, centered on the rightmost peak, with different starting points for the fit. 29a) starting fit point = 160keV, 29b) starting fit point = 170keV, 29c) starting fit point = 180keV.

all the others.

Looking at the spectra, it seems 150keV is too small a value for all detectors, and 190 seems to be too large a value. So it seems best to choose an intermediate value. There is not much difference for detector 1, 2 and 3 when starting at 160keV, 170keV or 180keV. 170keV seems to be a good intermediate value for detectors 1, 2 and 3, while 180keV seems better for detector 4 looking at the fit, and also because the peak is narrower, so it may be necessary to start fitting a bit after the others.

Figures 30 and 31 shows that the trend for the numbers of counts is similar for detectors 1, 2 and 3, and 170keV appears to be a good choice. For detector 4, 180keV appear to be a reasonable intermediate value.

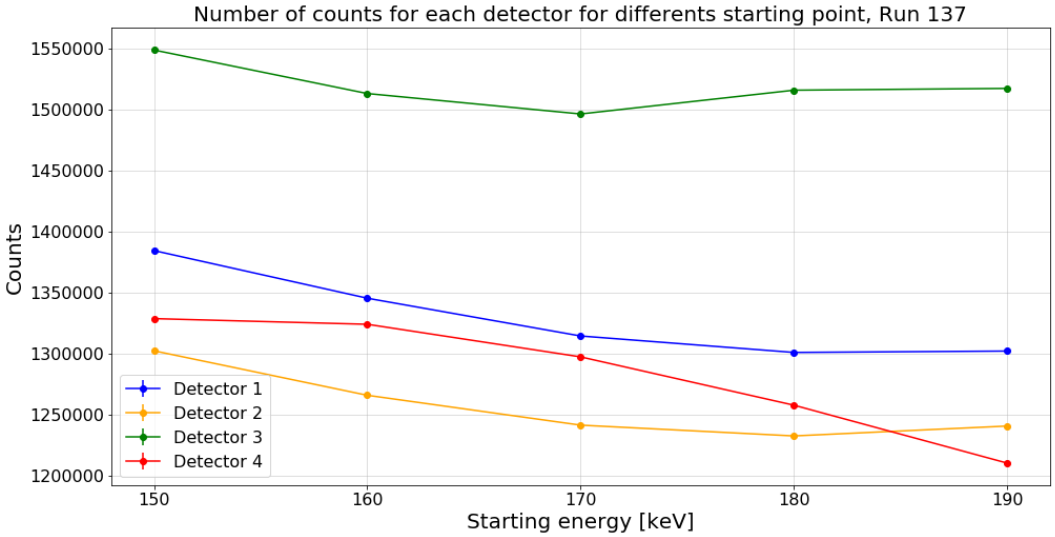

Figure 30: Number of counts for several starting fit energies.

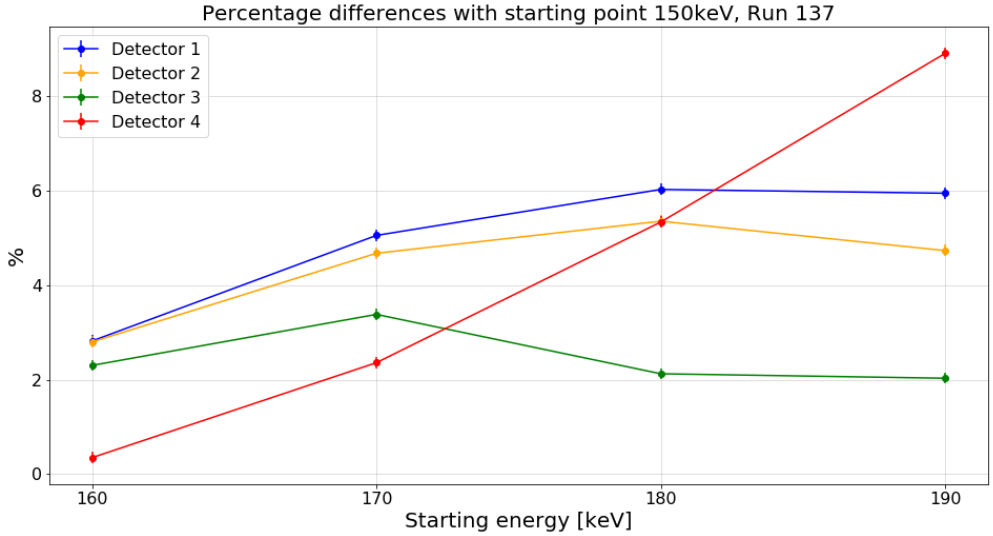

Figure 31: Percentage differences of counts for several starting fit energies with respect to counts for 150keV.

In conclusion, we chose to start fitting at 170keV for detectors 1, 2 and 3, and at 180keV for detector 4.

Figure 32 shows the percentage differences between the detectors for each energy we tried starting the fit. The percentages vary for all detectors, and some lines cross between 180keV

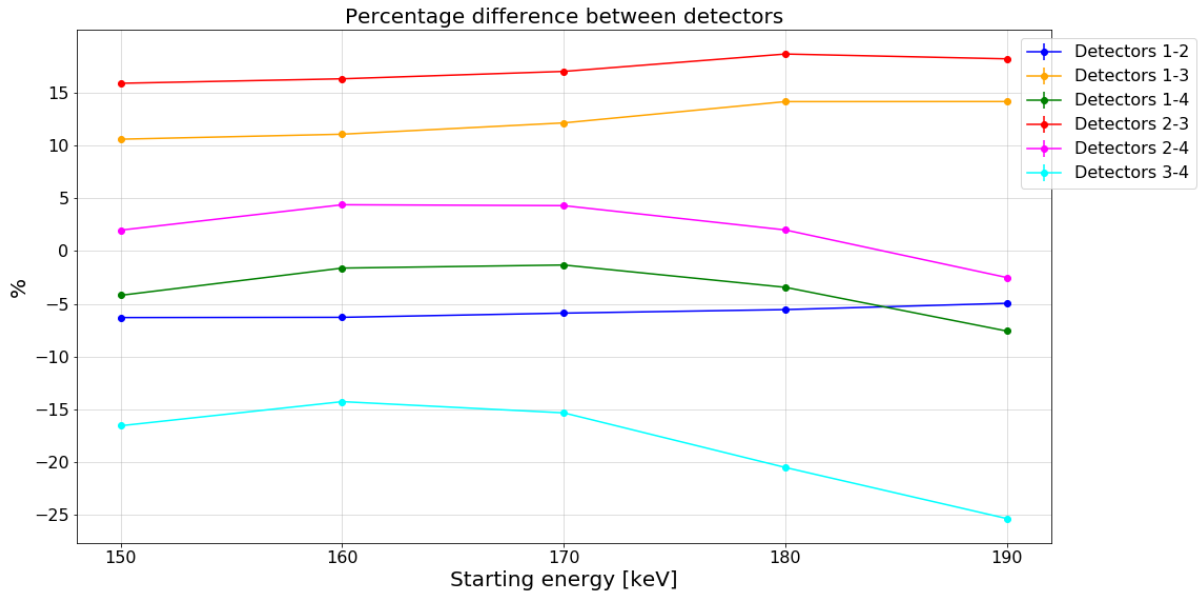

Figure 32: Percentage differences of counts between detectors for several starting fit energies.

and 190keV. The percentages including detector 4 follow the same trend, and the one not including it follows another trend. After 170keV these trends become very different, so this value is probably a good intermediate value.

4.6.3 Time separation bins

During the data analysis, we will separate the data in multiple time intervals. We can set the duration of these intervals, and see the fit results for the different intervals. We will compare the results for the following values: 10 seconds, 30 seconds, and 50 seconds. Figure 33 and Table 9 in Appendix A shows the number of counts obtained for each interval duration.

The number of counts are different for all the chosen intervals, but the trend remains the same. For each detector, the same increase is observed when the duration of the interval is increased, so the differences should therefore not have any influence on the percentage calculations.

Figure 34 shows the percentage differences between the numbers obtained for 10 seconds intervals with the numbers obtained for 30 seconds and 50 seconds intervals. Again, we see that the trend is exactly the same for all detectors.

To make sure to take into account the temperature drift, we chose to separate the data into 10 seconds intervals.

Figure 35 shows the percentage differences between the detectors for each time interval. In this case, the percentages between the detectors remain very stable as a function of the time interval. This shows that the choice of the interval does not affect the results of the percentage calculations.

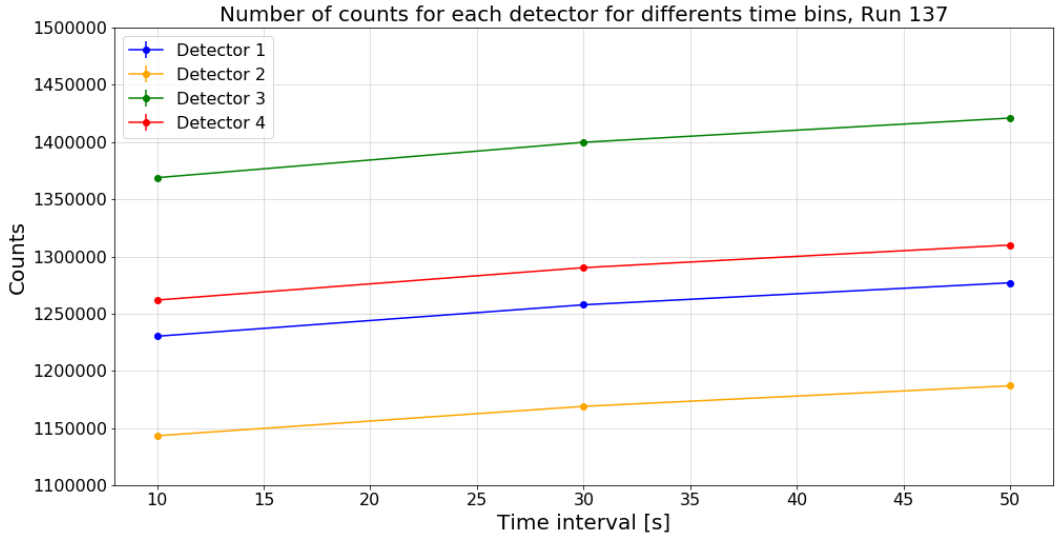

Figure 33: Number of counts between detectors for several time bins.

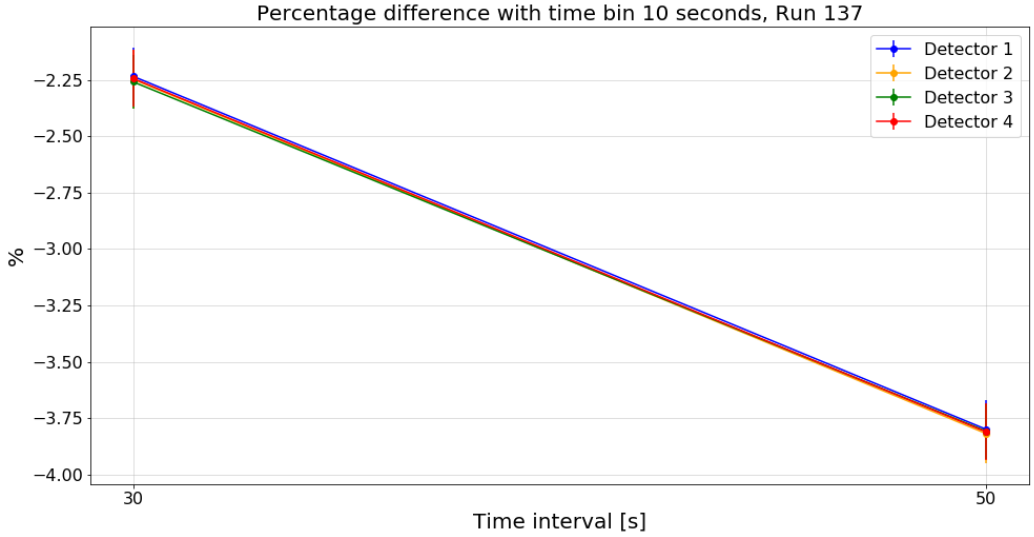

Figure 34: Percentage differences of counts for several time bins with respect to counts for 10 seconds.

4.7 Results

For simplicity, the results obtained after separating the data into 10 seconds intervals and integrating each of the corresponding histograms will be mentioned by *"10 second bin fits"* data.

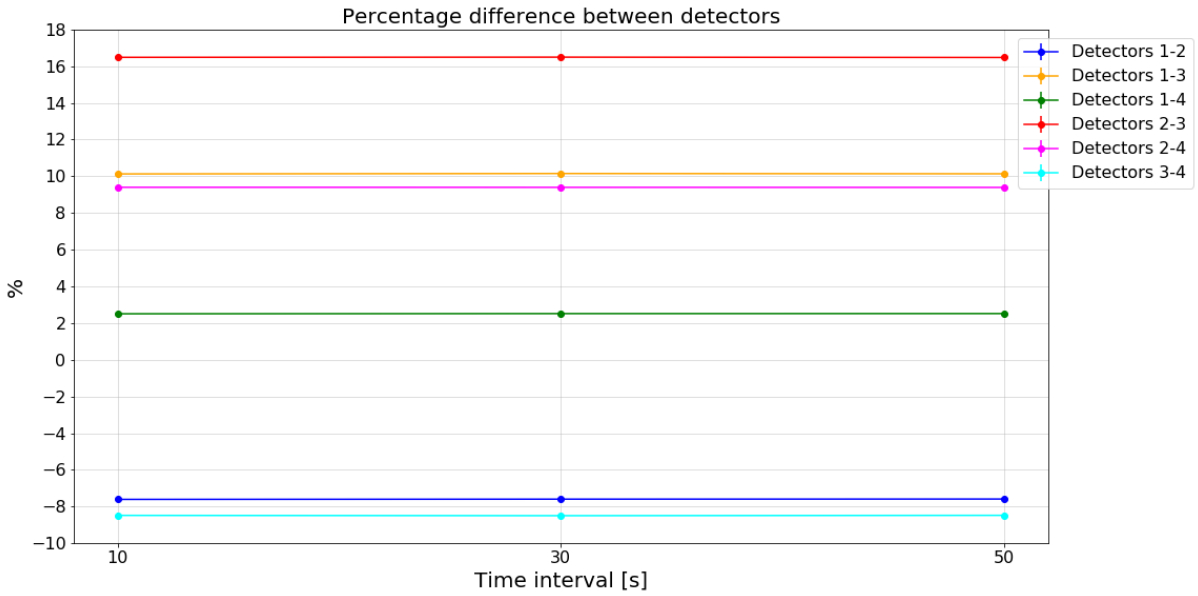

Figure 35: Percentage differences of counts between detectors for several time bins.

The results obtained by integrating the total spectrum containing all the data of a Run with a single Gaussian will be named *"One Gaussian total fit"* data.
And the numbers obtained by integrating the total spectrum containing all the data of a Run with three Gaussians will be called *"Three Gaussians total fit"* data.

4.7.1 Runs with ^{129m}Xe

In this section, we will study runs 137, 138, 139 and 140, where all conditions were stable and online analysis hinted at a spin polarization. The conditions during the running of these runs are summarized in Table 1.

Table 1: Runs 137-140.

Runs 137 to 140 for ^{129m}Xe				
	Run 137	Run 138	Run 139	Run 140
Magnetic field	on	off	on	off
Laser	on	on	on	on
Temperature	increasing fast	stable	stable	slowly decreasing

We now want to look for gamma asymmetries by comparing different runs, taken in the same conditions, but some with magnetic field on, and some with magnetic field off. Here, we will study four runs from 137 to 140. For these runs, we were using ^{129m}Xe. We can especially compare runs 138 and 139 since they took place under the same temperature conditions, with the only difference being the magnetic field on or off (so presence and absence of polarization).

Runs 137 to 140 were taken without breaks between and by only changing the settings. Detector 1 was placed 3 centimeters above the oven, Detector 2: 4.5 centimeters on the side, and detectors 3 and 4: 6 centimeters behind the oven.

We begin with run 137, which is the one during which we were increasing the temperature of the sample. The laser and the magnetic field were also on. After we ended heating the sample, the heater was stopped to begin run 138 with stable temperature. The laser was still on, but the magnetic field was off. Then, run 139 is the same as run 138 but with the magnetic field turned on. Finally, we let the temperature decrease during run 140. The magnetic field was turned off.

4.7.1.1 *10 second bin fits* and *One Gaussian total fit* comparison

Figure 36 shows the spectra for runs 137 to 140 for each detector, and Figures 37 and 38 the fitted average number of counts per second for *10 second bin fits* and *one Gaussian total fit*. Tables 12 and 13 in Appendix D shows the numbers. This is an occasion to see that these two methods give comparable but still different results.

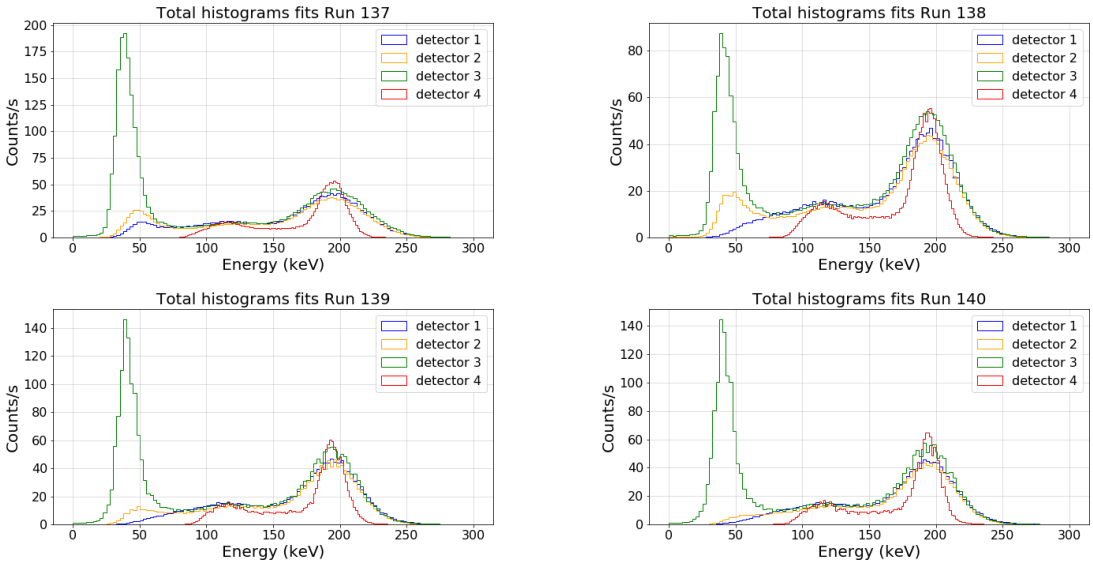

Figure 36: All data histogram spectra for all detectors for runs 137, 138, 139 and 140, with energy calibration. Detectors 1 and 2: transverse. Detectors 3 and 4: longitudinal.

On Figures 37 and 38 showing the number of counts per second for *10 second bin fits* and *one Gaussian total fit*, the biggest difference is in the numbers corresponding to Run 137. This could be explained by the fact that the temperature was increasing fast, as mentioned in Figure 1, thus causing a significant energy drift. This drift is taken into accounts with *10 second bin fits*, but not with *one Gaussian total fit*, which could explain this big difference.

We can also see a slight increase in the number of counts for detectors 1 and 2 (the transversal ones) between Runs 138 and 139, and a decrease for detectors 3 and 4 (the longitudinal ones), for both methods. This is also noticeable on Figures 39 and 40 showing the percentages differences between Runs 138 and the others for each detector. The percentage differences between the runs are shown in Tables 16 and 17 in Appendix D.

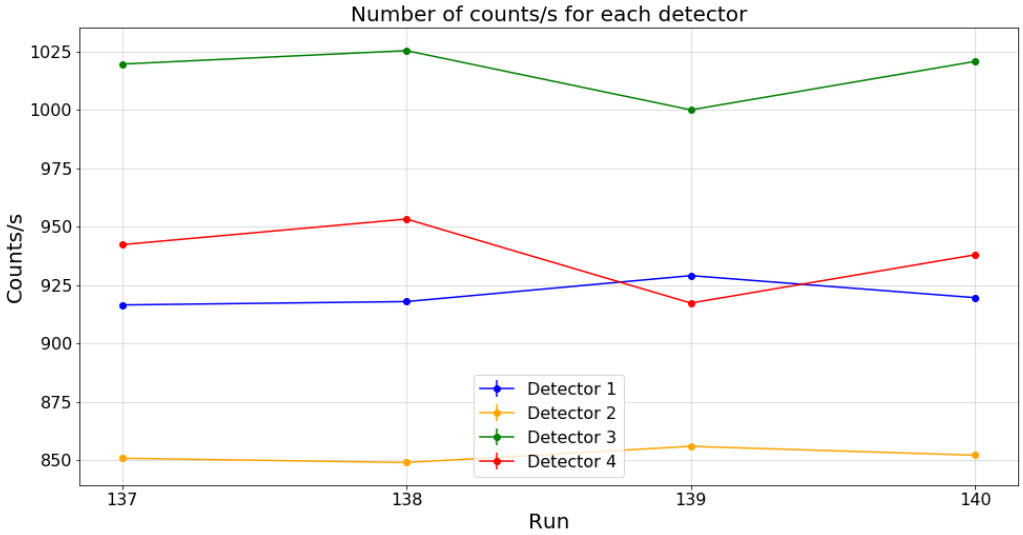

Figure 37: Average number of counts per second obtained with *10 second bin fits* for Runs 137, 138, 139 and 140. Detectors 1 and 2: transverse. Detectors 3 and 4: longitudinal.

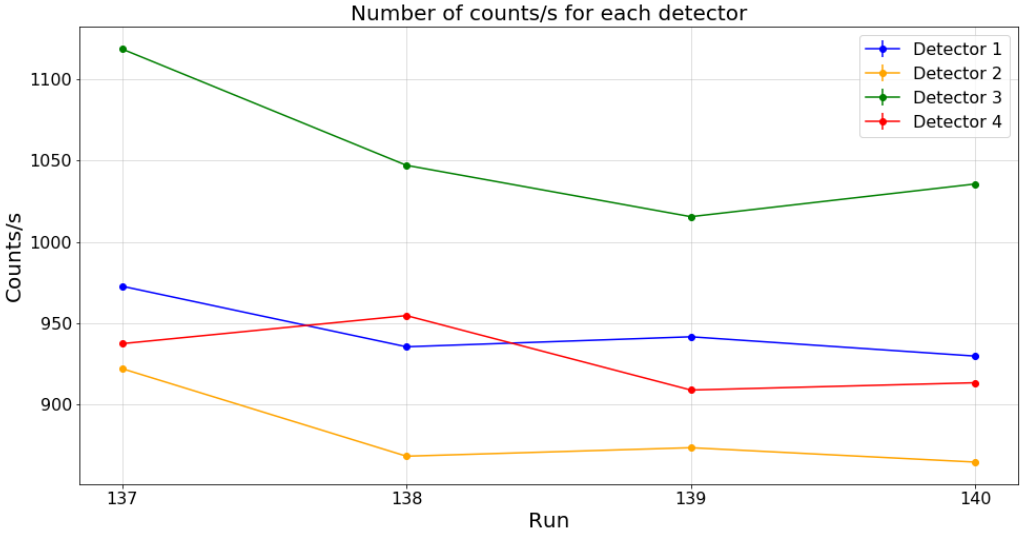

Figure 38: Average number of counts per second obtained with *one Gaussian total fit* for Runs 137, 138, 139 and 140. Detectors 1 and 2: transverse. Detectors 3 and 4: longitudinal.

The percentages obtained for the two methods are different due to the differences of the two methods, again especially for Run 137 during which the heaters were on, which was therefore subject to drastic changes in temperature inducing energy drifts. We will generally compare runs 138 and 139, since they were taken at equal and constant temperature, while

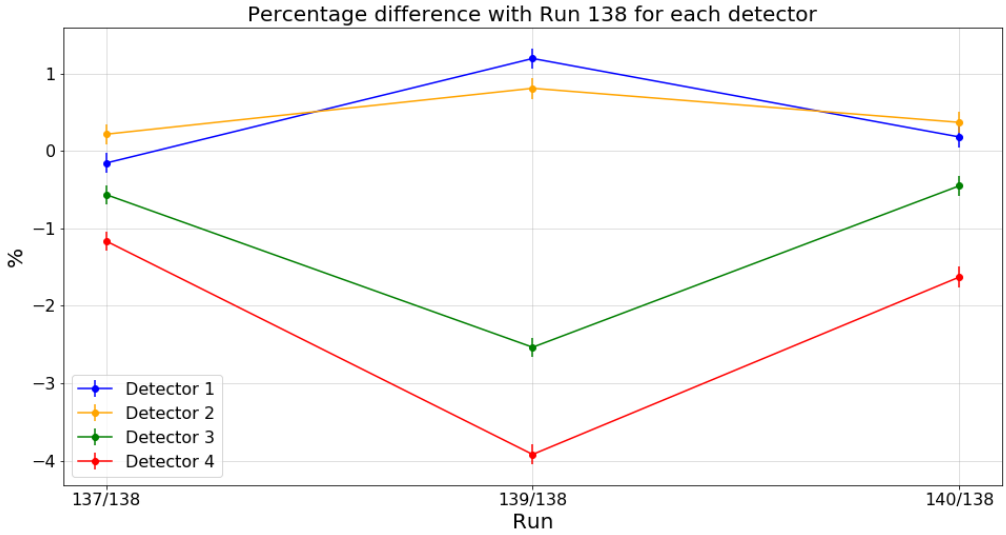

Figure 39: Percentage differences of counts per second obtained with *10 second bin fits* for Runs 137, 138, 139 and 140. Detectors 1 and 2: transverse. Detectors 3 and 4: longitudinal.

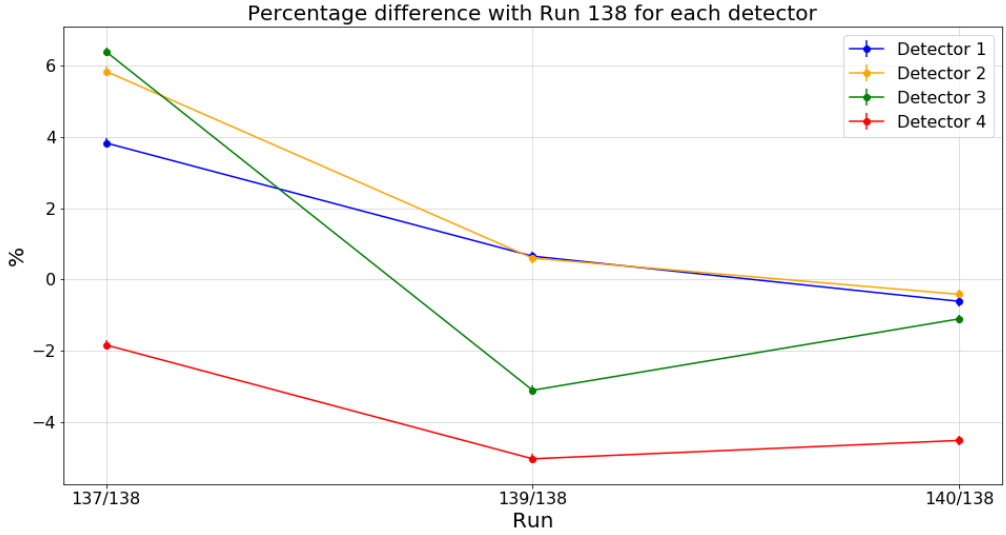

Figure 40: Percentage differences of counts per second obtained with *one Gaussian total fit* for Runs 137, 138, 139 and 140. Detectors 1 and 2: transverse. Detectors 3 and 4: longitudinal.

runs 137 and 140 were subject to temperature changes.

On Figure 39 showing the percentage differences for *10 second bin fits*, we can see an increase of around 1% for the transverse detectors (1 and 2) between the differences for runs

137 and 138 and runs 138 and 139, and then a decrease of again around 1% for runs 138 and 140.

We can also see an decrease of around $2-3\%$ for the longitudinal detectors (3 and 4) between the differences for runs 137 and 138 and runs 138 and 139, and then an increase of again of the same order of magnitude for runs 138 and 140.

If we ignore Run 137, the most important thing is the difference in results between runs 138 and 139, taken under identical conditions, with only one difference being the magnetic field (on for Run 139, off for Run 138, see again Table 1). The differences between runs 138 and 140 are much smaller.

Still ignoring Run 137, Figure 40 shows similar trends: decrease for the transverse detectors (1 and 2) between the differences for runs 138 and 139 and runs 138 and 140, and an increase for the longitudinal detectors (3 and 4).

We can go further to emphasize these changes in the counts by calculating the percentage of differences between two detectors for the same run, and then comparing the results for the four runs, using formula 12. For example, the calculations were done following: $D_1(det_1, det_N) = \frac{N_1(det_N) - N_1(det_1)}{N_1(det_N)} \cdot 100$. The results for the two methods are shows in Figures 41 and 42, and also in Tables 20 and 21.

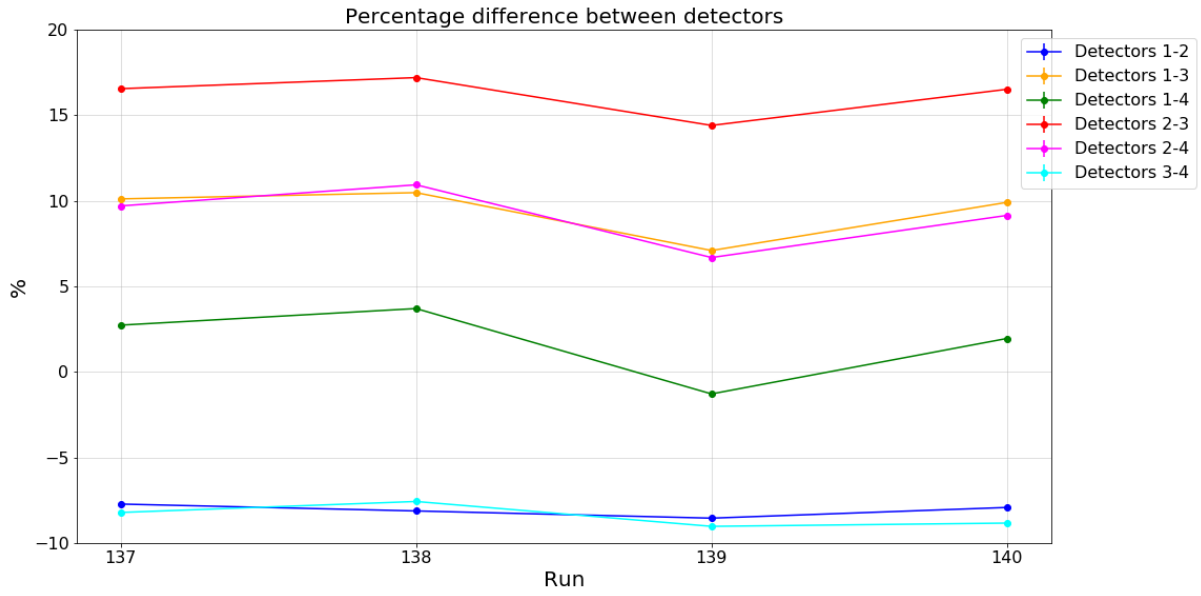

Figure 41: Percentage differences of counts per second between detectors obtained with *10 second bin fits* for Runs 137, 138, 139 and 140. Detectors 1 and 2: transverse. Detectors 3 and 4: longitudinal.

Here, the results we were discussing previously are highlighted. On Figure 41 for *10 second bin fits*, we see that the percentages between detectors 1 and 2 (transverse/transverse) and between detectors 3 and 4 (longitudinal/longitudinal) remain almost perfectly stable. The other differences, between a transverse and a longitudinal detector, all show the same trend: they increase between Run 137 and 138, decrease between Run 138 and 139, and increase again between Run 139 and 140. This shows that the application of a magnetic field may influence

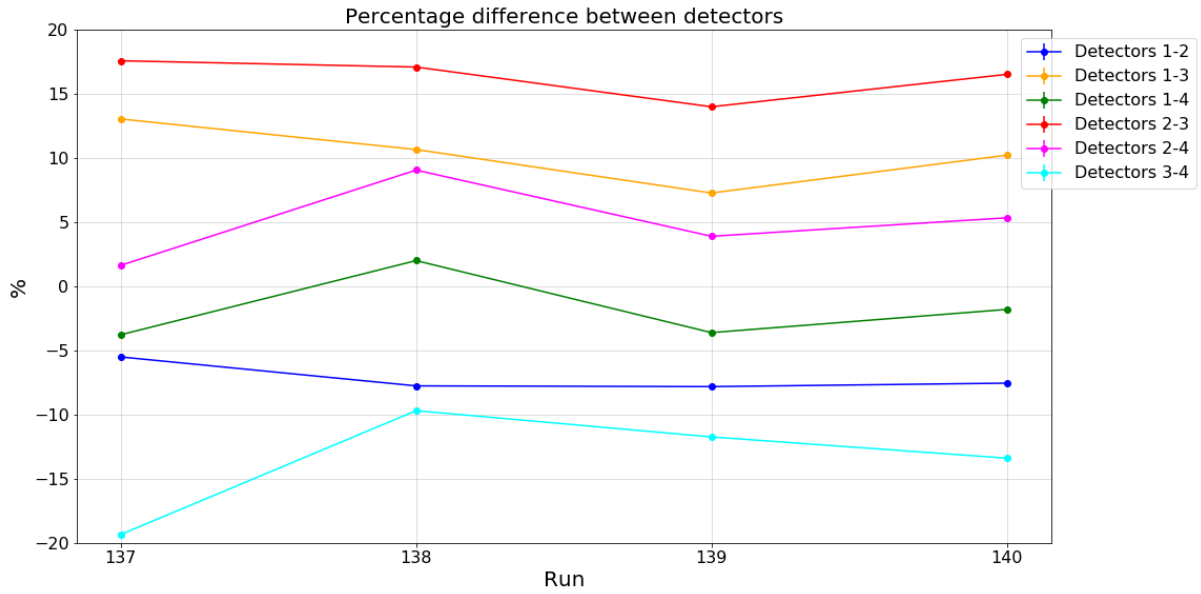

Figure 42: Percentage differences of counts per second between detectors obtained with *one Gaussian total fit* for Runs 137, 138, 139 and 140. Detectors 1 and 2: transverse. Detectors 3 and 4: longitudinal.

number of counts reaching each detector (which we expect when orienting the nuclear spins).

Results shown on 42 for *one Gaussian total fit* are a little less clear. We will again ignore the results of Run 137 in this case. Here again, the percentages between detectors 1 and 2 (transverse/transverse) are stable, but it is not the case for the percentages between detectors 3 and 4 (longitudinal/longitudinal), which decrease only. Apart from that, we can still observe that the differences between a transverse and a longitudinal detector show again the same trend: they increase between Run 137 and 138, decrease between Run 138 and 139, and increase again between Run 139 and 140.

We tried to show an overview of the effect of the magnetic field (which should be equivalent to the presence of spin orientation) on the number of counts detected on Figure 43, which shows a spectrum of the average number of gammas counted per second for runs 138 and 139 for each detectors. However, the changes (supposedly very small) are not obvious on the spectra.

As we did before, Figure 44 shows the number of counts per 10 second interval for runs 138 and 139 on the same graph, one after the other, so one can see the changes.

We can clearly see a decrease in the count numbers for detectors 3 and 4 when Run 139 begins and the magnetic field is turned on (see Figure 1). We can also observe a slight increase for detectors 1 and 2.
On Figure 45, we made the same graph, but with the differences between the detectors.

The differences between detectors 1 and 2 (transverse/transverse) and 3 and 4 (longitudinal/longitudinal) seem to remain fairly stable, while the others (transverse/longitudinal) all

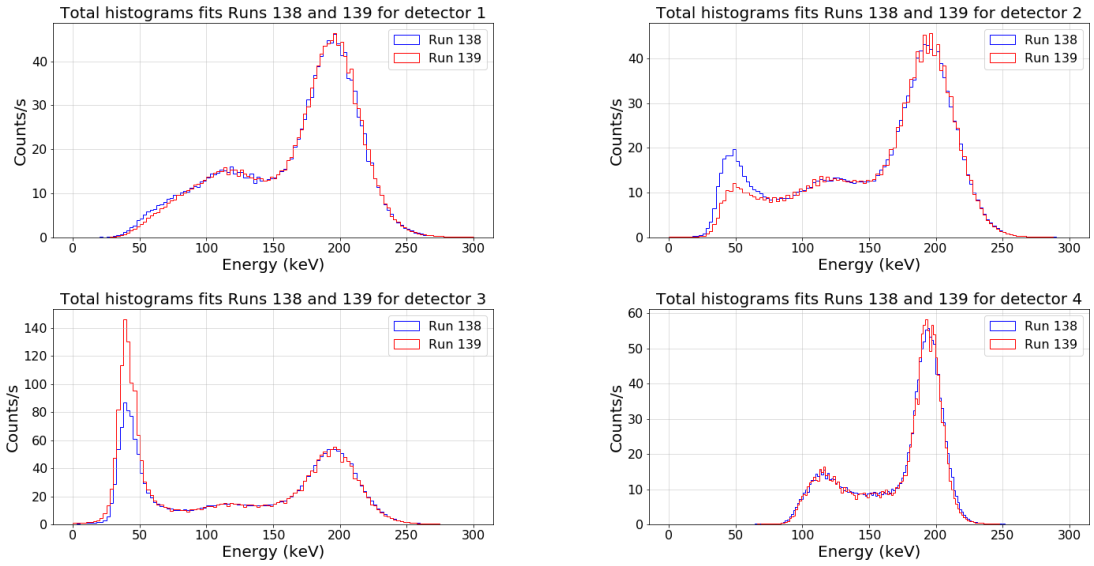

Figure 43: Superposition of all data histogram spectra for all detectors for runs 138 and 139, with energy calibration. Detectors 1 and 2: transverse. Detectors 3 and 4: longitudinal.

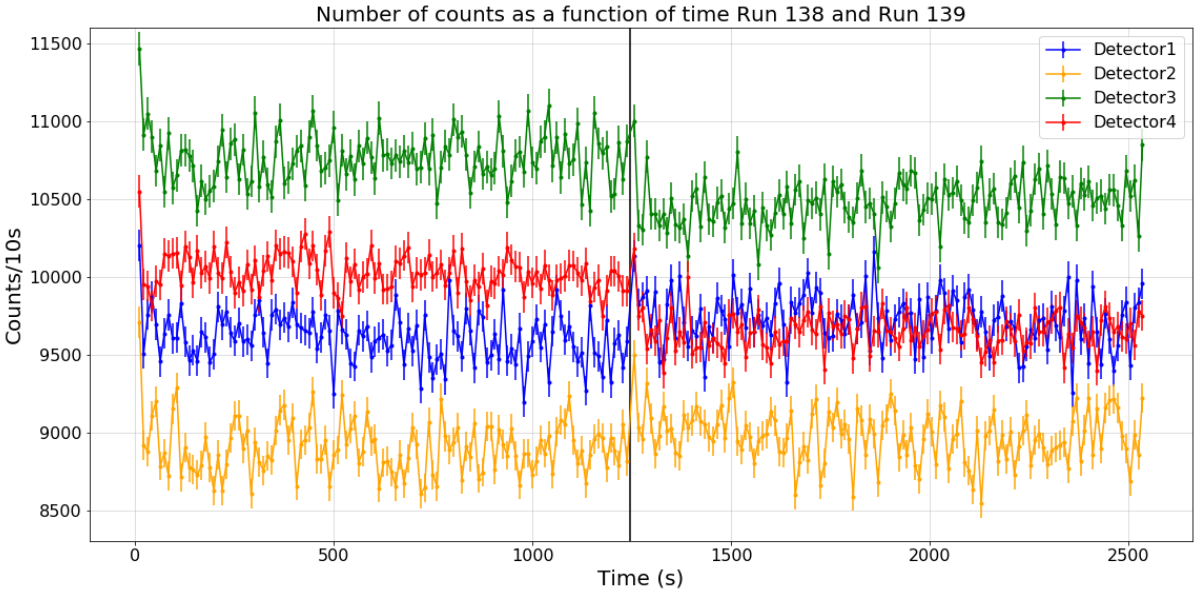

Figure 44: Number of 197keV in ^{129m}Xe counts as a function of time for all detectors, runs 138 and 139. The **Black** lines show the moment when Run 138 ends and Run 139 begins. Detectors 1 and 2: transverse. Detectors 3 and 4: longitudinal.

decrease.

Figure 45: Percentage differences of counts as a function of time, runs 138 and 139. The **Black** lines show the moment when Run 138 ends and Run 139 begins. Detectors 1 and 2: transverse. Detectors 3 and 4: longitudinal.

4.7.1.2 *Three Gaussians total fit* results

We made the same calculations of percentages of differences between runs with the numbers obtained for *"three Gaussians total fit"*. The number of counts are shown in Figure 46 and Table 18 in Appendix D. The percentage differences with Run 138 are shown in Figure 47 and the percentage differences between the runs are shown in Table 18 in Appendix D.

We immediately see that the results, whether the numbers of counts or the percentages of differences, do not show the same trends as for the previous methods. For the number of counts on Figure 46, we can actually see a decrease followed by an increase for detectors 3 and 4 (longitudinal) between runs 138 and 140, but detectors 1 and 2 (transverse) do not show the expected behavior.

For the percentages of differences on Figure 47, again detectors 3 and 4 (longitudinal) show an decrease between the differences for runs 137 and 138 and runs 138 and 139, and an increase for the differences for runs 138 and 140. Detectors 1 and 2 (transverse) should do the opposite to match previous results, but they are not: detector 2 also decreases and increases, and detector 1 only decrease. These results are therefore not completely in agreement with those of the other methods.

We have again calculated the percentages of differences between the detectors within the same run, and the results shown on Figure 42, and in the Appendix D on Table 22.

On Figure 48 some detectors show the expected behaviors, and others do not. The differences between detectors 1 and 2 (transverse) and detectors 2 and 4 (longitudinal) should remain stable, but are not, even ignoring Run 137. The other differences should increase, decrease and then increase again to match the previous results, but only the difference between detectors 1 and 4 shows this trend. If we ignore run 137, we can include the difference

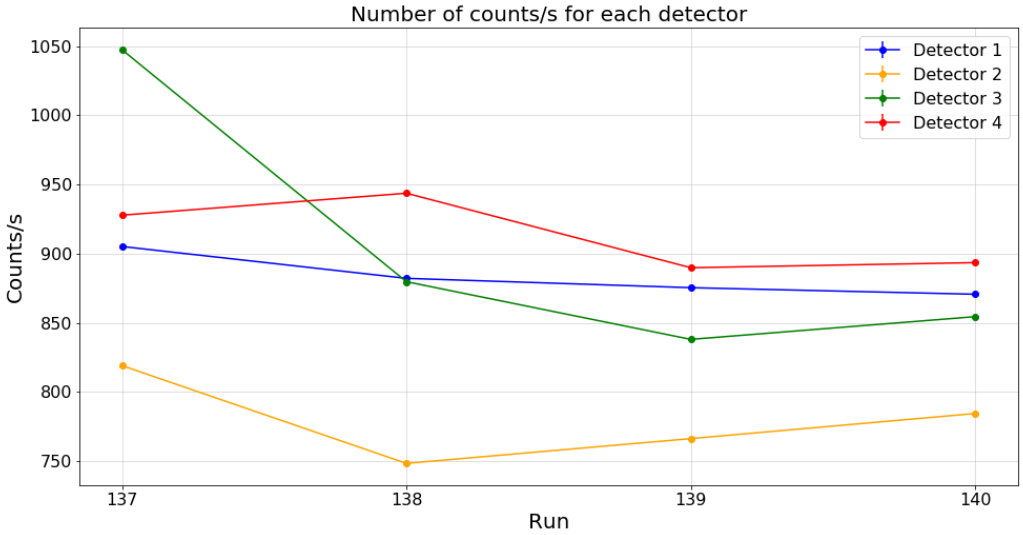

Figure 46: Average number of counts per second obtained with *"three Gaussians total fit"* for Runs 137, 138, 139 and 140. Detectors 1 and 2: transverse. Detectors 3 and 4: longitudinal.

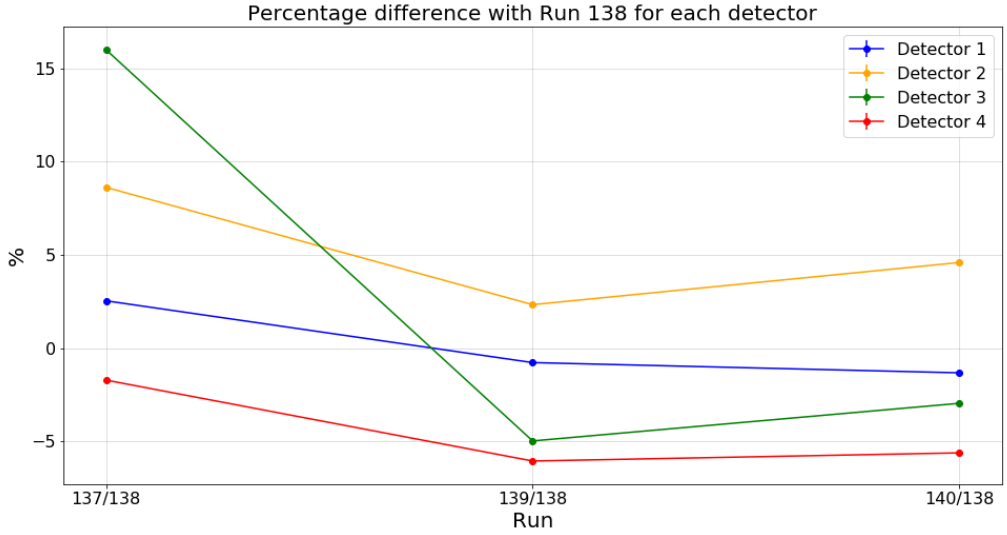

Figure 47: Percentage differences of counts per second between detectors obtained with *"three Gaussians total fit"* for Runs 137, 138, 139 and 140. Detectors 1 and 2: transverse. Detectors 3 and 4: longitudinal.

between detectors 1 and 3, but this is not enough to declare that these results are similar to the previous ones.

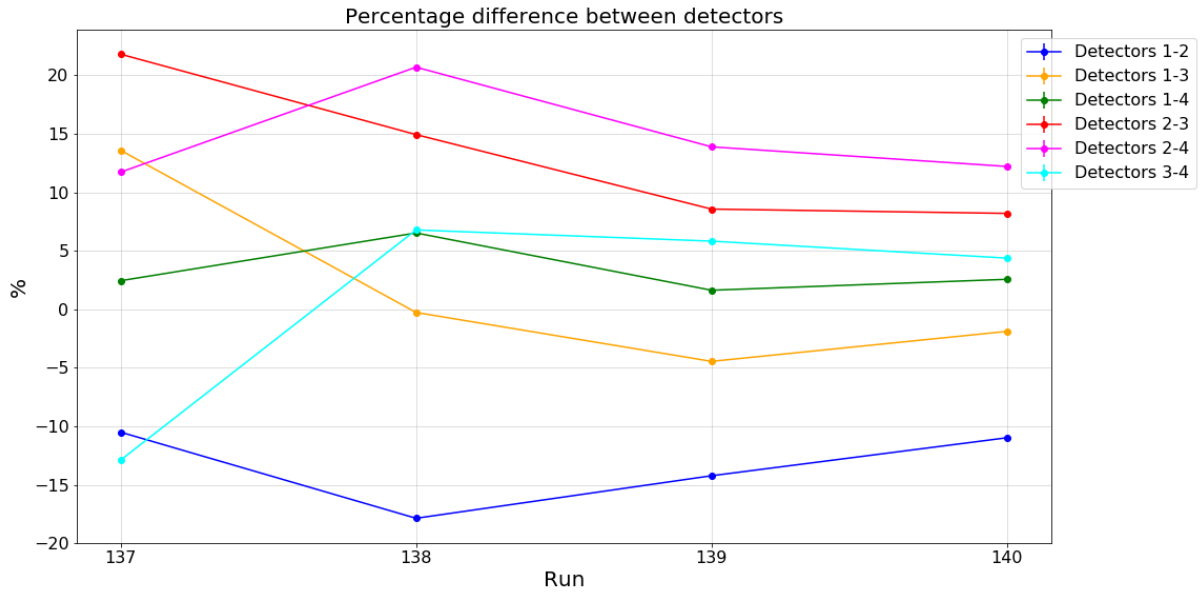

Figure 48: Percentage differences of counts per second between detectors obtained with *"three Gaussians total fit"* for Runs 137, 138, 139 and 140. Detectors 1 and 2: transverse. Detectors 3 and 4: longitudinal.

However, it is possible to observe that this method for fitting a spectrum is not the most suitable when one does not know exactly the shape and the nature of the spectrum. Figure 49 shows the spectrum for detector 1 of run 137. Figure 49a shows the spectrum fitted with three Gaussians, And Figure 49a shows the three Gaussians obtained by taking the parameters of the fit.

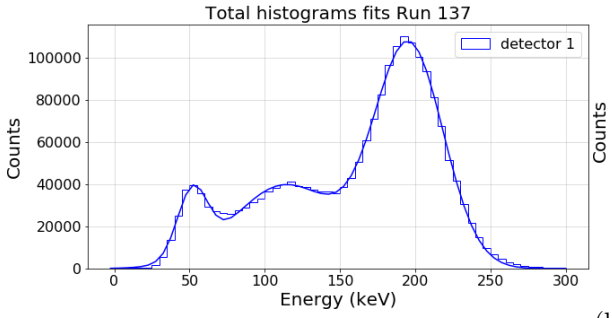

(a) Run 137, detector 1, spectra with three Gaussians fit.

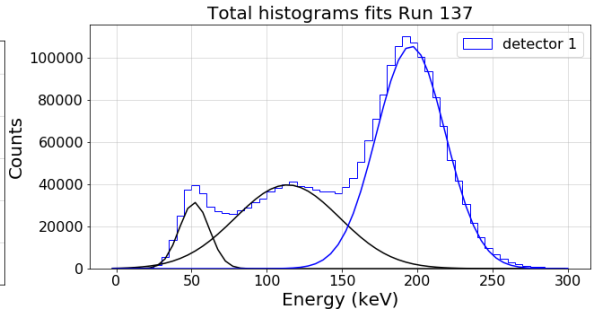

(b) Run 137, detector 1, spectra with the three Gaussians obtained by taking the parameters of the fit.

Figure 49: Spectra for detector 1, Run 137.

We can assume that there are several combinations of parameters giving a suitable fit as in Figure 49a, and small changes in the parameters of one of the three peaks on Figure 49b

can greatly influence the parameters of the other two. It is therefore impossible to certify that this combination (and therefore the results of the integration) are correct.

4.7.1.3 *drift correction fits* results

We can try one last approach we will call *"drift correction fits"*. Previously, when we separated the data in 10 second intervals, we calibrated and integrated each spectrum individually. We can, after calibrating all the 10 second interval spectra, add them together. Thus, we obtain a spectrum containing all the data, with the temperature drift corrected. The advantage is that, rather than fitting and integrating multiple spectra with little data, we integrate a single one with lots of data, which avoids systematic errors and reduces uncertainties. Figure 50 shows the difference between spectra containing data without correction for the temperature drift with spectra obtained with this approach for Run 137 which showed a great energy drift due to the temperature increase.

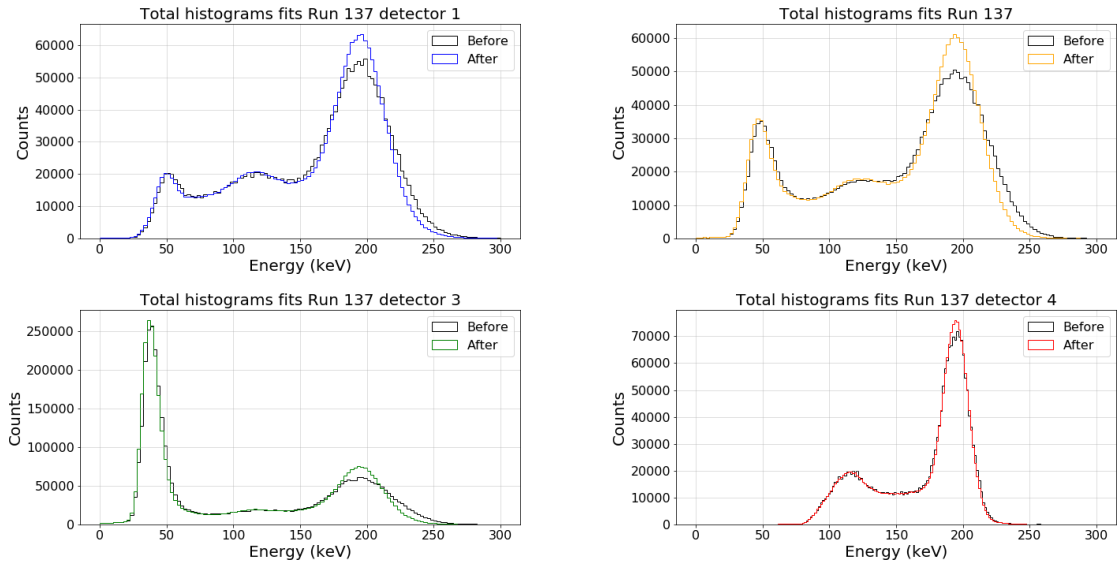

Figure 50: Run 137, differences between total spectra before the thermal drift correction and after for all detectors. The **Black** spectra are those before the correction, with data calibrated in energy. The others are those after the correction of the **Black** spectra.

Figure 51 shows the number of counts per second obtained by fitting and integrating the rightmost peaks of these spectra for runs 137, 138, 139 and 140 with a single Gaussian, and the corresponding numbers are shown in Table 15 in Appendix D.

On Figure 51, we observe a slight increase in the number of counts for detectors 1 and 2 between runs 137 and 138, then a decrease between runs 138 and 139, and finally an increase again between runs 139 and 140. For detectors 3 and 4, we observe the complete opposite. Between runs 137 and 138, the number of counts increases slightly, then decreases between runs 138 and 139, and finally increases again between runs 139 and 140. As a reminder, as shown in Table 1, the magnetic field was on for runs 137 and 139, and off for runs 138 and 140, and detectors 1 and 2 are transverse, and detectors 3 and 4 are longitudinal. Therefore, what we observe in the Figure is what we might expect: an increase in the counts for the transverse

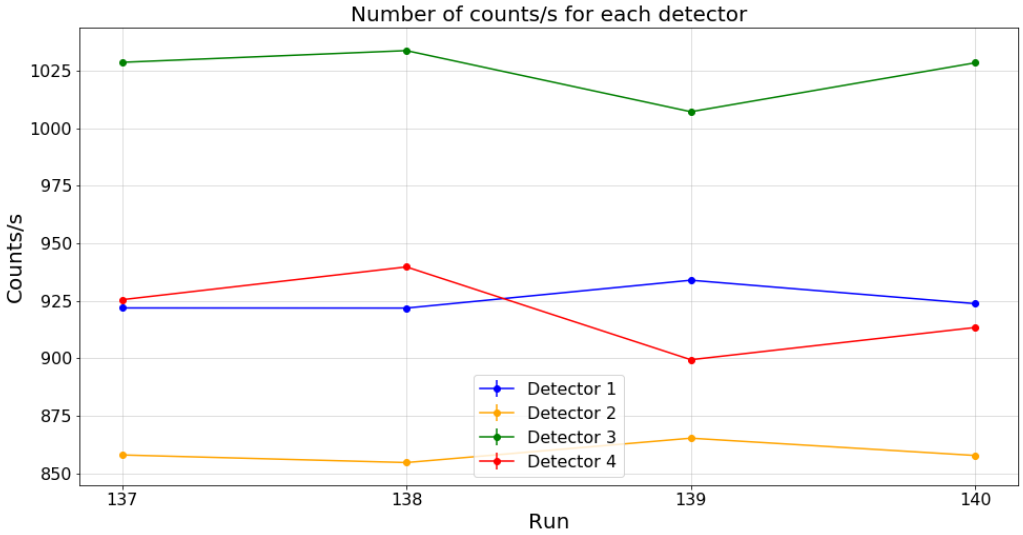

Figure 51: Average number of counts per second obtained with *"drift correction fits"* for Runs 137, 138, 139 and 140. Detectors 1 and 2: transverse. Detectors 3 and 4: longitudinal.

detectors when the magnetic field is on and an decrease for the longitudinal detectors, and the reverse when the magnetic field is off.

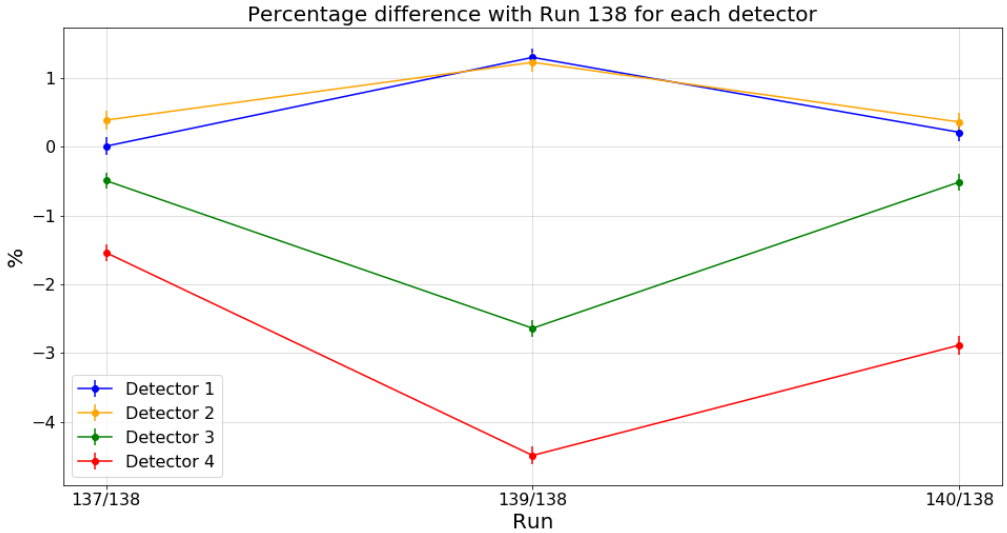

Figure 52: Percentage differences of counts per second obtained with *drift correction fits* for Runs 137, 138, 139 and 140. Detectors 1 and 2: transverse. Detectors 3 and 4: longitudinal.

Figure 52 shows the percentages of differences between the counts of runs 137, 139 and 140 with the counts of Run 138. The percentage difference numbers between runs are shown in Table 19 in Appendix D.

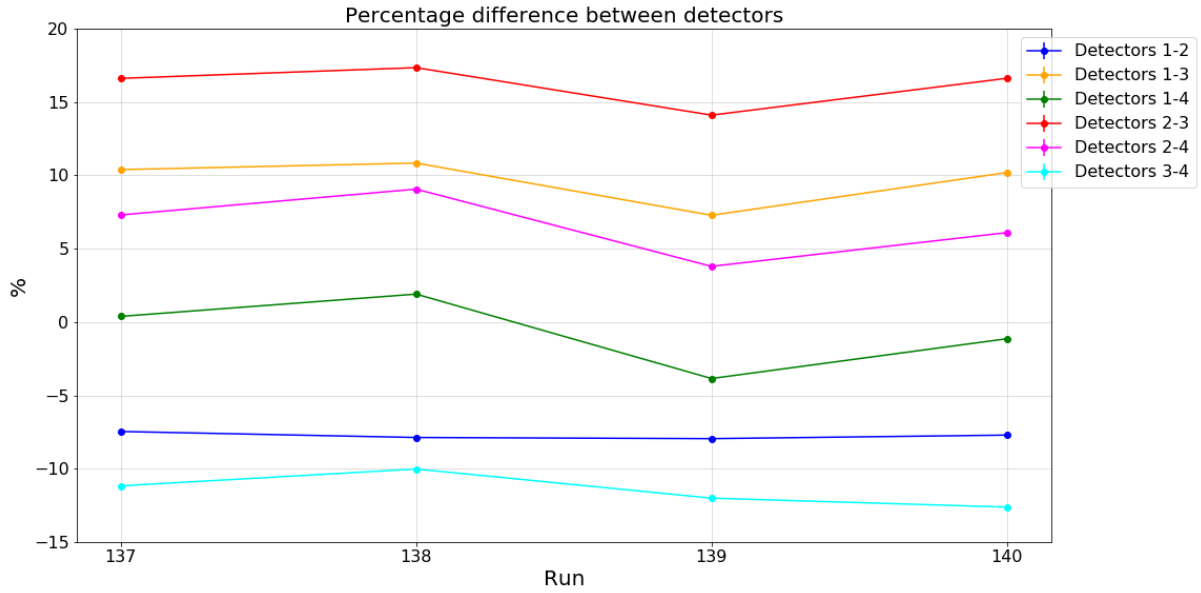

Figure 53: Percentage differences of counts per second between detectors obtained with *drift correction fits* for Runs 137, 138, 139 and 140. Detectors 1 and 2: transverse. Detectors 3 and 4: longitudinal.

We calculated again the differences between the detectors within a run in order to compare these differences between runs. Figure 53 shows these percentage differences between detectors for each of the four runs, and the numbers are shown in Table 23 in Appendix D. We expect the differences between two longitudinal or two transverse detectors to stay stable. We see that the differences between detectors 1 and 2 (transverse) remain fairly stable, and the differences between detectors 3 and 4 are a little less stable, but still vary less than the others. We also observe that the differences between a transverse detector and a longitudinal detector increase when the magnetic field is on, and decrease when it is off.

These results therefore match with those we had with *10 second bin fits* and *One Gaussian total fit* data.

4.7.2 Runs with ^{131m}Xe

In order to confirm the promising results we had for Runs 137 to 140, we would like to find a similar feature with other runs, with ^{131m}Xe this time. We therefore selected two other runs, 161 and 163, taken in the similar conditions as Runs 138 and 139, but with detectors moved a bit further. Detector 1 was 8.5 centimeters from the oven, detector 2: 6.5 centimeters, and detectors 3 and 4: 10 centimeters from the oven.

Run 161 is the equivalent of Run 138. The sample have been previously heated so the temperature was stable, and the magnetic field off. Then, for Run 163, as for Run 139, the

Table 2: Runs 161 and 163.

Runs 161 and 163 for ^{131m}Xe		
	Run 161	Run 163
Magnetic field	on	off
Laser	on	on
Temperature	stable	stable

magnetic field is turned on. These conditions are summarized in the Table 2. The total spectra of these two runs are shown on Figure 54.

4.7.2.1 *10 second bin fits* and *One Gaussian total fit* comparison

As previously, Figure 54 shows the spectra for these runs for each detector, and Figures 55 and 56 give the average number of counts per second for *10 second bin fits* and *one Gaussian total fit*. Tables 24 and 25 in Appendix D shows the corresponding numbers.

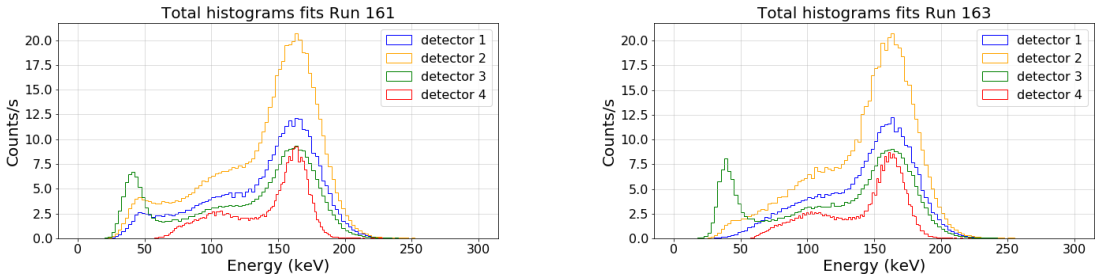

Figure 54: All data histogram spectra for all detectors for runs 161 and 163, with energy calibration. Detectors 1 and 2: transverse. Detectors 3 and 4: longitudinal.

Figures 55 and 56 seem to show very similar results, but the changes are very small, so we can directly look at the percentages differences between the two runs in Tables 28 and 29 for the two approaches.

Contrary to the previous runs, we do not have here a visible increase in counts for the transverse detectors in presence of the magnetic field, nor a decrease for the longitudinal detectors. Changes seem more random. We can draw the same conclusions by looking at the spectra comparing the counts per second for runs 161 and 163 in Figure 57. We do not clearly see more counts in one run than in the other for any detector.

Once again, we made the calculations of percentages of differences between detectors for the two methods, and the results are shown in Figures 58 and 59. Tables 32 and 33 in Appendix D show the numbers.

In this case, these calculations reveal nothing more and do not meet our expectations since most of the percentage differences remain stable between the two runs, or change very subtly,

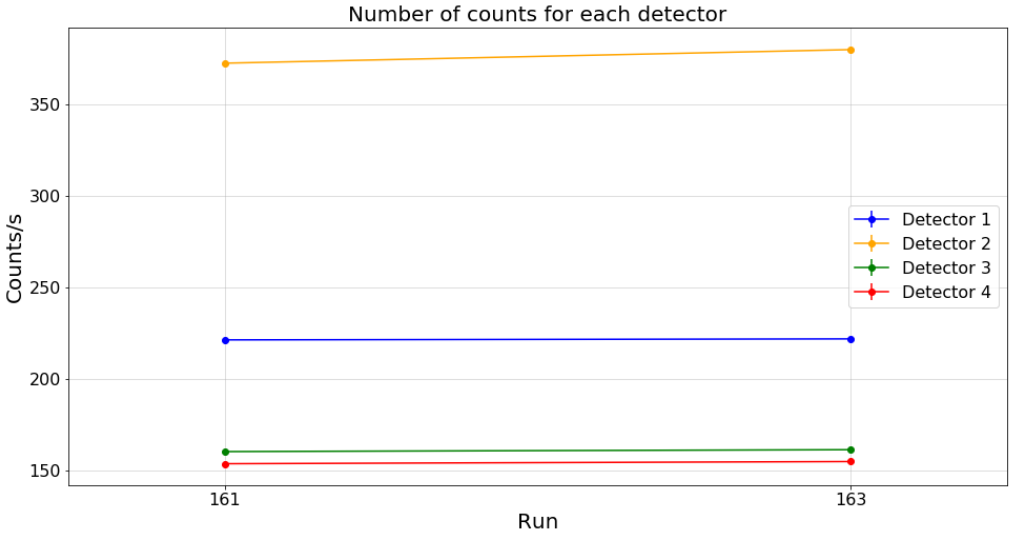

Figure 55: Average number of counts per second obtained with *10 second bin fits* for Runs 161 and 163. Detectors 1 and 2: transverse. Detectors 3 and 4: longitudinal.

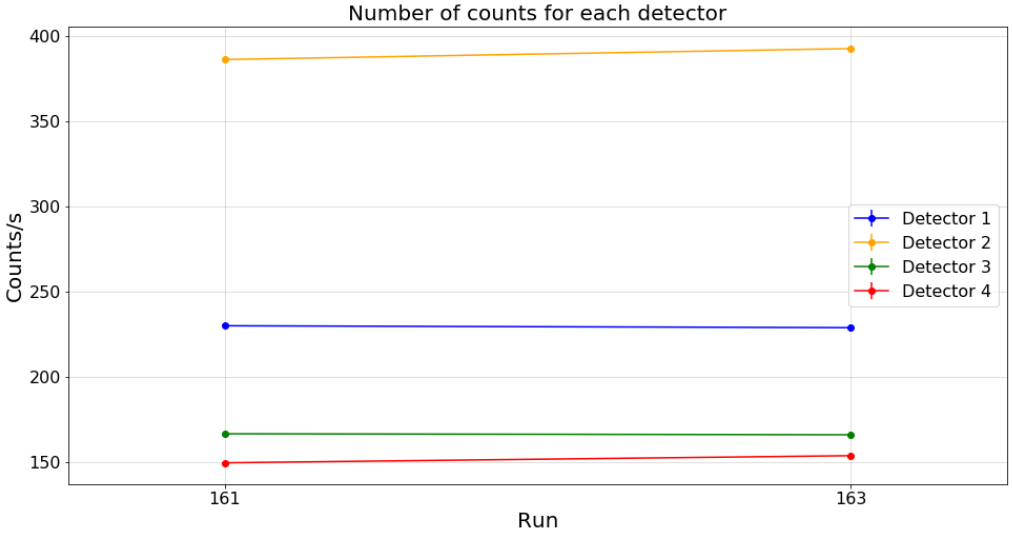

Figure 56: Average number of counts per second obtained with *one Gaussian total fit* for Runs 161 and 163. Detectors 1 and 2: transverse. Detectors 3 and 4: longitudinal.

but not in the way we would expect. We cannot see huge differences between the percentages differences between detectors 1 and 2 and detectors 3 and 4 which should remain stable and the others which should change more obviously.

Table 3: Percentage differences between runs 161 and 163 for each detectors using number of counts obtained with *10 second bin fits*. Detectors 1 and 2: transverse. Table 24, Equation 12.

Percentage differences between runs with *10 second bin fits*	
	161-163
Detector 1 (transverse)	0.2(3)
Detector 2 (transverse)	1.9(2)
Detector 3 (longitudinal)	0.6(3)
Detector 4 (longitudinal)	0.8(4)

Table 4: Percentage differences between runs 161 and 163 for each detectors using number of counts obtained with *One Gaussian total fit*. Detectors 1 and 2: transverse. Table 25, Equation 12.

Percentage differences between runs with *One Gaussian total fit*	
	161-163
Detector 1 (transverse)	-0.5(3)
Detector 2 (transverse)	1.6(2)
Detector 3 (longitudinal)	-0.4(3)
Detector 4 (longitudinal)	2.7(4)

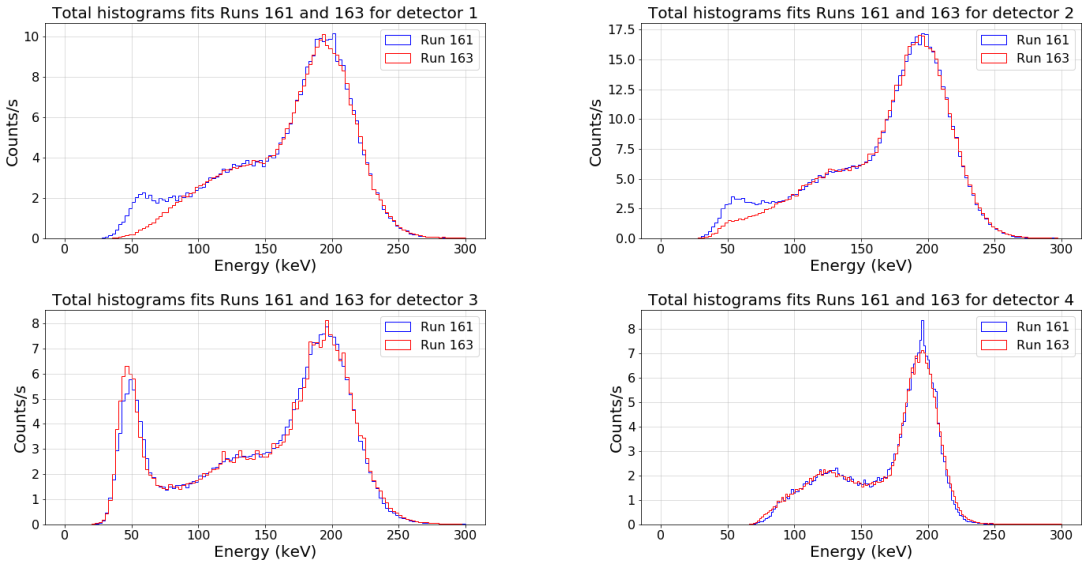

Figure 57: Superposition of all data histogram spectra for all detectors for runs 161 and 163, with energy calibration. Detectors 1 and 2: transverse. Detectors 3 and 4: longitudinal.

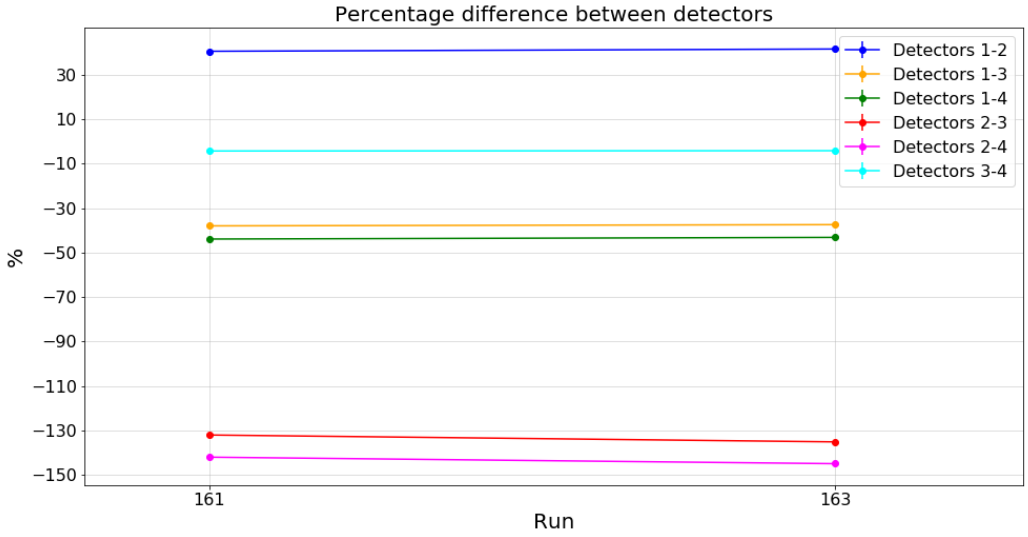

Figure 58: Percentage differences of counts per second between detectors obtained with *10 second bin fits* for Runs 161 and 163. Detectors 1 and 2: transverse. Detectors 3 and 4: longitudinal.

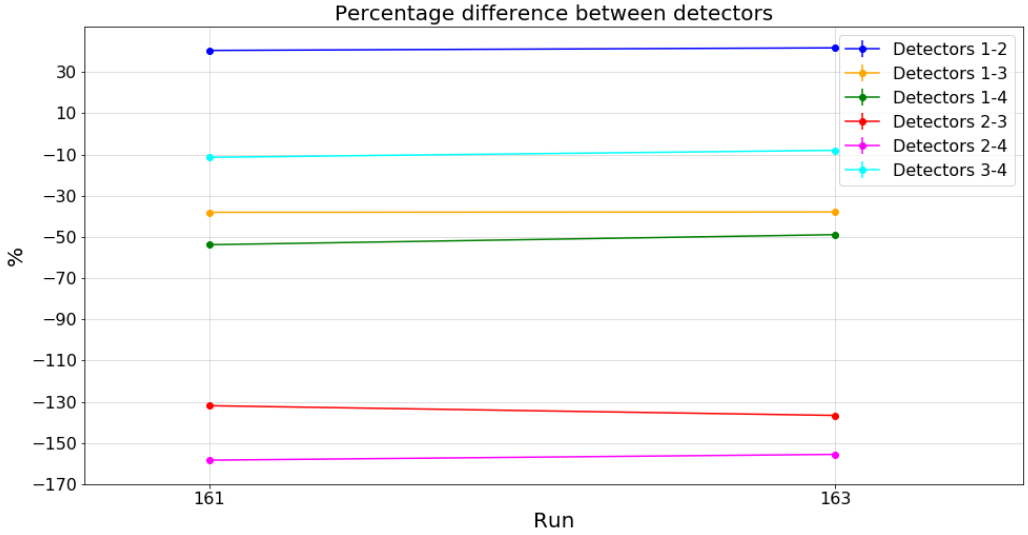

Figure 59: Percentage differences of counts per second between detectors obtained with *one Gaussian total fit* for Runs 161 and 163. Detectors 1 and 2: transverse. Detectors 3 and 4: longitudinal.

4.7.2.2 *Three Gaussians total fit* results

The average number of counts for *"three Gaussians total fit"* are shown in Figure . We made the calculations of percentages of differences between runs with these numbers, and the results

are shown in Table 26.

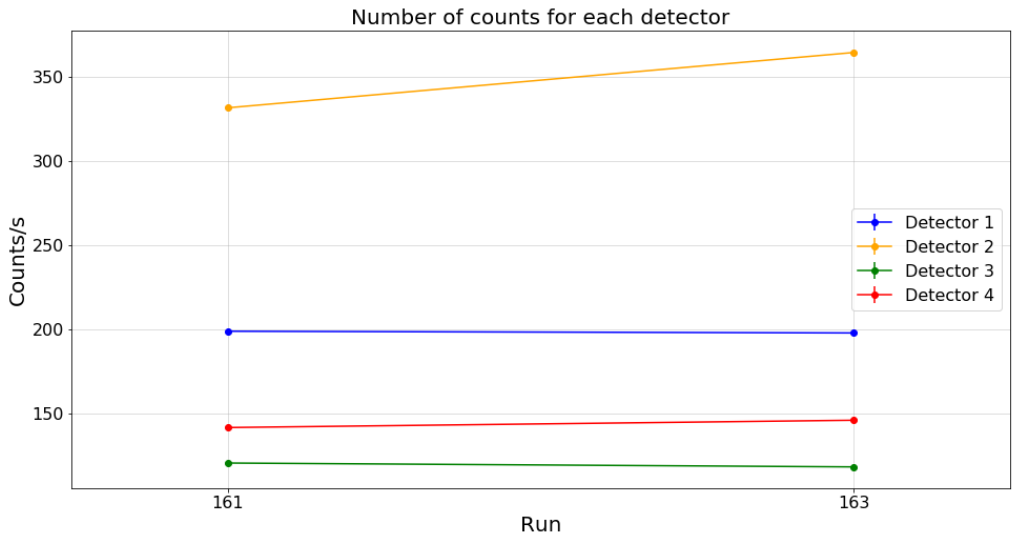

Figure 60: Average number of counts per second obtained with *three Gaussians total fit* for Runs 161 and 163. Detectors 1 and 2: transverse. Detectors 3 and 4: longitudinal.

Table 5: Percentage differences between runs 161 and 163 for each detectors using number of counts obtained with *three Gaussians total fit*. Detectors 1 and 2: transverse. Table 26, Equation 12.

Percentage differences between runs with *three Gaussians total fit*	
	161-163
Detector 1 (transverse)	-1.3(3)
Detector 2 (transverse)	-16.8(3)
Detector 3 (longitudinal)	-0.9(4)
Detector 4 (longitudinal)	3.1(4)

We can see a big difference between the two runs for detector 2, and more moderate differences for the others. These results are quite different from the previous ones, but are not closer to the expected results. Again we don't observe the changes expected for longitudinal and transverse detectors.

4.7.2.3 *drift correction fits* results

We can again try the *"drift correction fits"*. Figure 61 shows the number of counts obtained, and Table 31 shows the percentage differences between the two runs. The number of counts are also shown in Table 27 in Appendix D.

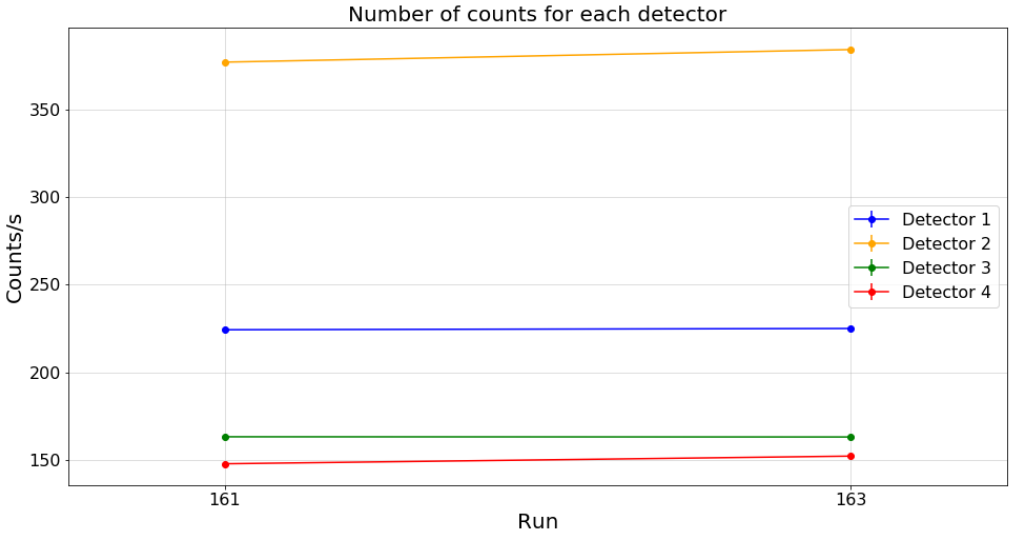

Figure 61: Average number of counts per second obtained with *drift correction fits* for Runs 161 and 163. Detectors 1 and 2: transverse. Detectors 3 and 4: longitudinal.

Table 6: Percentage differences between runs 161 and 163 for each detectors using number of counts obtained with *drift correction fits*. Detectors 1 and 2: transverse. Table 27, Equation 12.

Percentage differences between runs with *drift correction fits*	
	161-163
Detector 1 (transverse)	0.3(3)
Detector 2 (transverse)	1.9(2)
Detector 3 (longitudinal)	-0.1(3)
Detector 4 (longitudinal)	2.9(4)

Here we can see an increase between runs 161 and 163 for detectors 1 and 2 (transverse), and a decrease for detector 3 (longitudinal). Unfortunately, we can also see a clear increase for detector 4 (longitudinal), even larger than all the other changes. This therefore does not allow us to draw conclusions related to the results of runs 137 to 140.

We can again try to look at the percentage differences between the detectors in Figure 62. The corresponding numbers are shown in Table 35 in Appendix D.

The changes in the percentage differences between a longitudinal and a transverse detector are not very large and seem random, and the differences which should remain stable change in about the same order of magnitude. Again, this does not allow us to compare these numbers with the results of the runs studied previously.

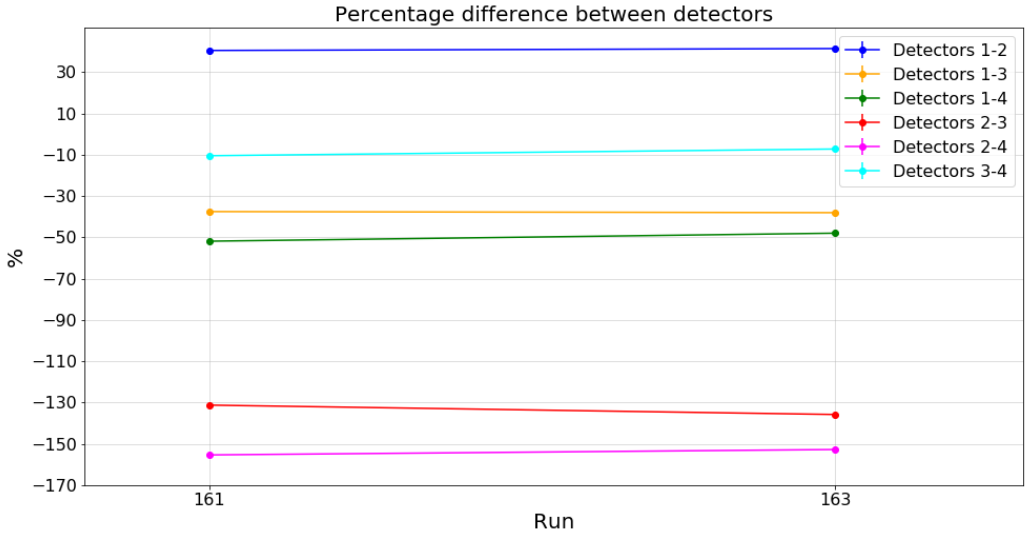

Figure 62: Percentage differences of counts per second between detectors obtained with *"drift correction fits"* for Runs 161 and 163. Detectors 1 and 2: transverse. Detectors 3 and 4: longitudinal.

4.8 Discussion of results

4.8.1 Runs with ^{129m}Xe

Table 7 shows a summary of the results of all different approaches for runs 137, 138, 139 and 140, using ^{129m}Xe. The percentage differences between runs 138 and 139 and between runs 139 and 140 for *10 second bin fits*, *one Gaussian total fit* and *drift correction fit* are similar and in good agreement. The differences related to Run 137 vary a lot between these methods. The explanation is that during runs 137 and 140, temperature changes were induced, as explained in Section 4.8.1 and summarized in Table 1. The temperature change during Run 137 was faster and more drastic since we were heated the sample than for Run 140 for which we let the temperature slowly decrease. That's why we focus more on the other two Runs: 138 and 139, which were taken at stable temperature. The only method that does not agree with the others is the one with *three Gaussians total fit*.

For these three methods which are *10 second bin fits*, *one Gaussian total fit* and *drift correction fit*, we can observe a slight increase for the transverse detectors 1 and 2 between runs 138 and 139, and a decrease for the longitudinal ones 3 and 4. These are the trends we would expect to see if the presence of magnetic field indeed lead to a build-up of polarization similar to those presented in the work of Virginia team [1]. If these results turn out to be true asymmetries of gamma radiation, it would mean that the hyperpolarization of the spins has been successfully accomplished and recorded.

The differences between *three Gaussians total fit* with the other methods can be explained. With the other approaches, we were using a simple Gaussian fit, so we ignored the influence of the other peaks on the third (rightmost) one. By fitting with three Gaussians, we take into account that some of the counts under the rightmost peak actually belong to the second peak

Table 7: Summary of percentage differences between runs 137, 138, 139 and 140 with the different methods for data analysis: *10 second bin fits*, *one Gaussian total fit*, *three Gaussians total fit*, *drift correction fit*.

Summary of results for runs 137, 138, 139 and 140			
	137-138	138-139	139-140
10 second bin fits			
Detector 1 (transverse)	0.2(1)	1.2(1)	-1.0(1)
Detector 2 (transverse)	-0.2(1)	0.8(1)	-0.4(1)
Detector 3 (longitudinal)	0.6(1)	-2.5(1)	2.0(1)
Detector 4 (longitudinal)	1.1(1)	-3.9(1)	2.2(1)
one Gaussian total fit			
Detector 1 (transverse)	-4.0(1)	0.7(1)	-1.3(1)
Detector 2 (transverse)	-6.2(1)	0.6(1)	-1.0(1)
Detector 3 (longitudinal)	-6.8(1)	-3.1(1)	1.9(1)
Detector 4 (longitudinal)	1.8(1)	-5.0(1)	0.5(1)
three Gaussians total fit			
Detector 1 (transverse)	-2.9(1)	-0.8(1)	-0.4(1)
Detector 2 (transverse)	-10.4(1)	3.6(1)	2.0(1)
Detector 3 (longitudinal)	-18.4(1)	-4.0(1)	1.3(1)
Detector 4 (longitudinal)	-1.0(1)	-5.5(1)	0.6(1)
drift correction fit			
	137-138	138-139	139-140
Detector 1 (transverse)	-0.0(1)	1.3(1)	-1.1(1)
Detector 2 (transverse)	-0.4(1)	1.2(1)	-0.9(1)
Detector 3 (longitudinal)	0.5(1)	-2.6(1)	2.1(1)
Detector 4 (longitudinal)	1.5(1)	-4.5(1)	1.5(1)

(the one in the middle). But it is difficult to determine the exact influence of other peaks on the one we are interested in. That's why using the same method but slightly different parameters, the results can change dramatically. It is also unlikely that all the peaks are actually Gaussians, and this approximation may not be very good, especially given the big differences in results with the other methods.

We also calculated the percentages of difference between the detectors within the same run, which we then compared between the runs. This approach allows to demonstrate the preceding results by comparing the differences in the number of counts between the detectors rather than the numbers of counts themselves. In the case of runs 138 and 139, for *10 second bin fits*, *one Gaussian total fit* and *drift correction fit*, this only confirms our previous observations showing that the differences between a longitudinal detector and a transverse detector increase during the activation of the magnetic field, while the differences between two longitudinal detectors or two transverse detectors remain stable.

For *three Gaussians total fit*, unsurprisingly, this method does not give better results. The percentages of differences seem a bit random and do not give concrete results.

Table 8: Summary of percentage differences between runs 161 and 163 with the different methods for data analysis: *10 second bin fits*, *one Gaussian total fit*, *three Gaussians total fit*, *drift correction fit*.

Summary of results for runs 161 and 163	
	161-163
10 second bin fits	
Detector 1 (transverse)	0.2(3)
Detector 2 (transverse)	1.9(2)
Detector 3 (longitudinal)	0.6(3)
Detector 4 (longitudinal)	0.8(4)
one Gaussian total fit	
Detector 1 (transverse)	-0.5(3)
Detector 2 (transverse)	1.6(2)
Detector 3 (longitudinal)	-0.4(3)
Detector 4 (longitudinal)	2.7(4)
three Gaussians total fit	
Detector 1 (transverse)	-1.3(3)
Detector 2 (transverse)	-16.8(3)
Detector 3 (longitudinal)	-0.9(4)
Detector 4 (longitudinal)	3.1(4)
drift correction fit	
Detector 1 (transverse)	0.3(3)
Detector 2 (transverse)	1.9(2)
Detector 3 (longitudinal)	-0.1(3)
Detector 4 (longitudinal)	2.9(4)

4.8.2 Runs with ^{131m}Xe

We did the same analysis for runs 161 and 163, which are similar to runs 138 and 139, but using ^{131m}Xe, and Table 8 shows a summary of the results. Unfortunately, none of the three methods used to fit the spectra showed such promising results, and they weren't particularly in good agreement with each other. We again calculated the percentages of difference between the detectors within the same run, and then we compared between the runs. But here almost all the percentages of differences for the three methods remained stable or randomly changed and did not provide additional information.

It is therefore difficult to estimate whether these runs show asymmetries or not. One thing may explain the difficulty of getting good results for these runs, which is that the number of counts recorded is much lower than for the previous runs. This comes from the fact that we measured for a shorter time, and that the detectors were further from the source.

4.8.3 General discussion

This thesis was devoted to the analysis and comparison of spectra recorded with and without the presence of the magnetic field for ^{129m,131m}Xe. We also tried to reproduce the results presented in the thesis [1] of the Virginia group. The difference in the number of counts is obvious on Figure 16, it is not on our Figures 43 and 57. If hyperpolarization is present in our measurements, it is not as visible and therefore probably weaker. More optimal conditions

could therefore perhaps be found to improve the achieved degree of hyperpolarization in ^{129m,131m}Xe.

All of these methods that we used to analyze the data have strengths and weaknesses.

Doing a Gaussian fit on the total spectrum is very simple because we have large statistics and very little manipulation to do, so we are less likely to generate errors. However, we do not take into account the influence of the other peaks on the one rightmost one, nor the energy drift induced by temperature variations.

Separating the data by time intervals, then performing a Gaussian fit for each interval minimizes the potential impact of temperature drift. Though, by doing a simple Gaussian fit, we still don't take into account the influence of the other peaks. Additionally, making multiple fits to spectra containing less data leads to inaccuracies in the results.

Making a three Gaussians fit on the total spectrum finally allows to take into consideration the influence of the other peaks on the third (if they are actually Gaussians). However, we do not know precisely the shape of these peaks, and therefore their effect on the data. It is thus difficult to obtain reliable results.

Performing a drift correction by separating the data by time intervals, calibrating all of the resulting histograms, and then adding them and integrating the total resulting spectra couls be the most powerful and the most reliable methods of all, because we have a great statistic we are less prone to errors, and we minimizes the potential impact of temperature drift. The only problem is that we don't take into account the influence of the other peaks on the rightmost one.

Most of the analysis approaches point to a small, but reproducible gamma asymmetry in presence of the magnetic field. Its direction agrees with the observations by the Virginia group, although its magnitude is smaller.

Following the tests carried out in this thesis, we can identify some points to enhance to improve the data analysis that we need to perform. A better knowledge of the spectrum we are studying would help separate the data we are interested in from the rest. Then, we must determine which is the most accurate and correct method for this experiment. For this, blind studies can be carried out (some have already been done) on well-known data similar to those obtained in this project.

For now, it might be too early to draw final conclusions based on the results presented in this thesis. However, the graphs and numbers presented point to a small, but clear gamma asymmetry due to spin hyperpolarization achieved on ^{129m}Xe. We hope that the analysis of other spectra, based on the procedures described in this thesis, will help to confirm the presence of and will quantify the degree of hyperpolarization.

4.8.4 Fit with a Compton Edge

This part concerns a possible way to fit the spectra with more precision, taking into account the part to the left of the rightmost peak, but this time by fitting it with a Compton Edge.

The part on the left with respect to the rightmost peak could be the Compton continuum, due to the Compton scattering in the scintillator, as explained in Section 2.3. This means that the peak on the left with respect to the rightmost one should be a Compton Edge. With this assumption, if we want to fit the spectrum, we have to use a function combining a Compton continuum and Compton edge part with a Gaussian part for the rightmost peak.

For the Compton part, we use the following formula [14]:

$$R(E) = \alpha_1 \cdot erfc\left[\frac{E - E_c}{\sqrt{(2)}\sigma}\right] + \beta_1 \cdot \exp\left[\frac{-(E - E_c)^2}{2\sigma^2}\right] \tag{14}$$

With:

$$\text{erfc}(E) = 1 - \frac{2}{\sqrt{\pi}} \int_0^E \exp -x^2 dx$$

And with:

$$\alpha_1(E) = \frac{1}{2}\left[a(E^2 + \sigma^2) + bE + c\right]$$

$$\beta_1(E) = \frac{-\sigma}{\sqrt{2\pi}} a(E + E_c) + b$$

Here E is the energy, E_c is the energy value for which the maximum occurs, a, b, and c are parameters and σ is the variance.

For the Gaussian part, we use the usual formula of Equation 11

So the complete formula is simply the addition of these two formulas. Figure 63a shows the curves resulting from Equations 14 and 11, and Figure 63b shows the curve resulting from the addition of these two.

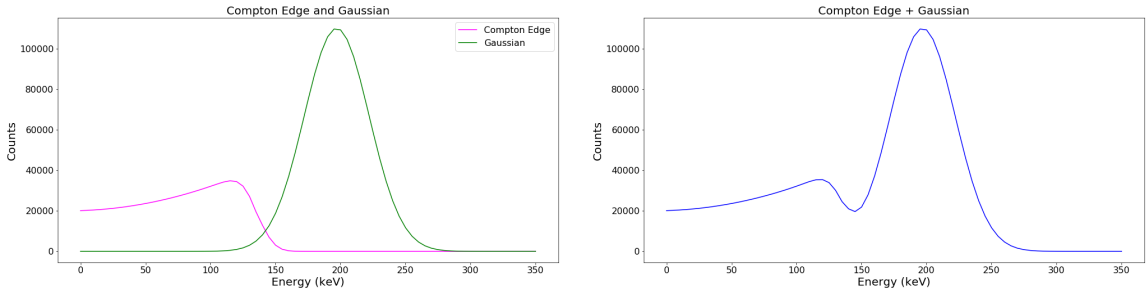

(a) Compton and Gaussian. (b) Compton + Gaussian.

Figure 63: Compton edge and Gaussian curves.

With the right parameters, this could correctly match our spectra, and thus make the data analysis more accurate. This possibility will be studied in the near future.

5 Conclusion and Outlook

5.1 Conclusion

From June to September 2019, the gamma-MRI experiment covered in this thesis was executed. The objective of the experimental period was to successfully hyperpolarize two Xenon isomers which are ^{129m}Xe and ^{131m}Xe by Spin-Exchange Optical-Pumping. The procedure consists of the polarization of the Alkali metal, Rubidium, with a laser (Optical-Pumping), and the hyperpolarization of the isomers via the spin-exchange between the polarised atom and the Xe nucleus (hyperfine interaction), and then recording the asymmetries in the gamma emissions when spin polarisation could be achieved (magnetic field on), compared to absence of polarisation (magnetic field off). To perform this experiment, an adapted setup was installed, and regularly improved to make it more functional for the experiment.

This thesis was devoted to the analysis of the data collected during the experimental period to to look for possible asymmetries in the gamma emissions using the data collected by the four detectors placed transversely or longitudinally. The analysis of data taken under different experimental conditions also allowed to determine whether spin polarization was achieved to identify the best parameters for the next measurement periods.

The most promising results come from the analysis of a series of runs with ^{129m}Xe, two of which were taken in succession under identical conditions, except that in one case the magnetic field was on, and in the other it was off. These are runs 137, 138, 139 and 140. The most interesting results occurred between runs 138 during which the magnetic field was off, and 139 during which it was on. During run 139, we therefore expected a decrease in counts for the longitudinal detectors, and an increase for the transverse detectors. This is what we can observe with three of our fitting methods of the four selected, although the differences are less obvious than what was expected.

The first approach, called *"10 second bin fits"*, was simply to make the fit of a single Gaussian on the peak of our interest. This is a simple and quick method to implement and adapt to all kinds of spectra. However, it can potentially lack precision in our case, since it does not take into account the energy shift induced by changes in temperature, nor the influence of the rest of the spectrum on the peak studied. With this method, in presence of the magnetic field (i.e. conditions suitable for spin polarisation), we have effectively observed a slight increase in counts for the transverse detectors 1 and 2, and decreases for the longitudinal ones 3 and 4, which might indicate that hyperpolarization of ^{129m}Xe was successfully achieved.

The second approach we named *"One Gaussian total fit"* was to separate the data in 10 second intervals, and independently fit each data bunch. Finally, the results were summed together to obtain the total number of counts. This method takes into consideration the energy shift caused by temperature changes, but not the influence of other peaks. This method, showing results not identical but similar to those of the first one, confirmed the first observations.

Unfortunately, the third technique, *"Three Gaussians total fit"*, presented in this thesis did not show such encouraging results. It was about fitting the entire spectrum with three Gaussians and integrating under the last one. This technique allowed to take into account the influence of the rest of the spectrum on the last peak (if they are Gaussians). However, it was not possible to implement time-based data separation with this method, so the temperature drift was not compensated. We actually observed a decrease for the longitudinal detectors between runs 138 and 139, and an increase for detector 2 which is transverse, but we conversely observe a slight decrease of for detector 1 which is also transverse, which is not in line with our expectations and previous results.

The fourth and last technique, called *"Drift correction fit"* and inspired by the best aspects

of our two first methods, was to separate the data in ten second intervals as for the first one, but instead of integrating them directly, we first added them and then integrated the resulting histogram. This technique is probably the most reliable one. It takes into consideration the energy shift caused by temperature changes, but not the influence of other peaks.
As for the first two methods, we observed slight increases for the transverse detectors 1 and 2, and decreases for the longitudinal ones 3 and 4, which confirmed the first observations we made.

To highlight the differences in counts we saw between the runs, we calculated the percentage differences in counts (asymmetries) registered in different detectors within the same run, and then we compared the results between the different runs. The latter approach allowed us to highlight the encouraging results that we saw in individual detectors, and to confirm that the method with three Gaussians gave results different from the other 3 approaches, and was therefore possibly a bad approximation.

We also analysed two runs 161 and 163, recorded in similar conditions to runs 138 and 139, but using ^{131m}Xe. We carried out the same analyzes, but unfortunately we did not obtain similar results. The percentages differences in detector counts between file 161 and 163, and asymmetries in counts in different detectors in both files are not affected by the presence of the magnetic field for none of the four approaches. This might be due to the lower activity in the vial, a little different pressure of the gases inside the vial, or a different distance of the detectors from the vial.

To summarise, this thesis explored several approaches to analyse ^{129m}Xe and ^{131m}Xe spectra in the gamma-MRI project. The aim was to obtain reliable changes in counts when the experimental parameters were changed, and reliable asymmetries in counts between detectors placed longitudinally and transversely to the magnetic field. Systematic fits to ^{129m}Xe spectra during which the detector gain was changing, allowed to show that the fitting strategy for one Gauss fit gives the same results within about 1% or better. For ^{129m}Xe, the systematic analysis of one set of 4 files, allowed to show a change in counts in the detectors and in asymmetry between the detectors at the level of $1-4\%$. The direction of the changes is consistent with presence of spin-orientation when the magnetic field is on. The magnitude is smaller than hoped for.

For ^{131m}Xe, as set of two files, recorded in similar conditions and analysed in the same way as ^{129m}Xe, showed no spin-orientation larger than the uncertainties.

5.2 Outlook for gamma-MRI project

The data analysed within this thesis presented several challenges, which were identified during the measurements or only during the present analysis. Therefore, in this thesis, several fitting and analysis strategies have been studied, it remains now to perfect them, and to identify the best way to use the promising data to progress in the gamma-MRI project. Points to consider when studying the data have been highlighted. More specifically, we have seen that each method presented in this thesis has its strengths and weaknesses. A better knowledge of the studied spectrum would be also advantageous, in order to be able to better constrain the parameters during the fit procedure.

The measurements of this experimental session allow to identify the points to improve, and those which gave the best results for asymmetries. Based on the gamma-decay asymmetry observed in different sets of files (including the ones analysed in this thesis), technical improvements will be in order to get the best conditions to achieve hyperpolarization of metastable Xenon isomers via SEOP. For this purpose, the results of the analysis will be compared to ongoing simulations and to the results of the Virginia group presented in the Nature paper [2] and thesis [1]. This should allow to work on the optimisation of hyperpolarisation.

The recently obtained funding for gamma-MRI, within the EU scheme for Future and Emerging Technologies (FET-OPEN) should provide enough resources to progress in analysing more data, simulating the expected signals, predicting optimal conditions, building an optimised experimental setup, and takings steps to change gamma-MRI from an experimental technique into a technology.

A Fits setting tables

Table 9: Number of counts for several time bins for each detector for Run 137.

Counts for several time bins				
	Detector 1	Detector 2	Detector 3	Detector 4
10 seconds	1277021	1186956	1421046	1310003
30 seconds	1257766	1168992	1399843	1290233
50 seconds	1277021	1186956	1421046	1310003

Table 10: Number of counts for several bin widths for each detector for Run 137.

Counts for several bin widths				
	Detector 1	Detector 2	Detector 3	Detector 4
5 keV	1396206	1320916	1576829	1332544
2.5 keV	1305886	1237084	1497268	1302898
1.5 keV	1309044	1233368	1504061	1256584
1 keV	1324343	1231594	1536904	1241213

Table 11: Number of counts for several starting fit energies for each detector for Run 137.

Counts for several starting fit energies				
	Detector 1	Detector 2	Detector 3	Detector 4
150 keV	1384561	1302394	1548988	1328784
160 keV	1345517	1265934	1513318	1324152
170 keV	1314549	1241463	1496577	1297413
180 keV	1301057	1232609	1516061	1257816
190 keV	1302185	1240725	1517525	1210330

B Background Measurements

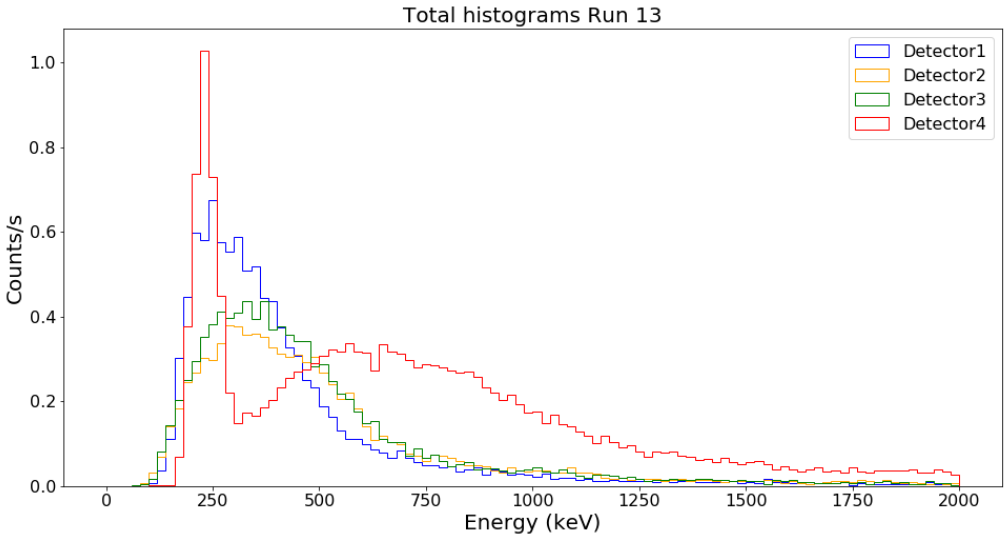

Figure 64: Background Measurements: all data histogram spectra for all detectors for run Run 13.

Figure 64 shows a spectrum of the numbers of counts per second for a background measurement. For the all spectrum, the number of counts do not exceed 1, while for the runs used in this thesis, the measurements are always at least 150 counts per second. It was therefore decided that the background noise could be neglected for the calculations.

C Error calculations

In this thesis, uncertainties on number of counts detected and percentages differences were calculated. We decided to take into account only the statistical errors, which is a sufficient approximation for the analysis we are doing here.

The statistical error on a number (used in the calculations which follow) is only given by the square root of this number.

C.1 Calculations for $f = \frac{a}{b}$

$$\sigma^2 = \left(\left(\frac{1}{b}\right) \cdot \sigma a\right)^2 + \left(\left(-\frac{a}{b^2}\right) \cdot \sigma b\right)^2$$

$$\Rightarrow \sigma^2 = \frac{1}{b^2}\sigma a^2 + \frac{a^2}{b^4}\sigma b^2$$

with $\sigma a = \sqrt{a}$ and $\sigma b = \sqrt{b}$.

$$\Rightarrow \sigma^2 = \frac{a}{b^2} + \frac{a^2}{b^3}$$

And the approximation $a \approx b$ can be made.

$$\Rightarrow \sigma = \sqrt{\frac{2}{a}}$$

C.2 Calculations for $f = \frac{a-b}{a}$

$$\sigma^2 = \left(ba^{-2} \cdot \sigma a\right)^2 + \left(-a^{-1} \cdot \sigma b\right)^2$$

- if $\sigma a = \sqrt{a}$ and $\sigma b = \sqrt{b}$, then:

$$\sigma^2 = b^2 a^{-3} + a^{-2} b$$

And with the approximation $a \approx b$:

$$\Rightarrow \sigma = \sqrt{\frac{2}{a}}$$

- if $\sigma a \neq \sqrt{a}$ and $\sigma b \neq \sqrt{b}$, and using the approximation $a \approx b$, then:

$$\sigma = \frac{\sqrt{2}}{a}\sigma a$$

D Additional tables

D.1 Runs 137, 138, 139 and 140

Table 12: Number of counts per second for each detector for run 137, 138, 139 and 140 obtained with *10 second bin fits*.

Counts/s with *10 second bin fits*				
	Run 137	Run 138	Run 139	Run 140
Detector 1 (transverse)	916.6(8)	918.0(9)	929.1(8)	919.7(9)
Detector 2 (transverse)	851.0(8)	849.1(8)	856.1(8)	852.3(8)
Detector 3 (longitudinal)	1019.6(9)	1025.4(9)	1000.0(9)	1020.8(9)
Detector 4 (longitudinal)	942.4(8)	953.3(9)	917.4(8)	938.0(9)

Table 13: Number of counts per second for each detector for run 137, 138, 139 and 140 obtained with *One Gaussian total fit*.

Counts/s with *One Gaussian total fit*				
	Run 137	Run 138	Run 139	Run 140
Detector 1 (transverse)	972.9(9)	935.6(9)	941.8(9)	929.9(9)
Detector 2 (transverse)	922.2(8)	868.4(8)	873.6(8)	864.7(8)
Detector 3 (longitudinal)	1118.6(9)	1047.2(9)	1015.6(9)	1035.7(9)
Detector 4 (longitudinal)	937.5(8)	954.8(9)	909.0(8)	913.5(9)

Table 14: Number of counts per second for each detector for run 137, 138, 139 and 140 obtained with *Three Gaussians total fit*.

Counts/s with *Three Gaussians total fit*				
	Run 137	Run 138	Run 139	Run 140
Detector 1 (transverse)	907.7(8)	881.9(8)	874.8(8)	874.8(8)
Detector 2 (transverse)	820.5(8)	743.4(8)	771.6(8)	771.6(8)
Detector 3 (longitudinal)	1038.0(9)	876.9(8)	843.5(8)	843.5(8)
Detector 4 (longitudinal)	828.1(8)	820.3(8)	777.4(8)	777.4(8)

Table 15: Number of counts per second for each detector for run 137, 138, 139 and 140 obtained with *drift correction fit*.

Counts/s with *drift correction fit*				
	Run 137	Run 138	Run 139	Run 140
Detector 1 (transverse)	921.9(8)	921.8(9)	933.9(8)	923.7(9)
Detector 2 (transverse)	857.9(8)	854.6(8)	865.2(8)	857.7(8)
Detector 3 (longitudinal)	1028.7(9)	1033.8(9)	1007.2(9)	1028.5(9)
Detector 4 (longitudinal)	925.5(8)	939.7(9)	899.4(8)	913.4(9)

Table 16: Percentage differences between runs 137, 138, 139 and 140 for each detector using number of counts obtained with *10 second bin fits*. Table 12, Equation 12.

Percentage differences between runs with *10 second bin fits*			
	137-138	138-139	139-140
Detector 1 (transverse)	0.2(1)	1.2(1)	-1.0(1)
Detector 2 (transverse)	-0.2(1)	0.8(1)	-0.4(1)
Detector 3 (longitudinal)	0.6(1)	-2.5(1)	2.0(1)
Detector 4 (longitudinal)	1.1(1)	-3.9(1)	2.2(1)

Table 17: Percentage differences between runs 137, 138, 139 and 140 for each detector using number of counts obtained with *One Gaussian total fit*. Table 13, Equation 12.

Percentage differences between runs with *One Gaussian total fit*			
	137-138	138-139	139-140
Detector 1 (transverse)	-4.0(1)	0.7(1)	-1.3(1)
Detector 2 (transverse)	-6.2(1)	0.6(1)	-1.0(1)
Detector 3 (longitudinal)	-6.8(1)	-3.1(1)	1.9(1)
Detector 4 (longitudinal)	1.8(1)	-5.0(1)	0.5(1)

Table 18: Percentage differences between runs 137, 138, 139 and 140 for each detector using number of counts obtained with *Three Gaussians total fit*. Table 14, Equation 12.

Percentage differences between runs with *Three Gaussians total fit*			
	137-138	138-139	139-140
Detector 1 (transverse)	-2.9(1)	-0.8(1)	-0.4(1)
Detector 2 (transverse)	-10.4(1)	3.6(1)	2.0(1)
Detector 3 (longitudinal)	-18.4(1)	-4.0(1)	1.3(1)
Detector 4 (longitudinal)	-1.0(1)	-5.5(1)	0.6(1)

Table 19: Percentage differences between runs 137, 138, 139 and 140 for each detector using number of counts obtained with *drift correction fit*. Table 15, Equation 12.

Percentage differences between runs with *drift correction fit*			
	137-138	138-139	139-140
Detector 1 (transverse)	-0.0(1)	1.3(1)	-1.1(1)
Detector 2 (transverse)	-0.4(1)	1.2(1)	-0.9(1)
Detector 3 (longitudinal)	0.5(1)	-2.6(1)	2.1(1)
Detector 4 (longitudinal)	1.5(1)	-4.5(1)	1.5(1)

Table 20: Percentage differences between detectors for runs 137, 138, 139 and 140 using number of counts obtained with *10 second bin fits*. Table 12, Equation 13.

Percentage differences between detectors with *10 second bin fits*				
	137	138	139	140
Detectors 1-2 (trans./trans.)	-7.7(1)	-8.1(1)	-8.5(1)	-7.9(1)
Detectors 1-3 (trans./long.)	10.1(1)	10.5(1)	7.1(1)	9.9(1)
Detectors 1-4 (trans./long.)	2.7(1)	3.7(1)	-1.3(1)	2.0(1)
Detectors 2-3 (trans./long.)	16.5(1)	17.2(1)	14.4(1)	16.5(1)
Detectors 2-4 (trans./long.)	9.7(1)	10.9(1)	6.7(1)	9.1(1)
Detectors 3-4 (long./long.)	-8.2(1)	-7.6(1)	-9.0(1)	-8.8(1)

Table 21: Percentage differences between detectors for runs 137, 138, 139 and 140 using number of counts obtained with *One Gaussian total fit*. Table 13, Equation 13.

Percentage differences between detectors with *One Gaussian total fit*				
	137	138	139	140
Detectors 1-2 (trans./trans.)	-5.5(1)	-7.7(1)	-7.8(1)	-7.5(1)
Detectors 1-3 (trans./long.)	13.0(1)	10.7(1)	7.3(1)	10.2(1)
Detectors 1-4 (trans./long.)	-3.8(1)	2.0(1)	-3.6(1)	-1.8(1)
Detectors 2-3 (trans./long.)	17.6(1)	17.1(1)	14.0(1)	16.5(1)
Detectors 2-4 (trans./long.)	1.6(1)	9.1(1)	3.9(1)	5.3(1)
Detectors 3-4 (long./long.)	-19.3(1)	-9.7(1)	-11.7(1)	-13.4(1)

Table 22: Percentage differences between detectors for runs 137, 138, 139 and 140 using number of counts obtained with *Three Gaussians total fit*. Table 14, Equation 13.

Percentage differences between detectors with *Three Gaussians total fit*				
	137	138	139	140
Detectors 1-2 (trans./trans.)	9.6(1)	15.7(1)	11.8(1)	9.7(1)
Detectors 1-3 (trans./long.)	-14.4(1)	0.6(1)	3.6(1)	1.9(1)
Detectors 1-4 (trans./long.)	8.8(1)	7.0(1)	11.1(1)	10.3(1)
Detectors 2-3 (trans./long.)	-26.5(1)	-18.0(1)	-9.3(1)	-8.5(1)
Detectors 2-4 (trans./long.)	-0.9(1)	-10.3(1)	-0.8(1)	0.7(1)
Detectors 3-4 (long./long.)	20.2(1)	6.5(1)	7.8(1)	8.5(1)

Table 23: Percentage differences between detectors for runs 137, 138, 139 and 140 using number of counts obtained with *drift correction fit*. Table 15, Equation 13.

Percentage differences between detectors with *drift correction fit*				
	137	138	139	140
Detectors 1-2 (trans./trans.)	-7.5(1)	-7.9(1)	-7.9(1)	-7.7(1)
Detectors 1-3 (trans./long.)	10.4(1)	10.8(1)	7.3(1)	10.2(1)
Detectors 1-4 (trans./long.)	0.4(1)	1.9(1)	-3.8(1)	-1.1(1)
Detectors 2-3 (trans./long.)	16.6(1)	17.3(1)	14.1(1)	16.6(1)
Detectors 2-4 (trans./long.)	7.3(1)	9.1(1)	3.8(1)	6.1(1)
Detectors 3-4 (long./long.)	-11.2(1)	-10.0(1)	-12.0(1)	-12.6(1)

D.2 Runs 161 and 163

Table 24: Number of counts per second for each detector for run 161 and 163 obtained with *10 second bin fits*.

Counts/s with *10 second bin fits*		
	Run 161	Run 163
Detector 1 (transverse)	221.5(5)	222.1(5)
Detector 2 (transverse)	372.5(6)	379.9(6)
Detector 3 (longitudinal)	160.6(4)	161.6(4)
Detector 4 (longitudinal)	154.0(4)	155.1(4)

Table 25: Number of counts per second for each detector for run 161 and 163 obtained with *One Gaussian total fit*.

Counts/s with *One Gaussian total fit*		
	Run 161	Run 163
Detector 1 (transverse)	229.9(5)	228.8(5)
Detector 2 (transverse)	386.2(6)	392.6(6)
Detector 3 (longitudinal)	166.5(4)	165.9(4)
Detector 4 (longitudinal)	149.5(4)	153.6(4)

Table 26: Number of counts per second for each detector for run 161 and 163 obtained with *Three Gaussians total fit*.

Counts/s with *Three Gaussians total fit*		
	Run 161	Run 163
Detector 1 (transverse)	199.4(5)	196.9(4)
Detector 2 (transverse)	330.9(6)	283.3(5)
Detector 3 (longitudinal)	120.4(4)	119.3(3)
Detector 4 (longitudinal)	141.8(4)	146.3(4)

Table 27: Number of counts per second for each detector for run 161 and 163 obtained with *drift correction fit*.

Counts/s with *drift correction fit*		
	Run 161	Run 163
Detector 1 (transverse)	224.3(5)	225.0(5)
Detector 2 (transverse)	377.2(6)	384.4(6)
Detector 3 (longitudinal)	163.1(4)	163.0(4)
Detector 4 (longitudinal)	147.7(4)	152.1(4)

Table 28: Percentage differences between runs 161 and 163 for each detector using number of counts obtained with *10 second bin fits*. Table 24, Equation 12.

Percentage differences between runs with *10 second bin fits*	
	161-163
Detector 1 (transverse)	0.2(3)
Detector 2 (transverse)	1.9(2)
Detector 3 (longitudinal)	0.6(3)
Detector 4 (longitudinal)	0.8(4)

Table 29: Percentage differences between runs 161 and 163 for each detector using number of counts obtained with *One Gaussian total fit*. Table 25, Equation 12.

Percentage differences between runs with *One Gaussian total fit*	
	161-163
Detector 1 (transverse)	-0.5(3)
Detector 2 (transverse)	1.6(2)
Detector 3 (longitudinal)	-0.4(3)
Detector 4 (longitudinal)	2.7(4)

Table 30: Percentage differences between runs 161 and 163 for each detector using number of counts obtained with *Three Gaussians total fit*. Table 26, Equation 12.

Percentage differences between runs with *Three Gaussians total fit*	
	161-163
Detector 1 (transverse)	-1.3(3)
Detector 2 (transverse)	-16.8(3)
Detector 3 (longitudinal)	-0.9(4)
Detector 4 (longitudinal)	3.1(4)

Table 31: Percentage differences between runs 161 and 163 for each detector using number of counts obtained with *drift correction fit*. Table 27, Equation 12.

Percentage differences between runs with *drift correction fit*	
	161-163
Detector 1 (transverse)	0.3(3)
Detector 2 (transverse)	1.9(2)
Detector 3 (longitudinal)	-0.1(3)
Detector 4 (longitudinal)	2.9(4)

Table 32: Percentage differences between detectors for runs 161 and 163 using number of counts obtained with *10 second bin fits*. Table 24, Equation 13.

Percentage differences between detectors with *10 second bin fits*		
	161	163
Detectors 1-2 (trans./trans.)	40.5(2)	41.5(2)
Detectors 1-3 (trans./long.)	-38.0(4)	-37.4(3)
Detectors 1-4 (trans./long.)	-43.9(4)	-43.1(4)
Detectors 2-3 (trans./long.)	-132.0(4)	-135.1(3)
Detectors 2-4 (trans./long.)	-141.9(4)	-144.9(4)
Detectors 3-4 (long./long.)	-4.3(4)	-4.2(4)

Table 33: Percentage differences between detectors for runs 161 and 163 using number of counts obtained with *One Gaussian total fit*. Table 25, Equation 13.

Percentage differences between detectors with *One Gaussian total fit*		
	161	163
Detectors 1-2 (trans./trans.)	40.5(2)	41.7(2)
Detectors 1-3 (trans./long.)	-38.1(4)	-37.9(3)
Detectors 1-4 (trans./long.)	-53.8(4)	-48.9(4)
Detectors 2-3 (trans./long.)	-131.9(4)	-136.6(3)
Detectors 2-4 (trans./long.)	-158.3(4)	-155.5(4)
Detectors 3-4 (long./long.)	-11.4(4)	-8.0(4)

Table 34: Percentage differences between detectors for runs 161 and 163 using number of counts obtained with *Three Gaussians total fit*. Table 26, Equation 13.

Percentage differences between detectors with *Three Gaussians total fit*		
	161	163
Detectors 1-2 (trans./trans.)	-65.9(1)	-43.9(1)
Detectors 1-3 (trans./long.)	39.6(1)	39.4(1)
Detectors 1-4 (trans./long.)	28.9(1)	25.7(1)
Detectors 2-3 (trans./long.)	63.6(1)	57.9(1)
Detectors 2-4 (trans./long.)	57.1(1)	48.4(1)
Detectors 3-4 (long./long.)	-17.8(2)	-22.6(2)

Table 35: Percentage differences between detectors for runs 161 and 163 using number of counts obtained with *drift correction fit*. Table 27, Equation 13.

Percentage differences between detectors with *drift correction fit*		
	161	163
Detectors 1-2 (trans./trans.)	40.5(2)	41.5(2)
Detectors 1-3 (trans./long.)	-37.5(4)	-38.0(3)
Detectors 1-4 (trans./long.)	-51.8(4)	-47.9(4)
Detectors 2-3 (trans./long.)	-131.2(4)	-135.7(3)
Detectors 2-4 (trans./long.)	-155.3(4)	-152.7(4)
Detectors 3-4 (long./long.)	-10.4(4)	-7.2(4)

E *Counting bins* method

This method, which will be called *"counting bins"*, consists in counting the counts which are above the calibration energy directly in the files (after energy calibration), which are the counts included in the bins after the middle of the peak, and multiply the result by two.

This energy is around 197keV for ^{129m}Xe, and around 164keV for ^{131m}Xe.

This method allow us to obtain an approximation of the number of counts without using a fit, and without being bothered by the contribution of the peaks on the left.

E.1 Runs 137, 138, 139 and 140

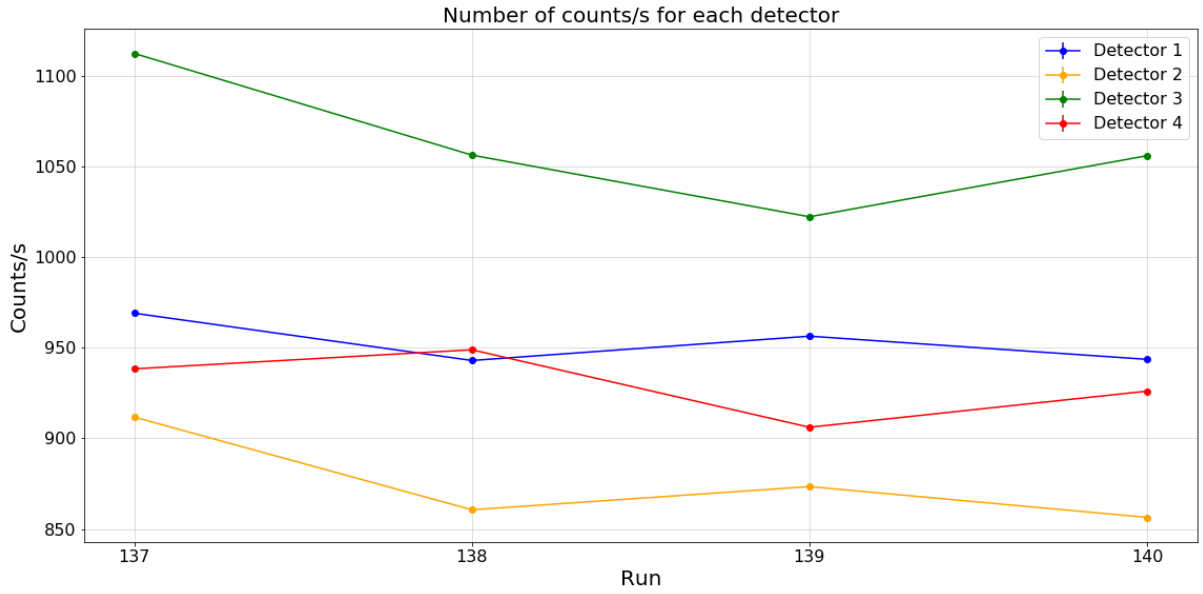

Figure 65: Average number of counts per second obtained with *counting bins* for Runs 137, 138, 139 and 140. Detectors 1 and 2: transverse. Detectors 3 and 4: longitudinal.

Table 36: Number of counts per second for each detector for run 137, 138, 139 and 140 obtained with *counting bins*.

Counts/s with *counting bins*				
	Run 137	Run 138	Run 139	Run 140
Detector 1 (transverse)	969.1(9)	943.0(9)	956.4(9)	956.4(9)
Detector 2 (transverse)	911.7(8)	860.6(8)	873.4(8)	873.4(8)
Detector 3 (longitudinal)	1112.4(9)	1056.3(9)	1022.3(9)	1022.3(9)
Detector 4 (longitudinal)	938.4(8)	948.9(9)	906.2(8)	906.2(9)

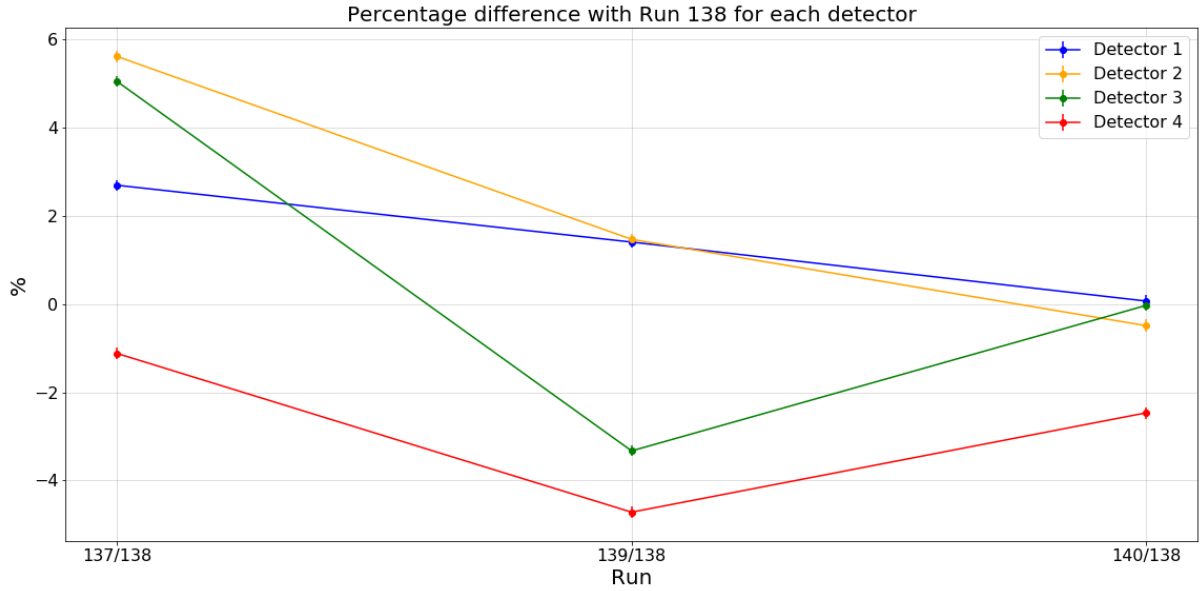

Figure 66: Percentage differences of counts per second obtained with *counting bins* for Runs 137, 138, 139 and 140. Detectors 1 and 2: transverse. Detectors 3 and 4: longitudinal.

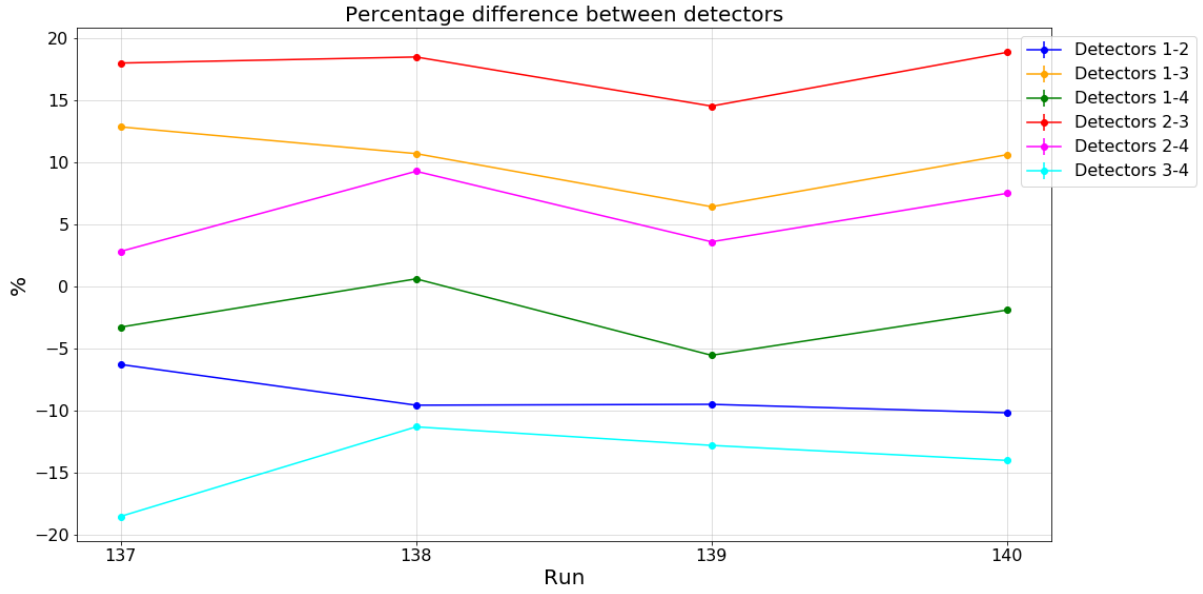

Figure 67: Percentage differences of counts per second between detectors obtained with *counting bins* for Runs 137, 138, 139 and 140. Detectors 1 and 2: transverse. Detectors 3 and 4: longitudinal.

Table 37: Percentage differences between runs 137, 138, 139 and 140 for each detector using number of counts obtained with *counting bins*. Table 36, Equation 12.

Percentage differences between runs with *counting bins*			
	137-138	138-139	139-140
Detector 1 (transverse)	-2.8(1)	1.4(1)	-1.4(1)
Detector 2 (transverse)	-5.9(1)	1.5(1)	-2.0(1)
Detector 3 (longitudinal)	-5.3(1)	-3.3(1)	3.2(1)
Detector 4 (longitudinal)	1.1(1)	-4.7(1)	2.1(1)

Table 38: Percentage differences between detectors for runs 137, 138, 139 and 140 using number of counts obtained with *counting bins*. Table 36, Equation 13.

Percentage differences between detectors with *counting bins*				
	137	138	139	140
Detectors 1-2 (trans./trans.)	-6.3(1)	-9.6(1)	-9.5(1)	-10.2(1)
Detectors 1-3 (trans./long.)	12.9(1)	10.7(1)	6.4(1)	10.6(1)
Detectors 1-4 (trans./long.)	-3.3(1)	0.6(1)	-5.5(1)	-1.9(1)
Detectors 2-3 (trans./long.)	18.0(1)	18.5(1)	14.6(1)	18.9(1)
Detectors 2-4 (trans./long.)	2.8(1)	9.3(1)	3.6(1)	7.5(1)
Detectors 3-4 (long./long.)	-18.5(1)	-11.3(1)	-12.8(1)	-14.0(1)

E.2 Runs 161 and 163

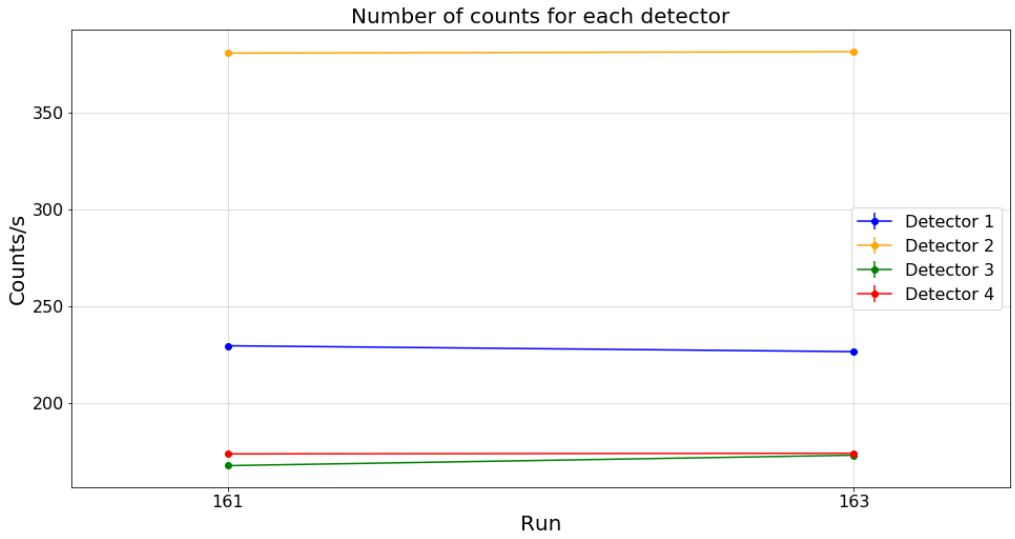

Figure 68: Average number of counts per second obtained with *counting bins* for Runs 161 and 163. Detectors 1 and 2: transverse. Detectors 3 and 4: longitudinal.

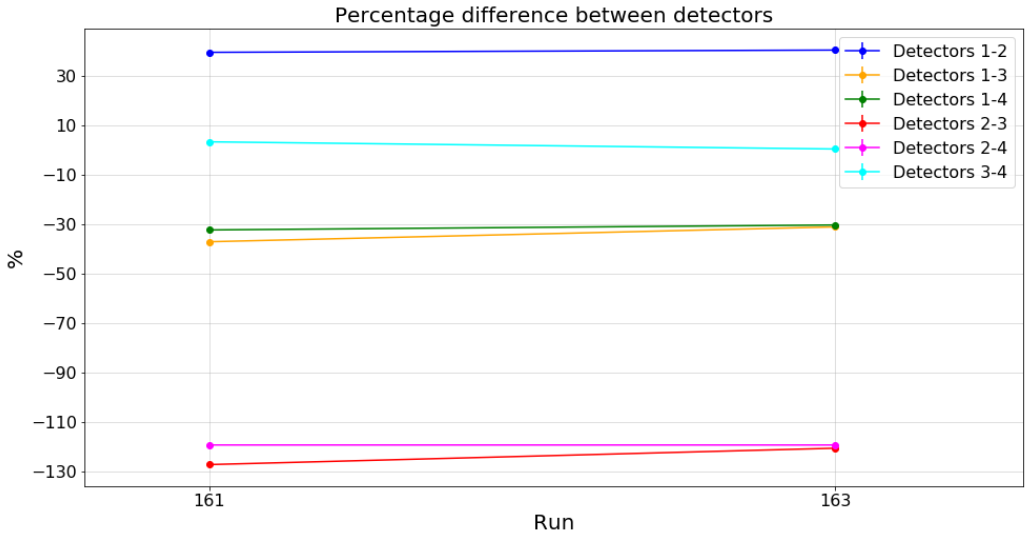

Figure 69: Percentage differences of counts per second between detectors obtained with *counting bins* for Runs 161 and 163. Detectors 1 and 2: transverse. Detectors 3 and 4: longitudinal.

Table 39: Number of counts per second for each detector for run 161 and 163 obtained with *counting bins*.

Counts/s with *counting bins*		
	Run 161	Run 163
Detector 1 (transverse)	229.5(5)	226.4(5)
Detector 2 (transverse)	380.6(6)	381.3(6)
Detector 3 (longitudinal)	167.6(4)	172.9(4)
Detector 4 (longitudinal)	173.6(4)	174.0(4)

Table 40: Percentage differences between runs 161 and 163 for each detector using number of counts obtained with *counting bins*. Table 39, Equation 12.

Percentage differences between runs with *counting bins*	
	161-163
Detector 1 (transverse)	-1.3(3)
Detector 2 (transverse)	0.2(2)
Detector 3 (longitudinal)	3.1(3)
Detector 4 (longitudinal)	0.2(3)

Table 41: Percentage differences between detectors for runs 161 and 163 using number of counts obtained with *counting bins*. Table 39, Equation 13.

Percentage differences between detectors with *counting bins*		
	Run 161	Run 163
Detectors 1-2 (trans./trans.)	39.7(2)	40.6(2)
Detectors 1-3 (trans./long.)	-36.9(4)	-30.9(3)
Detectors 1-4 (trans./long.)	-32.2(4)	-30.2(3)
Detectors 2-3 (trans./long.)	-127.1(4)	-120.5(3)
Detectors 2-4 (trans./long.)	-119.2(4)	-119.2(3)
Detectors 3-4 (long./long.)	3.5(4)	0.6(3)

References

1. Zheng, Y. *Low Field MRI and the Development of Polarized Nuclear Imaging (PNI)-A New Imaging Modality* PhD thesis (University of Virginia, Oct. 7, 2014).
2. Zheng, Y., Miller, G. W., Tobias, W. A. & Cates, G. D. A method for imaging and spectroscopy using -rays and magnetic resonance. *Nature* (Sept. 2016).
3. Pallada, L. *IRM Imagerie par Résonance Magnetique* (HEdS Genève).
4. Bjørnerud, A. The Physics of Magnetic Resonance Imaging.
5. Pallada, L. *Modalités de diagnostique avec radio-isotopes (SPECT)* (HEdS Genève).
6. Rosen, M. S., Chupp, T. E., Coulter, K. P., Welsh, R. C. & Swanson, S. D. Polarized 129Xe optical pumping/spin exchange and delivery system for magnetic resonance spectroscopy and imaging studies. *Review of Scientific Instruments* (1999).
7. Driehuys, B. *et al.* High-volume production of laser-polarized 129Xe. *Applied Physics Letters* (1996).
8. Meersmann, T. & Brunner, E. *Hyperpolarized Xenon-129 Magnetic Resonance* ISBN: 978-1-84973-889-7 (Royal Society of Chemistry, 2015).
9. Appelt, S. *et al.* Theory of spin-exchange optical pumping of3He and129Xe. *Physical Review A - Atomic, Molecular, and Optical Physics* (1998).
10. Walker, T. G. & Happer, W. Spin-exchange optical pumping of noble-gas nuclei. *Reviews of Modern Physics* (Apr. 1, 1997).
11. Abdullah, K. M.-S. *Fundamentals in Nuclear Physics* (Dec. 2014).
12. Wiström, E. L. *Developing gamma-MRI with the Hyperpolarization of 129mXe and 131mXe by Spin Exchange Optical Pumping* Master thesis (University of Oslo).
13. Firestone, R. B. *Table of Isotopes* (1996).
14. Safari, M. J., Davani, F. A. & Afarideh, H. Differentiation method for localization of Compton edge in organic scintillation detectors.
15. Grover, V. P. *et al.* Magnetic Resonance Imaging: Principles and Techniques: Lessons for Clinicians. *Journal of Clinical and Experimental Hepatology* **5** (Sept. 2015).
16. Lewin, J. S. Interventional MR Imaging: Concepts, Systems, and Applications in Neuroradiology, 14 (1999).
17. Livieratos, L. in *Radionuclide and Hybrid Bone Imaging* (eds Fogelman, I., Gnanasegaran, G. & van der Wall, H.) (Springer Berlin Heidelberg, Berlin, Heidelberg, 2012).
18. Engel, R. *Planing, Simulation and Preparation of a Magnetic Resonant Imaging Experiment based on the Detection of Anisotropic gamma-Radiation from Hyperpolarized Isomers* PhD thesis (Carl von Ossietzky Universitat Oldenburg).
19. Zevallos-Chávez, J. *et al.* Response function of a germanium detector to photon energies between 6 and 120 keV. *Nuclear Instruments and Methods in Physics Research Section A: Accelerators, Spectrometers, Detectors and Associated Equipment* (Jan. 2001).
20. Virkki, O. *Distinguishing different radioactive sources with operative plastic scintillators* PhD thesis (University of Jyväskylä, May 25, 2018).
21. Jelescu, I. Introduction to MRI, echoes & contrast.
22. Della Volpe, D. *Interaction of photon with matter* (Université de Genève).
23. Della Volpe, D. *Interaction of Radiation with matter* (Université de Genève).